Theoretical studies of the dynamics of electron transfer in dye sensitized solar cells and of the mechanism of singlet fission in organic crystalline materials

by

Francesco Ambrosio

A thesis submitted in partial fulfilment of the requirements for the degree of

Doctor of Philosophy in Chemistry

University of Warwick, Department of Chemistry

June 2014

Table of contents

List of tables

List of figures

Acknowledgements

I would like to express my sincere gratitude to Prof. Alessandro Troisi for the support he granted during the entire duration of my studies. If I have become a better scientist after this experience, I owe this to his continuous incitement to improve myself, his meticulous advice, and inspiring discussions that allowed me to widen my knowledge and my capability of working in an academic environment, but also to develop working skills that will help my carrier, no matter which pattern I will follow after the completion of my studies.

I am also glad to thank sincerely Dr. Natalia Martsinovich. It was a privilege to have the opportunity to collaborate with her, during the first part of my PhD studies. Her devotion to research, her rigorous approach to science and her supportiveness will always be remembered and taken as an example.

I kindly acknowledge European Research Council (ERC) for financial support and Centre for Scientific Computing (CSC) for computational time and facilities.

Finally, I would like to dedicate this thesis to my family for the immense support received during my studies abroad. I never felt alone and I have to thank my father Raffaele, my mother Filomena, my brother Enzo and my sister Letizia. Finally (last but not least) I would like to express my infinite gratitude to the mate of my life Rosa, who shared this adventure with me, to her family, and I dedicate this thesis to our son, the little Raffaele, who is just laughing while I am typing these words. They all helped me to carry on, during difficult periods.

Declarations

This thesis is submitted to the University of Warwick in support of my application for the degree of Doctor of Philosophy in Chemistry. It has not been submitted in any previous application for any degree and it has been composed by myself. Computational strategy and part of the density functional theory calculations (around 50%), presented in Chapter 5 to describe the TiO_2-N_3 interface and the electron injection properties of the N3 dye, were performed by Dr. Natalia Martsinovich, along with supplemental analysis of data, required for the creation of Figures 5.2-5.4.

Part of this thesis has been published by the author:

1. Ambrosio, F; Martsinovich, N; Troisi, A. Effect of the Anchoring Group on Electron Injection: Theoretical Study of Phosphonated Dyes for Dye-Sensitized Solar Cells. *J Phys. Chem. C* **2012**, *116* (3), 2622-2629.

2. Ambrosio, F; Martsinovich, N; Troisi, A. What Is the Best Anchoring Group for a Dye in a Dye-Sensitized Solar Cell? *J. Phys. Chem. Lett.* **2012**, *3* (11), 1531-1535.

3. Martsinovich, N; Ambrosio, F; Troisi, A. Adsorption and Electron Injection of the N3 Metal-Organic Dye on the TiO_2 Rutile (110) Surface. *Phys. Chem. Chem. Phys* **2012**, *14* (48), 16668-76.

Abstract

We present a theoretical and computational study on two different processes of interest for the development of third generation solar cells: (i) electron injection in dye sensitized solar cells (DSSCs); (ii) mechanism of singlet fission (SF) in organic crystalline materials, commonly employed in organic solar cells.

(i) Electron injection rates in DSSCs are computed through a combination of *ab initio* calculations and theoretical modeling. In particular, rates are calculated using a matrix partitioning approach, in conjunction with the propagation of Green's functions. We are able to separate the entire dye-semiconductor surface in smaller sub-systems, whose study is less computational demanding. We prove that this approach is not only capable of simulating experimental results, but, due to its flexibility, can be used in a predictive way. We propose three possible applications of our method: a) a comparative study of different organic dyes sharing the same anchoring group; b) an investigation aimed to identify the optimal anchoring group for a DSSC dye, by screening 15 potential candidates in terms of adsorption strength on the TiO_2 surface and electron injection properties; c) an extension of our approach for the study of metal-organic dyes, attaching the TiO_2 surface through a variety of binding modes and with multiple anchoring groups.

(ii) SF is studied focusing on the multi-excitonic (ME) intermediate, playing a pivotal role in the mechanism of the process. A model configuration interaction Hamiltonian is presented for the study of the electronic structure of a linear cluster of molecules undergoing to SF. The analysis of its electronic structure shows that different distances between the pseudo-triplets composing the ME produce energetically distinguishable states. In particular, we can separate the ME in two types: bound stabilized ME states whose pseudo-triplets are located on neighboring molecules, and unbound ME states, whose energy is almost equal to the energy of two triplets. We also demonstrate that, while singlet excitons are delocalized, ME states are localized. Dynamics of the $ME \leftarrow S_1$ radiationless decay is studied with Fermi golden rule, where a model is proposed to simulate explicitly the vibronic ME states. Effect of different choices of model parameters is studied, along with an analysis of the branching of the rates, showing that the transition occurs almost completely toward bound ME states.

Abbreviations

B3LYP	Becke 3-parameter exchange and Lee-Yang-Parr correlation functional
CAS-SCF	Complete active space self consistent field
CI	Configuration interaction
CB	Conduction band
CT	Charge transfer
DFT	Density functional theory
DSSC	Dye sensitized solar cell
FGR	Fermi golden rule
GF	Green's function
GGA	Generalized gradient approximation
HF	Hartree-Fock
HOMO	Highest occupied molecular orbital
LDA	Local density approximation
LUMO	Lowest unoccupied molecular orbital
ME	Multi-exciton
MEb	Bound multi-exciton
MEu	Unbound multi-exciton
N3	Cis-bis(isothiocyanato)-bis(4,4'-dicarboxy-2,2'-bipyridyl)-ruthenium(II)
OSC	Organic solar cell
S_1	First excited singlet state
SCF	Self consistent field
T_1	First excited triplet state
TD-DFT	Time dependent density functional theory

Chapter 1:

Introduction

1.1 Alternative sources of energy: a global challenge

According to estimations deriving from Hubbert peak theory[1, 2], oil extraction will begin its decline after 2020. Despite the criticism about oil peak theory[3], there is an undeniable truth: mankind will be obliged to face an enormous shift of paradigm in the consumption and production of energy. The gargantuan profile of this global challenge is even extended, if we consider that energy consumption have been increasing exponentially from the days of the first industrial revolution and it is still growing in the new millennium. It is actually driven by the industrialization of emerging countries − a trend that is not likely to be inverted in the near/mid-term future. More energy will be needed but we will not be able to use traditional means of provision, which actually supply the vast majority of energy in the world − a conundrum that is still far from being solved.

Moreover, the increasing consumption of fossil fuels has led to a dramatic increase in CO_2 emissions, raising the issue of global warming, which has been world-wide addressed by Kyoto protocol, setting, for the first time, strict limits to the production of greenhouse gases in industrialized countries.[4] Therefore, we have to face a world-wide increasing energy consumption that cannot be dealt with, adopting traditional schemes; moreover, depletion of raw materials represents a geo-political issue, due to

the competition among industrialized countries for the control of continuously decreasing resources.

Renewable energy resources (solar, tidal, wind, geo-thermal heat) could represent a viable solution for this problem. However, in spite of the increasing efforts produced during the last decades, only a small percentage (3%) of energy is produced in this way and only a fraction of it is obtained by solar energy conversion.[5] Nevertheless, solar energy alone could in principle satisfy the request of energy of the entire planet, covering also future increases in energy demands: solar luminosity irradiated on Earth in a year is ten orders of magnitude higher than current annual energy consumption. The realization of a cost-efficient device, capable of converting only a portion of solar power irradiated, would provide extraordinary benefits and also ensure long-term geo-political stability.

Among a wide variety of possible architectures and materials that have been tested in the last decades, silicon based solar cells, the first invented solar cells, still holds the monopoly of the sector.[6] High conversion efficiencies have been achieved for single junction (~25%) solar cells.[7] Nevertheless, silicon based solar cells present several major drawbacks. First of all, pure silicon is needed for this kind of device, and it must be obtained from purification of silicate minerals, involving strongly endothermic reactions. This process drastically decreases the net energy, shifting the balance between the energy required to produce the device and the energy produced by the device during its life-span.[8, 9] Moreover, silicon is one of the most requested (hence expansive) raw materials, since it is widely used in electronics industry, and it is supplied by few countries in the world.[10]

For these reasons, research, both theoretical and experimental, has been focused, in the last decades, on individuating valid alternatives to silicon solar cells. The idea behind this new approach to solar energy (the so called third generation photovoltaics) is based on a drastic reduction of the costs of production. As these are dramatically reduced, if compared to silicon cells, the conversion efficiency required for the fabrication of a cost-effective cell is sensibly lowered.[11]

Among the vast variety of possible alternatives, dye sensitized solar cells (DSSCs), designed by Grätzel and O'Reagan in 1990[12], represent one of the most intriguing alternatives: they show promising efficiencies[13, 14] and inexpensive fabrication processes are already available. However, these devices are far from being optimized and, even if an initial commercialization of DSSC niche products has recently started, efficiencies are still not high enough to grant cost-effectiveness and large scale production. In particular, electron transfer processes, occurring in DSSCs, need to be elucidated, in order to understand how to modify the devices and increase their efficiencies.[15]

Another possible solution could be realized, surpassing the conversion efficiency limit set by theory: in 1961 Shockley and Queisser calculated the maximum theoretical efficiency for a single junction solar cell, which is, for an idealized semiconductor, only 33.7%.[16] Different methods have been theorized to overcome this limit and the use of singlet fission (SF) seems to be one of the most promising. SF is a process allowing the generation of two photo-excited electrons for each harvested photon, from the fission of a singlet exciton in two triplet excitons.[17] This process takes place in different materials that can be used in solar cells, particularly in organic solar cells (OSCs).[18] In principle, exploiting this physical process in a solar cell, could double its efficiency.

This would be fundamental for OSCs and other emerging solar cells, that struggle to reach a satisfactory efficiency. However, the mechanism of SF still holds unclear aspects, preventing its efficient use in solar cells.[17, 19]

Since the first investigations on DSSCs, computational and theoretical chemistry have been used to disentangle some of the phenomena that are relevant to the functioning of DSSCs and to introduce an element of design in the systematic exploration.[15] Due to the complexity of the device (described in Section 1.2), theory can contribute, more than in other research fields, not only to understand the experiments but to be predictive, addressing the development of new and more efficient solar cells. In Sections 1.5 and 1.6 we report the recent advancements made by experiments and theory, respectively, for DSSCs, but we anticipate that no optimal configuration of the device had been obtained yet, thus preventing sensible advancements, in terms of efficiency, from the early archetypal Grätzel cell: DSSCs showed around 11% efficiency in 1991,[12] recent record-breaking device in 2011 provided 12% efficiency,[13] and mesoscopic cells reached 15% in 2013[14]; the efficiency in 20 years was increased only by 1% and only very recently by 4%. One of the reasons behind this problem is the lack of a comprehensive knowledge of the electron transfer processes occurring in DSSCs and how they are related to the complex interplay among the different constituents of the device. In this framework, theory can play a fundamental role, in providing this knowledge and, therefore, assist the development of more efficient devices.

Theory can play a key role also in the study of SF and for its successful application in OSCs. In particular, the mechanism of SF has not been clarified yet: experiments alone struggle to capture the possible intermediate states of the process, which elude classical spectroscopic techniques. The lack of a full understanding of SF also casts shadows on

the possibility of its application in OSCs, which is currently controversial.[18, 20, 21] In the last years, different theoretical models[22-26] have been suggested and some *ab initio* studies [27-31] have been performed, in order to elucidate the SF mechanism and the electronic states involved in the process, in crystalline organic materials; these are described in detail in Section 1.6 but we can already reveal that there is a certain disagreement among different hypotheses, and that most of the current works provide *ab initio* calculations or phenomenological models featuring only a small model of the system (usually a dimer), which is not sufficient to describe the physics in a crystalline organic material. Therefore, further work is needed to understand the electronic states involved in SF and its dynamics. This knowledge would also be beneficial in providing a rational scheme for successful employment of SF in OSCs.

In this thesis, we present a theoretical study on (i) electron injection, one of the electronic transfer processes occurring in DSSCs, and on (ii) SF in a model system mimicking properties of crystalline organic materials. The dynamics of both these phenomena, occurring in different systems, can be studied, adopting the same theoretical framework provided by time dependent perturbation theory. This work aims to contribute to the knowledge of elementary electron transfer processes, which play a fundamental role in modern technology, and to assist the design of new and more efficient solar cells. In the next sections we are going to introduce in detail DSSC functioning mechanism (Section 1.2) and SF process (Section 1.3), along with a brief description of the state of art of experiments (Section 1.5) and theory (Section 1.6 for DSCCs and 1.7 for SF).

1.2 Dye sensitized solar cells: device and electron transfer processes

DSSCs, as originally conceived by Grätzel and O'Reagan in 1990[12], are typically composed by (i) a wide band gap semiconductor nanoparticles deposited on (ii) a transparent conducting substrate (usually fluorine doped tin oxide (FTO)), (iii) a molecular sensitizer stably anchored on the nanoparticle surface and a (iv) redox electrolyte in solution and in contact with (v) a counter electrode, as depicted in **Figure 1.1**.

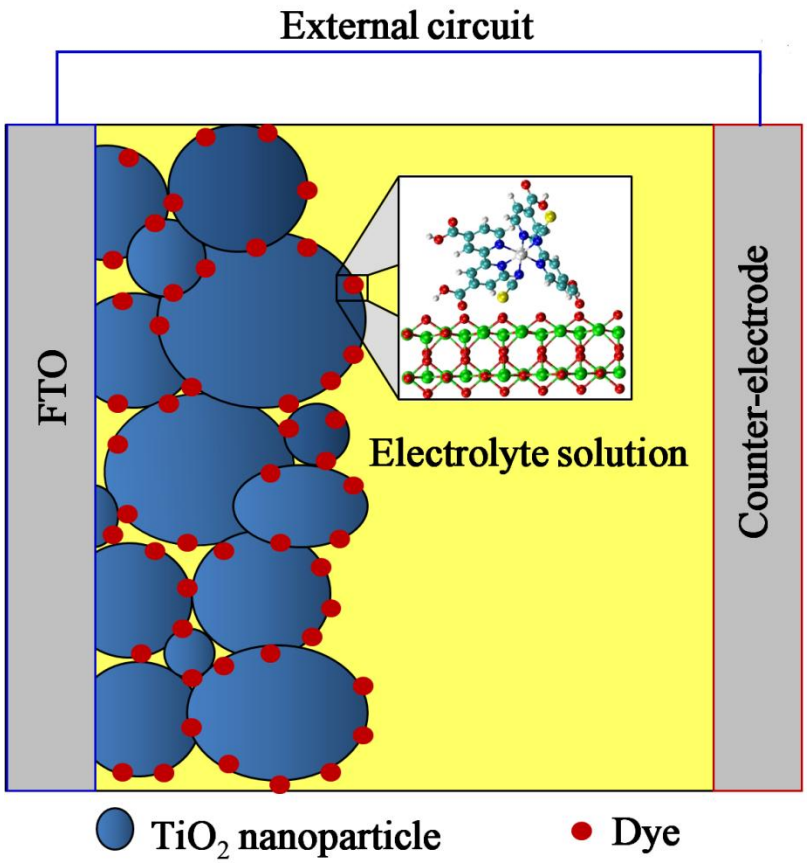

Figure 1.1: Schematic representation of a DSSC device.

The working mechanism of a DSSC is the result of a series of electron transfer processes which mimic photosynthesis: solar radiation is absorbed by the dye which, in its excited state, transfers an electron to the conduction band (CB) of the semiconductor. This electron transfer at a heterogeneous interface, occurring on the femtosecond (fs) time-scale, is called electron injection and will be studied in this thesis. Fast electron injection, while not being a sufficient condition for a high-efficiency device, is surely a necessary requirement: slow electron injection is likely to lead to poor performance of the solar cell.[32] The transferred charge then diffuses through TiO_2 nanoparticles to the electrode, where it is collected by an external circuit and reaches the counter-electrode. The circuit is closed by oxidation of the dye cation (dye regeneration) operated by the reduced species in solution, which in turn diffuse to the counter electrode, where are reduced again (electrolyte regeneration). In this way, a photo-voltage between the semiconductor and the counter electrode is generated, as schematized in **Figure 1.2**. This process is however affected by some loss mechanisms: (i) effects of thermal de-excitation,[33] (ii) charge recombination at the interface to the dye[34-36] or (iii) to the electrolyte.[35-37] Charge recombination, in particular, occurs when the electron transferred to the TiO_2 CB is back-transferred to the dye cation or to a reduced species in solution. These processes, even occurring on the millisecond (ms) timescale, are favored by slow diffusion of the electron to the electrode. The study of these electron transfer processes is beyond the scope of this thesis but it is important to underline that they dramatically affect the final efficiency of the device. For an exhaustive dissertation on this topic see ref.[38].

The efficiency of a DSSC is experimentally expressed by two parameters: the short-circuit photocurrent and the open circuit potential difference (photovoltage)[39]. The

former is due principally by a balance between (i) dye's light harvesting power, its injection characteristics and electron mobility through the nanoparticles, and (ii) back electron transfer processes and electron trapping in semiconductor defect states. The latter is given by the difference between the quasi-Fermi level of the semiconductor and the redox couple Fermi level. The choice of components obviously affects these parameters, however no trivial cause-effect explanation can be achieved because the effect of each component is not independent from the others, i.e. a dye that is excellent in an experiment could be a poor choice if the electrolyte or the semiconductor is changed. Hence, despite increasing efforts, optimization of the device is still far from being obtained, since an independent optimization of the individual components is not achievable, and different pathways are followed,in order to increase the efficiency.[39]

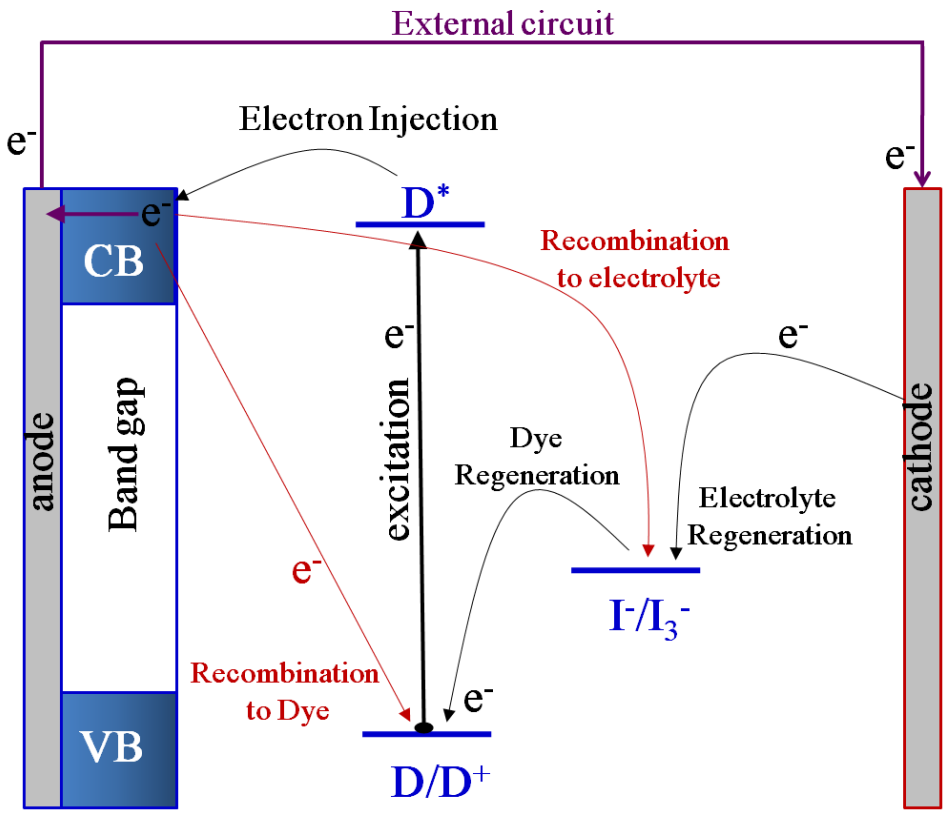

Figure 1.2: Schematic representation of electron transfer processes occurring in DSSCs.

Regarding the semiconductor, TiO_2 is the preferred choice for semiconductor nanoparticles: titanium dioxide is cheap, abundant on Earth, nanoparticles fabrication is inexpensive and it has a wide band gap. Two polymorphs of TiO_2 are commonly used: rutile and anatase, with the latter being usually preferred for better thermodynamic stability[40-43]. A wide variety of possible alternatives to TiO_2 have been studied: SnO_2[44], WO_3[45], $Nb2O_5$[46], $SrTiO_3$[47], ZnO[48]. Also different architectures have been experimented: TiO_2 nanowires[49], different nanoparticle fabrication[50] or the introduction of metal oxide blocking layers[35]. Aims of these investigations are: (i) the search for an optimal alignment of the energy levels, which favors desired electron transfer processes; (ii) obstruction of back electron transfer pathways; (iii) the attempt to obtain higher electron mobilities; (iv) improve the stability under illumination; (v) avoid photodecomposition of the dye.

Intense research has been devoted to the study of efficient redox species. In fact, a good number of alternatives have been recently introduced to the I_3^-/I^- couple used in the archetypal Grätzel cell: cobalt[13] and iron[51] based complexes, organic radicals[52] and solid state architectures based on polymers[53] or organic-inorganic hybrids.[14] Reasons to substitute the I_3^-/I^- couple are given by (i) adopting redox species with a simpler electrochemistry, (ii) increasing the open circuit voltage by lowering the Fermi level of the redox couple. Finally, solid state architectures could in principle overcome the diffusion issues arising in a solution and recently a solid state DSSC, based on a perovskite pigment, reached a record efficiency (15%).[14]

Finally, the possible dyes for DSSCs can be divided in two categories: (i) metal-organic dyes[12, 13, 54-56] (ii) organic dyes.[57-60] Ruthenium dyes have been the ones providing the highest efficiencies[12, 54-56] until 2011, when their record was broken

by Zn-porphyrins.[13]. Nevertheless, metal-organic dyes, even if providing the best results, are usually more expansive and their synthesis is more complicated. Moreover, their size prevents a more efficient coverage of the nanoparticle surface. Therefore, purely organic dyes represent an interesting alternative, due to their enormous versatility, given by low costs and feasibility of synthesis.[61] Co-sensitization of TiO_2 with different dyes has also been investigated, using dyes adsorbing in different regions of the light spectrum, to enlarge the range of collected photon energies.[62]

1.3 Singlet fission: a general overview

SF is a special case of spin allowed transition, where a single-exciton singlet state (usually S_1) splits in two coupled single-exciton triplet (T_1) excitations.[17, 19] Decades after its first observation in anthracene crystals, SF has been recently experimented in a wide variety of crystalline organic materials[63-70], polymers[71], quantum dots[72] (QD) and in solution.[73] The reason behind a renewed interest on this physical phenomenon is given by the opportunity to exploit it, in order to overcome the Shockley-Queisser theoretical limit of conversion efficiency for single junction solar cells.[16] In fact, adopting materials capable of SF, as light harvesting units in solar cells, may allow to generate two photo-excited electrons for each captured photon, doubling, in theory, the quantum efficiency. Moreover, back electron transfer processes from triplets would be spin forbidden. However, each of the two triplet excitons generated by SF possesses around half the energy of the singlet exciton, thus also halving the potential voltage. Therefore, the use of a SF material should be combined with materials absorbing at long wavelength. Exploiting SF could drastically increase

the conversion efficiency in (i) OSCs, adopting a SF-based donor material;[18, 20, 64, 69, 74-78] (ii) DSSCs, if a SF dye is employed;[63, 79] (iii) QD solar cells.[63, 80, 81] Recently, high values of external quantum efficiency (EQE) for SF-based OSCs have been measured, employing pentacene and tetracene. [18, 64] However, Mazumdar and coworkers argue that the connection between high EQE and SF cannot be completely proven by current experiments.[21]

Nevertheless, the SF mechanism still holds unclear aspects, leading to inconsistent interpretations of the phenomenon and preventing from manufacturing the expected high-efficiency devices.

SF is a thermodynamically favorable process when the following condition is satisfied[17]:

$$E(\mathrm{S}_1) > 2E(\mathrm{T}_1) \tag{1.1}$$

where, for isolated molecular pairs, $E(\mathrm{S}_1)$ and $E(\mathrm{T}_1)$ represent the energy of the first singlet and triplets states, respectively, while for crystalline materials represent the bottom of the singlet and triplet bands, respectively. Eq. 1.1 is true for organic crystalline materials like pentacene and hexacene derivatives, the former being the most studied material for SF purposes.[26, 28, 29, 63, 69, 75-78, 82, 83] For hexacene, instead, a possible fission of the singlet in three triplets has been recently proposed, due to the extremely low energy of T_1.[84] However, hexacene is very instable[85] and, for this reason, is usually functionalized.[86, 87] For these crystalline organic materials, the production of two separate triplets is an ultrafast process ranging from hundreds of fs (pentacene) to ps (hexacene).[82, 83] In other materials, i.e. tetracene, the previous condition is not met and SF should be thermally activated, thus lowering the rate of the

process. Bardeen and coworkers found an ambiguous temperature-dependence for the decay of singlet exciton in tetracene crystals, in particular at low temperatures (200 K), explained by possible change of polymorphism in tetracene crystals.[65, 66] However, Friend and coworkers suggest that the generation of triplet pairs, in absence of the driving force given by exothermicity, is due to an equilibrium-like process between S_1 and $2T_1$ populations, thus explaining both lower rates and high quantum yield[63]. Techniques commonly employed to study SF dynamics are briefly described in Section 1.4.

It is known that the mechanism of SF features an intermediate state which is typically described by a doubly excited configuration where two triplets with opposite spins are accommodated on two different excitation sites. This state is referred in literature as ^{1}(TT) or, more commonly, as multi-excitonic (ME) state.[17, 19] Its overall spin multiplicity is a singlet, and hence the process is spin allowed. SF can be described as a two steps process:

$$S_0 + S_1 \rightleftarrows ME \rightleftarrows T_1 + T_1 \qquad (1.2)$$

Where the ground state S_0 is included since it is involved in the overall mechanism. Experimental proof of existence of this dark state has been recently obtained via time-resolved two-photon photoemission spectroscopy for the pentacene/C_{60} system.[75]

1.4 Experimental techniques for the study of the dynamics of ultrafast charge transfer processes

1.4.1 Pump probe spectroscopy

Different time resolved spectroscopy techniques have been used to study electron injection in DSSCs and SF, such as (i) Uv-vis transient absorption spectroscopy[63, 69, 82, 84, 88-92] (ii) time resolved fluorescence spectroscopy[65, 93] (iii) time resolved infrared and Raman spectroscopy[94, 95] (iv) time resolved photoemission spectroscopy.[75, 88, 91, 92, 96-98] All these techniques share the use of the so-called pump-probe methodology: an ultrafast laser pulse is directed to the sample, populating an excited state (pump); then a second laser pulse (probe) is used to control the time-dependent evolution of this state, by monitoring physical properties of the sample. For example, in Uv-vis transient absorption spectroscopy, the time-dependent absorbance variation is monitored. In particular, for the case of electron injection in DSSCs, in the pump step the dye is photoexcited, while the probe monitors the rise in absorbance of the dye cation, due to the electron transfer to TiO_2. Finally, fitting of the time-dependent signal allows to calculate the time constant for electron injection. This method has been widely adopted for the study of electron injection of a variety of dyes. Transient absorption has been also used for the study of singlet fission dynamics in tetracene, pentacene, and hexacene derivatives. In this case, time delayed absorption signals for singlet and triplet states are observed and, hence, singlet fission rates are computed, showing fs timescales for pentacene[82] and ps timescales for tetracene[63] and hexacene.[84]

A similar procedure is adopted in time resolved fluorescence spectroscopy, where the time-dependent fluorescence is monitored instead. This technique has been used, for example, to study the electron injection dynamics of coumarin 343 on TiO_2.[93] Delayed fluorescence has also been used to study singlet fission dynamics in tetracene crystals, in order to investigate the lifetime of coherent triplet pairs.[65]

Time resolved IR spectroscopy has been adopted to study electron injection of Fe(II) complexes[89] while time resolved Raman spectroscopy has been used to study coumarin 343.[94] This technique provides also structural insights on the dye-TiO_2 system as it allows to observe time-dependent changes in the adsorbed dye's vibrational spectrum. It is a convenient choice of investigation when the interpretation of the Uv-vis spectra is affected by spectral overlap problems.

Finally, in time resolved photoemission spectroscopy, the probe pulse is used to induce photoemission of the electron from the excited state. The time-dependent population of the excited state is hence recorded, by changing the time delay between the pump and the probe pulses. This technique is mostly used to study dyes adsorbed on single crystals, instead of nanoparticles, and it overcomes some of the drawbacks of transient absorption method: while the latter need high extinction coefficients and high coverage of the surface, time resolved photoemission spectroscopy is more sensitive, being suitable also for low dye coverage of the surface.[88, 91, 92] It is important to underline that experimental injection times are usually upper limits estimates: this is due to instruments resolution ranging, for different techniques, from few fs[98] to 100 fs.[89]

More recently, time resolved photoemission spectroscopy has been successfully employed to study SF dynamics and the SF mechanism in tetracene and pentacene

crystals, but also in model SF based solar cells.[75, 96, 97] In fact, in this application of photoemission spectroscopy, the different excitonic states (S and T excitons, ME) are detected and distinguished because of different photo-electron energies. This allowed to obtain a first direct observation of the ME state in the C_{60}-pentacene interface, which had eluded other techniques.[75] It was also possible to study different rates of the S_1←ME non radiative decay in pentacene and in tetracene, the former occurring with ultrafast dynamics (~100 fs)[75], the latter being sensibly slower (~7 ps).[96, 97]

1.4.2 Resonant photoemission spectroscopy (core-hole clock method)

In resonant photoemission spectroscopy (RPES), resonant excitation (core-hole creation) is followed by core-hole decay with Auger emission. This ultrafast process can be schematized in two steps: in a first step, X-rays irradiate the sample, exciting one of its core-electrons to an unoccupied orbital. Hence, the hole left in the core level is filled by either the excited electron or by an electron from another orbital.[99] In both cases an Auger electron is emitted, its kinetic energy E_k being proportional to the exciting photon energy.

When the sample is irradiated with X-rays, if the energy is slightly lower or slightly higher, the same unoccupied orbital is filled by the core electron. Because of energy conservation, any excess energy is conserved by the molecule: this can be described as if, in the resonance width, there is a manifold of virtual states that can be filled by the core electron. This broadening is similar to the Raman vibrational broadening and, therefore, the process is usually named “Raman-like” and the relative peaks observed in the photo-emission spectrum are called “Raman-like” peaks.

When the molecule is linked to a semiconductor substrate, as in the case of DSSCs, the excited electron, if there is a favorable energy levels alignment, can delocalize to the substrate empty states (in DSSC case the manifold of the CB of the semiconductor), a process earlier described as electron injection. In this case, the E_k of the emitted Auger electron will be no longer proportional to the exciting photon energy. It will be a constant value instead, since charge delocalization to the semiconductor causes loss of information of the excited state.

In a resonant photoemission spectrum the peaks deriving from de-excitation of the excited state and from charge delocalization can be distinguished, because of the different E_k dependence. Moreover, the ratio between the lifetime of core-holes τ and charge transfer time τ_{CT} is related to the ratio of the intensities of the two peaks (I and I_{CT}):

$$\frac{\tau}{\tau_{\mathrm{CT}}} = \frac{f}{1-f} \tag{1.3}$$

$$f = \frac{I}{I + I_{CT}} \tag{1.4}$$

Eq. 1.3 and 1.4 are the basis of the so-called core-hole clock method[99] which is employed to evaluate τ_{CT} from RPES experiments, and the ideal conditions of applicability of the method are met when $0.1\tau < \tau_{\mathrm{CT}} < \tau$, i.e. the difference should be contained in one order of magnitude. This feature, while restricting the validity of the method to a small range of times, enables it to overcome limitations of transient spectroscopy and probe very short injection times (<10 fs). A possible drawback of this method is given by the fact that, if ground and excited states of the molecule are significantly changed when adsorbed on the substrate, the resulting core-hole spectrum will be complicated to interpret.

This technique has been employed for the calculation of electron injection times of ruthenium dyes on rutile(110),[100, 101] of isonicotinic and bi-isonicotinic acid on rutile (110) surface[102] and on anatase (110)[103, 104], allowing to sample electron injection times of the order of few femtoseconds.

For example, for ruthenium dyes, the de-excitation time is described by the N 1*s* core-hole lifetime and the electron injection is computed from LUMO+2 and LUMO+3 of the dye.[101]

1.5 Dye sensitized solar cells: theoretical studies of the dye-TiO_2 system

In this section we report the contributions made by theory, for the study of the dye-semiconductor interface in DSSCs and for the calculation of electron injection rates. In fact, a correct description of the dye-TiO_2 interface is fundamental for electron injection; the adsorption geometry influences the electron injection, as the chemistry of the anchoring group of the dye and its attachment to the surface determines the dye-TiO_2 electronic coupling. Moreover, studies of dyes adsorption are fundamental to assess the adsorption strength, as a stable adsorption of the dye is necessary to develop an efficient device.

1.5.1 Theoretical and computational studies on TiO_2

The structural and electronic properties of rutile, anatase and of their most stable surfaces have been widely studied. Adamo and co-workers evaluated the structural and electronic properties of the two polymorphs of TiO_2, with *ab initio* calculations, carried out both at the Hartree-Fock (HF) and at the density functional theory (DFT) level of

theory. Their results suggested that anatase is the most stable form of TiO_2. The same authors were also able to characterize the electronic structure of both polymorphs, in terms of bands structures and densities of states: in both cases the top of the valence band (VB) is mainly due to O_{2p} states, while the lowest part of CB is composed by Ti_{3d} states.[40] Adamo and co-workers also performed a similar study, on rutile and anatase slabs, in order to calculate surface energies, full-relaxation effects and electronic properties, such as the band structures and the densities of states, obtaining results in good agreement with experimental works. The results were able to describe the relative stability of the different surfaces and they confirmed, regarding the electronic properties, the conclusions drawn for the corresponding bulk cases.[41] An intriguing aspect is the oscillating behaviour of the geometric and electronic properties of rutile TiO_2 (110) thin films, as a function of the number of layers.[105] Pacchioni and co-workers proved that this phenomenon is caused by the change of O_{2p}-Ti_{3d} interlayer hybridization along the layers, due to a symmetry plane, which is contained in films with an odd number of layers.[106]

1.5.2 Theoretical and computational studies on molecular dyes and their adsorption on TiO_2 surfaces

The connection between dyes structures and DSSC efficiency has been vastly discussed[107] and, therefore, studies of molecular dyes on TiO_2 surfaces present a fascinating challenge for theoretical chemistry; due to the extremely wide range of available dyes for light harvesting in DSSCs, whereas the choice of the molecule to be studied is often made on a trial and error basis, theory can provide a methodological approach, predicting the properties of the most effective chromophores. Hence, theory is not only capable of explaining the experiments results, but can address the synthesis of

new and more efficient molecular dyes. In this regard, several studies on the influence of the sensitizer adsorption modes have been conducted. It has been shown that the sensitizer adsorption geometry of Ru-complexes has a remarkable influence on the open circuit potential, therefore on the efficiency of the DSSC device.[108] In particular, several possibilities have been explored, from the simple difference between molecular and dissociative (with protonation of the TiO_2 surface) adsorption modes to the comparison between mono-dentate and multi-dentate absorption geometries. It has been demonstrated that the sensitizer dipole moments, associated with different adsorption modes, can influence the position of the TiO_2 CB.[108] The alignment of the dye's molecular levels with the TiO_2 CB states, which is one the parameters determining the rate of the electron injection, has been analyzed through DFT and time dependent DFT (TD-DFT) studies for several Ru-complexes, highlighting how the position and the character of the HOMO-LUMO levels of the dyes are noticeably different in the isolated and interacting systems.[109-112] Purely organic molecules have also received a great attention: in particular coumarin based dyes[113], and alizarine[114, 115]. More recently, anthracene based sensitizers have been studied, showing appreciable conversion efficiency.[60] Finally, also di-anchoring group organic dyes have been investigated, demonstrating that the double adsorption improves the electronic properties of the system.[116]

1.5.3 Theoretical and computational studies on the electron transfer reactions at the interface between dye and semiconductor

The dynamics of photoinduced electron transfer processes at dye-semiconductor interface has been studied with different approaches and methods in the recent years.

Thoss and coworkers developed an *ab initio*-based method, called multi-layer multi-configuration time-dependent Hartree (ML-MCTDH) method.[117] This variational approach features a representation of Hamiltonian in a basis of localized donor and acceptor states, where the parameters of the Hamiltonian have been taken from *ab initio* calculations.[113, 118, 119] Prezhdo's group used non-adiabatic molecular dynamics to simulate electron transfer on timescales of up to tens of femtoseconds and to distinguish between adiabatic and non-adiabatic electron transfer pathways. For example, electron dynamics and electron transfer rates at the alizarine/TiO_2 and bipyridine/TiO_2 interfaces were studied. [114, 115, 120-122] However, even if an *ab initio* description of the interface is appealing, this kind of time-resolved simulations is still rare and computationally demanding. Batista and coworkers used *ab initio* molecular dynamics (within DFT). They adopted a model Hamiltonian derived using the semiempirical extended Hückel approach, to describe the excited states and propagate the wave function in time, for representative nuclear configurations. In this way, they modeled the dye-semiconductor electron transfer and subsequent charge delocalization in TiO_2 crystals.[123, 124] May and co-workers studied the heterogeneous electron transfer for the TiO_2-perylene system using a diabatic-like separation of the whole system into molecular and semiconductor states and considered the ground and first excited state sfor the dye together with a large number of states in the CB of the semiconductor[125, 126], an approach which presents some similarities with the method that we employ in this thesis. However, the model used by May and coworkers is based on experimental results, since the Hamiltonian features parameters which are fitted to measured spectra. More recently, Wang and May studied the enhancement of electron injection, due to metal nanoparticles used in conjunction with the dye and the semiconductor.[127]

The methods discussed above are all limited to some extent by the inability of predicting the alignment of the energy levels of the dye and the semiconductor in the presence of a complex liquid-solid interface (in addition to the DFT limitations which can be in principle reduced). Moreover, current models and methods to study electron injection either require a computational demanding simulation of a complete semiconductor-chromophore system, or they have to relate on experimental results. In either case, they are not suitable for systematic studies of electron injecting properties of a wide variety of chromophores and they are not able to disentangle the different driving forces (dye chemistry, anchoring group chemistry, attachment chemistry) of the electron injection process. Nevertheless, this knowledge is fundamental, since it may assist experiments, by conceiving rational rules for the design of new and more efficient dyes.

Our approach is based on partitioning the TiO_2-dye system into smaller sub-systems, as described in Chapter 2, where our methodology is explained in detail and compared with previous works. Our method does not need a simulation of a complete semiconductor-chromophore system and does not rely on experimental data. It has been previously applied to study injection times in a series of organic dyes, including perylene derivatives, isonicotinic and biisonicotinic acid and coumarin[128, 129]. In Chapters 3-5 we report three different applications of this method, for the study of electron injecting properties of DSSC dyes.

1.6 Singlet fission in organic crystalline materials: theoretical studies on the mechanism and role of the multi-excitonic state

A main controversy in SF mechanism arises from the coupling between ME and S_1 states: some studies suggest that the driving force for the ME←S_1 non radiative decay is given by direct coupling between these two states;[28, 29, 65, 130] Another school of thought indicates that direct coupling is not sufficient to explain the rates of SF and suggests that indirect coupling via charge transfer (CT) states causes the ultra-fast dynamics of ME generation[22-24].

Zimmermann and coworkers employed post-HF methods to study a pentacene dimer model. They characterized the ME as the intermediate state leading to SF. They found that ME←S_1 transition is fast and the subsequent separation in $2T_1$ is favoured by the formation of an excimer-like complex[28]. In a successive paper, they also studied pentacene and tetracene through QM/MM calculations, adopting the RAS-2SF method[131]; they suggest that the driving force for the ME←S_1 transition is the direct coupling between them and no CT state is involved in the process[29]. Zhu and coworkers argue that the ultrafast dynamics arising from available experiments cannot be justified by direct coupling between S_1 and ME. Multi-state DFT and density matrix modeling were employed to show that indirect coupling through CT states is two order of magnitude higher than direct coupling. This should justify the ultrafast dynamics, in conjunction with high density of ME states and dephasing produced by environmental effects[22]. Casanova studied tetracene and two of its derivatives with *ab initio* quantum chemical calculations, excluding in all the cases the role of CT states as possible intermediates of the SF mechanism, but confirming their role for second order

coupling[30]. Very recently, Voorhis and coworkers calculated the energy levels and the electronic coupling between S_1 and a TT state for dimers belonging to the crystallographic structures of different pentacene and tetracene derivatives, using constrained DFT (CDFT) and CDFT based configuration interaction (CDFT-CI).[132] Rates of SF, following the scheme proposed by Bixon and Jortner,[133-135] were in agreement with experimental results.[31] Regarding the mechanism, it is proposed that, for weakly interacting systems, SF is non-adiabatic while it is adiabatic for strongly coupled systems.[31]

Recently, theoretical studies have also been carried out, in order to investigate the interface between the SF material and the donor material in an OSC. Prezhdo and coworkers studied the C_{60}-pentacene interface, deriving a kinetic model for SF from non adiabatic molecular dynamics. They found that SF in a typical interface of an OSC must compete with the usual mechanism of exciton dissociation at the donor-acceptor interface[27]. This agrees with previous studies, motivating the competition between SF and exciton dissociation at the interface, for C_{60}-pentacene and C_{60}-tetracene systems, and showing that SF is favored for pentacene but not for tetracene[97]. However, a critical point of non adiabatic dynamics is given by the fact that it forces the system into one of the adiabatic potential energy surfaces via a sequence of fast hops, while, for very fast processes it is more likely for the system to be in a linear combination of electronic states.

In their recent papers, Reichman and coworkers developed a phenomenological model based on a minimal CI Hamiltonian. The dynamics of SF for a pentacene dimer were studied, considering only the electronic degrees of freedom explicitly, while all nuclear modes are part of a bath system. The results for this kind of approach suggest that SF

occurs via a “super-exchange” mediated mechanism, through CT states, even if these states possess very high energies[22-24]. Krylov and coworkers criticize such a diabatization approach and propose the use of adiabatic wave-function and the calculation of non adiabatic couplings. In this way, they argue that there is no need to introduce concepts like “super-exchange” or “two electron coupling”, since the CT configurations are already included in S_1 and ME wave-functions[25]. In a similar approach, Spano and coworkers developed a phenomenological Hamiltonian in conjunction with quantum chemical calculations, in order to study the photophysics of pentacene. They state that the lowest singlet exciton has a huge contribution (up to 50%) from CT configurations and this is the main responsible for Davydov splitting in pentacene. Also ME has a similar contribution from CT excitations; therefore, S1 and ME can be almost simultaneously populated when close in energy. Either wise, fast SF could still occur with a CT mediated mechanism[26, 136].

In our approach to SF, we aim to study, with a model Hamiltonian, the electronic structure of a linear chain of molecules undergoing SF, the coupling among S_1 and ME states, and hence test the applicability of Fermi golden rule for the study of the ME←S_1 transition in condensed phase, including an explicit modeling of molecular normal modes, in order to describe ME vibronic states. Our approach is hence focused on surpassing the limitations of theoretical methods employed in the recent literature. In fact, the subject of most of the current studies is a dimer model or *ab initio* calculations on dimers. These approaches are unable to reveal the complete physical picture of a condensed phase system, like organic crystalline materials, since in a dimer the localization of the ME state is imposed by the dimensions of the system, while in a more realistic description the two pseudo-triplets composing the ME could be localized

on different sites, or delocalized over a number of sites. However, *ab initio* calculations of the singles and double excitations of large clusters of molecules are computationally unfeasible, and, hence also models based on them cannot be improved. Moreover, the description of SF dynamics practiced by current models usually do not include explicitly molecular normal modes, whose effect is potentially critical. In Chapters 6 and 7 we present in detail our model and the results obtained for the electronic structure of a linear chain of molecules and for Fermi golden rule rates for the ME←S_1 transition, respectively.

1.7 Thesis outline

In Chapter 2 we define the theoretical bases of our study, in particular we describe in detail the matrix partitioning scheme largely employed in this thesis and the quantum chemistry methods used in conjuction with our theoretical models. In Chapter 3, we report a high throughput study on electron injection times for phosphonated organic dyes in DSSCs. Results are compared with available experiments, providing a proof for the validity of our partitioning approach, that is further employed in Chapter 4 where we report a systematic study of the attachment chemistry along with adsorption energies, and electron injection properties on TiO_2 surfaces, of 15 anchoring groups for DSSC dyes, providing useful insights for design of the anchoring group. In Chapter 5 we verify the validity of our approach for metal-organic dyes, studying the attachment chemistry and electron injection properties of the N3 dye on TiO_2, and comparing the electron injection times obtained with the full dye against different models of anchoring group. In Chapter 6 we describe the electronic structure of a cluster of molecules

subjected to SF, with particular focus on different types of ME states, by means of a model CI Hamiltonian and matrix partitioning procedure. In Chapter 7, we test Fermi golden rule for the study of ME←S_1 non radiative decay, including an explicit description of ME normal modes of vibration. Finally, in Chapter 8 concluding remarks and ideas for possible continuation of these studies are reported.

Chapter 2:

Theoretical methods for the study of electron transfer and non-radiative decay processes

2.1 Outline

In this Chapter, we introduce the theoretical methods used in this thesis. We first report a brief summary of the quantum chemistry methods, used in the following chapters for the study of the electronic structure of molecular systems and crystalline solids (Chapters 3-5). A particular attention is given to configuration interaction theory, that has been employed to develop a model Hamiltonian for the study of a linear chain of molecules undergoing SF (Chapters 6-7). Hence, we focus in more detail on the study of the dynamics of electron transfer and non radiative decay processes, via approximated solutions of the time-dependent Schrödinger equation. In particular, (i) we introduce the fundamental concepts of time-dependent perturbation theory and the formulation of the Fermi golden rule that will be used in Chapter 7; (ii) we describe the matrix partitioning scheme and its application to the study of the electron injection process in DSSCs (Chapters 3-5).

2.2 Quantum chemistry methods

The Hamiltonian of a molecular system has the following expression, given by contributions of kinetic energy T and potential energies V of electrons e and nuclei N, thus producing the following time independent Schrödinger equation:

$$[T_N + T_e + V_{NN}(\mathbf{R}) + V_{Ne}(\mathbf{r},\mathbf{R}) + V_{ee}(\mathbf{r})]\Psi(\mathbf{r},\mathbf{R}) = E\Psi(\mathbf{r},\mathbf{R}) \quad (2.1)$$

Where **r** and **R** are the electron and nuclear coordinates, respectively. The solution of this equation is drastically simplified by the Born-Oppenheimer approximation. This is based on the observation that, due to high ratios between masses of nuclei and electrons, time-scales of nuclear and electronic motion are extremely different. Nuclear and electronic degrees of freedom can be, hence, decoupled and the total wavefunction written as the product of a nuclear wavefunction and an electronic one, the latter depending only parametrically on **R**.[137]

$$\Psi(\mathbf{r},\mathbf{R}) = \phi(\mathbf{r},\mathbf{R})\chi(\mathbf{R}) \quad (2.2)$$

A similar decoupling procedure is not possible among electronic degrees of freedom because of the $V_{ee}(\mathbf{r})$ term, preventing a further simplification of the system into one-electron equations. The electronic Hamiltonian of the system has to be approximated; in the following section we describe common approximation procedures.

2.2.1 The Hartree-Fock method

According to the Pauli principle, the wavefunction of two identical fermions has to be anti-symmetric to the exchange of particles. Hence, the wavefunction of a many electron system has to be anti-symmetric to the exchange of two electrons. This is

obtained by expressing the wavefunction of a system of N electrons, as a determinant (the Slater determinant), which is anti-symmetric if two rows are exchanged[138]:

$$\psi(\mathbf{r}) = (N!)^{-\frac{1}{2}}\det[\chi_a(1)\chi_b(2)\dots\chi_z(N)] \tag{2.3}$$

where $\{\chi_i\}$ is a set of orthonormal spin-orbitals. In the Hartree Fock (HF) method, the energy of a spin orbital is determined, treating the electron-electron repulsion in an average way. This is done by defining the Fock operator $\hat{f}_i$ and solving the HF equations:

$$\hat{f}_i = \hat{h}_i + v_{HF}(i) \tag{2.4}$$

$$\hat{H}_{HF} = \sum_i^N \hat{f}_i \tag{2.5}$$

$$\hat{f}_i\chi(\mathbf{x}_i) = \varepsilon_i\chi(\mathbf{x}_i) \tag{2.6}$$

$\hat{h}_i$ contains one-electron terms, while $v_{HF}(i)$ represents the average potential acting on the *i*-th electron, due to all the other electrons. The explicit expression of $v_{HF}(i)$ represents the core of the HF approximation:

$$v_{HF}(i) = \sum_j \int \frac{|\chi_j(\mathbf{x}_j)|^2}{r_{ij}}\,\mathrm{d}\mathbf{x}_j - \sum_j \int \chi_j^*(\mathbf{x}_j)\frac{1}{r_{ij}}\chi_i(\mathbf{x}_j)\,\mathrm{d}\mathbf{x}_j \tag{2.7}$$

The first and second terms of the right side of Eq. 2.7 are the Coulomb operator, $\hat{J}_i$, and the exchange operator $\hat{K}_i$, respectively, and represent the total electronic repulsion considered in HF method.

Since $v_{HF}(i)$ depends on all the other spin-orbitals, HF equation is non linear and has to be solved through an iterative procedure called the self consistent field (SCF)

method: the Fock operator is built from a trial set of spin orbitals, the HF equation is then solved providing a new set of spin-orbitals, which, in turn produces a new Fock operator. This iterative procedure is repeated until convergence.

The HF method does not include, by definition, the correlation energy,[138] which is defined as:

$$E_c = \mathcal{E}_0 - E_{HF} \tag{2.8}$$

Where E_{HF} is the HF energy and $\mathcal{E}_0$ is the exact non-relativistic energy of the system.[139] Being a single-determinant approximation, HF method is incapable of describing this energy, whose physical meaning can be expressed in two contributions: (i) a static contribution which is due to the unsuitableness of a single-determinant approximation in describing the ground state of nearly degenerate systems (i.e. d^1 orbital of transition metals or bond dissociation) (ii) a dynamical contribution which is related to the correlated movement of electrons, which avoid one another in their motion. There are different ways to overcome this limitation of HF method; i.e. in density functional theory (Section 2.2.2) both exchange and correlation are handled in an approximated way, while post-HF methods, such as configuration interaction theory (Section 2.2.5), go beyond the single-determinant picture, describing the wavefunction as a linear combination of Slater determinants.

2.2.2 Density functional theory

Density functional theory (DFT) studies the interacting many-body system, adopting an auxiliary non interacting analog, the Kohn-Sham system, which is numerically tractable. The one-to-one correspondence between interacting and non-interacting systems has to be approximated in practice, even if it is exact in principle.[140]

DFT was proposed by Kohn and Honenberg[141], who demonstrated that the electron density ρ of the ground state of a system of N electrons uniquely determines the Hamiltonian and all the properties of the ground state, which are expressed as functionals of the electron density. This method is in principle very convenient, since it allows to describe a system of $3N$ coordinates in terms of a single function of 3 coordinates, the electron density. Moreover, the energy of the system, expressed as a functional of the electron density, $E(\rho)$, obeys to a minimization principle; hence, the energy of the ground state is given by the minimum value of $E(\rho)$. For the variational principle, the lowest value of $E(\rho)$ is delivered only if the true ρ is given. The exact ground state electronic energy of the system is:

$$E(\rho) = T + V_{ne} + V_{ee} + E_{XC} \tag{2.9}$$

$$E(\rho) = -\frac{\hbar^2}{2m_e}\sum_{i=1}^{n}\psi_i^*(\mathbf{r}_1)\nabla_{\mathrm{i}}^2\psi_i(\mathbf{r}_1)\mathrm{d}\mathbf{r}_1 - j_0\sum_{I=1}^{N}\int\frac{Z_1}{r_{I1}}\rho(\mathbf{r}_1)\,\mathrm{d}\mathbf{r}_1 +$$

$$+\frac{1}{2}j_0\int\frac{\rho(\mathbf{r}_1)\rho(\mathbf{r}_2)}{r_{12}}\mathrm{d}\mathbf{r}_1\mathrm{d}\mathbf{r}_2 + E_{XC}(\rho) \tag{2.10}$$

Where $\{\psi_i\}$ are the Kohn Sham orbitals, relative to a fictitious non interacting system, and $j_0 = e^2/4\pi\varepsilon_0$. In fact, Kohn and Sham developed the idea of an auxiliary system whose density is equal to the interactive many-body system one, which is intractable because V_{ee} cannot be broken in sum of terms containing only $\mathbf{r}_1$ and $\mathbf{r}_2$.[142] The Kohn-Sham equations define the orbitals of such a system, from which the electron density is easily computed:

$$\left\{\frac{\hbar^2}{2m_e}\nabla_{\mathrm{i}}^2 - j_0\sum_{n=1}^{N}\int\frac{Z_{n1}}{r_{n1}} + j_0\int\frac{\rho(\mathbf{r}_2)}{r_{12}}\mathrm{d}\mathbf{r}_2 + V_{XC}(\mathbf{r}_1)\right\}\psi_i(\mathbf{r}_1) = \varepsilon_i\psi_i(\mathbf{r}_1) \tag{2.11}$$

$$\rho(\mathbf{r}) = \sum_{i=1}^{n} |\psi_i(\mathbf{r})|^2 \tag{2.12}$$

In this framework, the interacting many-body system is converted in a system of non interacting particles, immersed in an effective potential which describes the external potential, Coulomb interactions among electrons and includes exchange and correlation interactions V_{XC}. However, this last term represents the main issue of Kohn-Sham DFT. In fact, for all the terms appearing in Eq. 2.10 an explicit form is given, except for the exchange-correlation functional $E_{XC}(\rho)$, which is not known. One of the major challenges of DFT is the search for approximate expressions of $E_{XC}(\rho)$: one-electron potential functionals are used to approximate the exchange-correlation energy and the calculated DFT results depend on the form of the functional. The development of new and more accurate functionals is still one of the main research topics in this area.[143] There is a wide variety of functionals that have been developed in the last decades but we can group them in few families differing for the nature of the approximation: (i) the local density approximation (LDA) where the exchange energy of a system with non homogenous density is approximated to the exchange of the homogeneous electron gas (derived by Bloch and Dirac)[144] having the same electron density of the system for each point the exchange energy is computed:

$$E_{XC}(\rho) = E_X + E_C \tag{2.13}$$

$$E_X = -\frac{3}{4}\left(\frac{3\rho}{\pi}\right)^{1/3} \tag{2.14}$$

There is no explicit expression for correlation energy E_C but accurate numerical estimations for the homogenous electron gas are available; (ii) the generalized gradient

approximation (GGA) is another local approximation which supplements the density at a particular point with its gradient, to describe the non homogeneity of the true electron density; (iii) hybrid functionals are linear combinations of exact exchange derived from HF theory and any exchange and correlation functional. The relative weights of these two components are usually determined semi-empirically. Most of hybrid functionals combines LDA and/or GGA functionals with HF exchange integral at a constant rate. Some functionals also include long range corrections, where the parameters are distance dependent, in order to fix long range electron-electron interactions, which are underestimated by local approximations.[145] The introduction of a portion of HF exchange improves the accuracy in the prediction of HOMO-LUMO gaps. Nevertheless, there are few major drawbacks in DFT such as the artificial delocalization of the wavefunction and its failure in describing correctly localized charged states. Notwithstanding its current limitations[146], DFT is ubiquitous in quantum chemistry as it outcompetes HF in terms of computational efficiency and accuracy, yielding to reliable predictions of a large number of physical quantities (i.e. reaction energies, cohesive energies in solids, surface energies, vibrational frequencies, phonon spectra, etc).[146] In this framework, probably the most popular functional is the hybrid functional B3LYP (Becke, three-parameter, Lee-Yang-Parr) which presents the following expression[147]:

$$E_{XC}^{B3LYP} = E_X^{LDA} + a_0(E_X^{HF} - E_X^{HF}) + a_X\left(E_X^{GGA} - E_X^{LDA}\right) + E_C^{LDA} + a_C\left(E_C^{GGA} - E_C^{LDA}\right) \quad (2.15)$$

This is a combination of Becke 1988 (B88) exchange and Lee-Yang-Parr (LYP) correlation GGA functionals, Slater (S) exchange and Vosko-Wilk-Nusair (VWN) correlation LDA functional. The three parameters a_0, a_X and a_C are evaluated from fitting to a set of atomization energies, ionization potentials, proton affinities, and total

atomic energies. The B3LYP functional provides a satisfactory description of electronic structure of most organic and metal organic molecules[109] and it is well suited for the study of the TiO_2 electronic structure.[148] Therefore, this functional is used in this thesis, for both calculations on isolated molecules and molecules covalently attached to TiO_2 slabs, in Chapters 3-5.

2.2.3 Density functional theory for periodic systems

The application of DFT to periodic systems like crystalline materials is, at first glance, unfeasible. In fact, while in such systems the external potential $V_{ext}(\mathbf{r})$ possesses a translational symmetry, $\psi(\mathbf{r})$ does not. Therefore, one should solve $\psi(\mathbf{r})$ for an infinite number of electrons in an infinite space. Bloch's theorem overcomes this obstacle, proving that, in a system where $V_{ext}(\mathbf{r})$ has a translational symmetry, the wavefunction (Bloch wave) can be written in the following form:

$$\psi_{\mathbf{k}}(\mathbf{r}) = u(\mathbf{r})e^{(\mathbf{ik}\cdot\mathbf{r})} \tag{2.16}$$

The equation above defines the Bloch wavefunction and means that, in a periodic system, the wavefunction is expressed as the product of a function u, which has the same periodicity of the lattice crystal, and a wavelike function.[144] $\mathbf{k}$ is the crystal wave vector, which, in principle, still needs to be sampled over an infinite space, since at each $\mathbf{k}$-point corresponds a set of electronic states. However, it is possible to obtain a good approximation of the band structure of a periodic system, considering that (i) any solution of the Schrödinger equation, $\psi_{\mathbf{k}}(\mathbf{r})$, possesses the following property:

$$\psi_{\mathbf{k}}(\mathbf{r}+\mathbf{T}) = \psi_{\mathbf{k}}(\mathbf{r})e^{(\mathbf{ik}\cdot\mathbf{T})} \tag{2.17}$$

Where **T** is a translation vector for the considered lattice. Hence $\psi_{\mathbf{k}}(\mathbf{r})$ differs only by a phase factor if we consider equivalent positions in the lattice. Since $[e^{(i\mathbf{k}\cdot\mathbf{T})}]^2 = 1$, this implies that :

$$|\psi_{\mathbf{k}}(\mathbf{r}+\mathbf{T})|^2 = |\psi_{\mathbf{k}}(\mathbf{r})|^2 \tag{2.18}$$

Therefore, for every equivalent position in the lattice vector, the probability of finding an electron is the same; (ii) the primitive unit cell of the reciprocal lattice (the first Brillouin zone) contains all the non equivalent values of **k** for the system under study; (iii) $\psi_{\mathbf{k}}$ is a continuous function of **k**. Hence, a clever choice of a finite number of **k** in the first Brillouin zone can provide a good approximation of the **k**-space. In this thesis we perform DFT calculations on periodic crystalline systems, adopting the sampling of **k**-space proposed by Monkhorst and Pack.[149] Their method provides an equally space mesh in the Brillouin zone:

$$\mathbf{k} = \sum_{i=1}^{3} \frac{2r_i - q_i - 1}{2q_i} \mathbf{b_i} \; (r_i = 1, \dots, q_i) \tag{2.19}$$

where $\{\mathbf{b_i}\}$ are the reciprocal lattice vectors and q_i is the number of **k** points along $\mathbf{b_i}$. In this way, a grid of equally spaced $q_i \times q_2 \times q_3$ points is generated.

2.2.4 Time dependent density functional theory

TD-DFT is an extension of density functional theory to systems subject to a time dependent potential (i.e. electric or magnetic fields). It shares the same concept of DFT: the time-dependent wavefunction is equivalent to the time-dependent electron density and, again, the interacting system can be expressed as a non-interactive one immersed in an effective potential. The formal basis of TD-DFT is the Runge-Gross theorem, the

time dependent analogue of the Hohenberg-Kohn theorem.[150] Runge and Gross demonstrated that, if two time-dependent external potentials differ by more than a pure time dependent function, they will produce different time-dependent electron densities:

$$v(\mathbf{r},t) \neq v'(\mathbf{r},t) + c(t) \Rightarrow \rho(\mathbf{r},t) \neq \rho'(\mathbf{r},t) \tag{2.20}$$

Therefore, for an initial wavefunction, there is an unique correspondence between the time-dependent external potential and its time-dependent density. As in the case of DFT, a feasible computational method requires the description of the interacting system as a non-interacting one which provide the same electron density. Again, Kohn-Sham equations can be reformulated for the time dependent case, providing time dependent Kohn-Sham orbitals[151]:

$$\mathrm{i}\frac{\partial}{\partial t}\psi_i(\mathbf{r},t) = \left\{-\frac{1}{2}\nabla_{\mathrm{i}}^2 + V_{ext}(\mathbf{r},t) - V_{XC}(\mathbf{r},t)\right\}\psi_i(\mathbf{r},t) \tag{2.21}$$

$$\rho(\mathbf{r},t) = \sum_{i=1}^{n} |\,\psi_i(\mathbf{r},t)|^2 \tag{2.22}$$

TD-DFT has been intensively used for the study of excited states of DSSC dyes, both for the isolated molecule and for the molecule attached to the semiconductor surface.[109, 110] In Chapter 4, TD-DFT calculations are used to compute excitation energies and oscillator strengths for singlet excited states for several dyes.

Since the total energy for a time dependent system is not conserved, TD-DFT obeys to no minimization principle of the energy, which represent an important drawback of the method, as it is incapable of providing optimized electronic structures of excited states. Another unsolved issue is the impossibility of characterizing double excited states, through electron density. For these reasons, TD-DFT, while being one of the simplest

and most used method for the study of excited states, it has only played a marginal role in theoretical studies on the mechanism of SF. TD-DFT calculations have only been used to compute single excitations energies, in isolated molecules and clusters, in order to study the Frenkel exciton and its delocalization.[29, 30]

2.2.5 Configuration interaction theory

Configuration interaction (CI) theory is a post-HF method, which was conceived to correct E_{HF} of the electronic ground state, including correlation energy. While in HF approximation, the wavefunction is described by a single Slater determinant, the exact energy of the system can be obtained only if the wavefunction is expressed as a linear combination of an infinite number of Slater determinants (configurations)[138]:

$$\Phi_{\mathrm{CI}} = c_0|\Psi_0\rangle + \sum_{ij}^{N} c_i^j\,|\Psi_i^j\rangle + \sum_{\substack{i<k\\ j<l}}^{N} c_{ik}^{jl}\,|\Psi_{ik}^{jl}\rangle + \sum_{\substack{i<k<m\\ j<l<n}}^{N} c_{ikm}^{jln}\,|\Psi_{ikm}^{jln}\rangle + \ \ldots \qquad (2.23)$$

Eq. 2.23 is the full CI wavefunction where (i) $|\Psi_0\rangle$ is the HF wavefunction of the ground state; (ii) $|\Psi_{ikm\ldots}^{jln\ldots}\rangle$ indicates an excited Slater determinant. For example, $|\Psi_i^j\rangle$ indicates a determinant where an electron, located in the ground state in the χ_i occupied spin-orbital, is promoted to the virtual χ_j spin orbital. $|\Psi_i^j\rangle$ is called a single excited determinant, $|\Psi_{ik}^{jl}\rangle$ is a double excited determinant and so on; Summations are carried out in order to include all the possible combinations of occupied and virtual spin orbitals; (iii) c_0, c_i^j, $c_{ik\ldots}^{jl\ldots}$ are the expansion coefficients of the wavefunction, which are computed diagonalizing the full CI Hamiltonian. In order to express the full CI Hamiltonian, we can simplify Eq. 2.23 with a compact notation:

$$\Phi_{\mathrm{CI}} = c_0|\Psi_0\rangle + c_s|S\rangle + c_d|D\rangle + +c_T|T\rangle + +c_Q|Q\rangle + \cdots \tag{2.24}$$

where $|S\rangle$ includes terms for single excitations, $|D\rangle$ for doubles and so on. The full CI Hamiltonian is hence written in the following form:

$$H_{\mathrm{CI}} = \begin{pmatrix} \langle\Psi_0|H|\Psi_0\rangle & \langle\Psi_0|H|\mathrm{S}\rangle & \langle\Psi_0|H|\mathrm{D}\rangle & \langle\Psi_0|H|\mathrm{T}\rangle & \ldots \\ & \langle\mathrm{S}|H|\mathrm{S}\rangle & \langle\mathrm{S}|H|\mathrm{D}\rangle & \langle\mathrm{S}|H|\mathrm{T}\rangle & \ldots \\ & & \langle\mathrm{D}|H|\mathrm{D}\rangle & \langle\mathrm{D}|H|\mathrm{T}\rangle & \ldots \\ & & & \langle\mathrm{T}|H|\mathrm{T}\rangle & \ldots \\ & & & & \ddots \end{pmatrix} \tag{2.25}$$

Matrix elements of the CI Hamiltonian can be computed with the Slater rules. These rules allow to express the matrix elements in term of one- and two-electron integrals, described with the following notation:

$$\langle a|\hat{h}|b\rangle = \int \chi_a^*(\mathbf{x}_1)\hat{h}\chi_b(\mathbf{x}_1)\mathrm{d}\mathbf{x}_1\mathrm{d}\mathbf{x}_2 \tag{2.26}$$

$$\langle ab\|cd\rangle = \langle ab|cd\rangle - \langle ab|dc\rangle \tag{2.27}$$

$$\langle ab|cd\rangle = \int \chi_a^*(\mathbf{x}_1)\chi_b^*(\mathbf{x}_2)\frac{1}{r_{12}}\chi_c(\mathbf{x}_1)\chi_d(\mathbf{x}_2)\mathrm{d}\mathbf{x}_1\mathrm{d}\mathbf{x}_2 \tag{2.28}$$

a) for two equal Slater determinants:

$$\langle\psi_i|\hat{H}|\psi_i\rangle = \sum_a^N \langle a|\hat{h}|a\rangle + \sum_{a>n}^N \langle an\|cn\rangle \tag{2.29}$$

b) for two Slater determinants differing for one spin orbital (a and c):

$$\langle\psi_i|\hat{H}|\psi_j\rangle = \langle a|\hat{h}|c\rangle + \sum_n^N \langle an\|cn\rangle \tag{2.30}$$

c) for Slater determinants differing for two spin orbitals (ab and cd):

$$\langle \psi_i | \hat{H} | \psi_j \rangle = \langle ab \| cd \rangle \tag{2.31}$$

d) Slater determinants differing for more than two spin orbitals do not mix with each other.

These rules are justified in detail in ref.[138] A full CI description of the electronic structure is unfeasible, except for the smallest systems with a minimal basis set, because the number of possible excited determinants sharply increases, with the number of exchanged spin-orbitals. In practice, the CI wavefunction is truncated, excluding high order excited determinants. The most used types of truncation are (i) the single excited CI (CIS) including only single excited determinants; (ii) double excited CI (DCI); (iii) the single and double excited CI (SDCI) including single and double excited determinants.

CIS is a good starting point for the study and optimization of excited states, being computationally viable for large systems, due to the small number of combinations available for single excited determinants. However, no direct correction of the HF energy of the ground state is possible with this method. This is a consequence of Brillouin's theorem, stating that singly excited determinants do not interact with $|\Psi_0\rangle$.[138] In fact it is proven that:

$$\langle \psi_0 | \hat{H} | \psi_a^c \rangle = \langle \chi_a | \hat{f} | \chi_c \rangle = 0 \tag{2.32}$$

Where the left side of the Eq. 2.32 is an off-diagonal term of the Fock matrix, which is zero, by definition. The only matrix elements to be considered are the ones between different single excited determinants, that can differ for one or two spin electrons .The main drawback of CIS stays in the incapability of describing excited states which are

not dominated by single excitations; for those systems other high level wavefunction-based methods are preferred.

DCI is the simplest method to correct the energy of the ground state, providing the major contribution to the correlation energy. In fact, as a consequence of Slater rules and Brillouin's theorem, $|\Psi_0\rangle$ does mix directly only with double excited determinants, all of them differing with $|\Psi_0\rangle$ for two spin orbitals. However, while single excited determinants minimally affect the correlation energy, they are fundamental in the correct description of charge density and the related physical properties.[138]

Since the inclusion of single excited determinants is not computational demanding, being their number sensibly lower than double excited ones, the most popular CI approach, SDCI, implements both, representing a viable method for the study of both correlation energies and excited states. Nevertheless, every truncation of the full CI is not size consistent; hence, if a system of two non interacting molecules is considered, the total SDCI energy is not the sum of the individual energies, because this type of truncation prevents both molecules from being doubly excited at the same time (an overall quadruple excitation), thus missing important contributions to the correlation energy.[138] This effect becomes worse for large systems and the computed correlation energy tends to zero, in the limit of a system of infinite size (infinite number of molecules N).

$$\lim_{N\to\infty} \frac{E_C(\mathrm{SDCI})}{N} = 0 \tag{2.33}$$

In Chapter 6, we propose a model dimer SDCI Hamiltonian, where each monomer possesses two orbitals (namely, HOMO and LUMO), in order to study the electronic

structure of a cluster of molecules undergoing SF. While we are aware of the issues of SDCI, we are not interested in computing correlation energies but in the calculations of energies of excited states, where CI theory represents the only viable choice to fulfill our goals.

Previous works[28, 29] on excited states of systems undergoing SF employed other post-HF methods such as CAS-SCF (complete active space self consistent field) combined with multi-reference Møller-Plesser (MP) perturbation theory method[152]. Electronic structures of dimers, taken from the crystallographic structure of pentacene and tetracene, were computed. In CAS-SCF a truncated CI approach is adopted, where both expansion coefficients and orbitals are simultaneously optimized, following the variational principle.[138] The complexity of this non-linear problem limits the truncation of the wavefunction, if compared to CI. A selection of the possible configurations is provided by partitioning the orbital space in different subspaces. In complete CAS-SCF the orbital space is divided in three portions: inactive, active and secondary orbitals. The inactive and secondary orbitals are always totally occupied or unoccupied, respectively, for every considered configuration, while the active orbitals (usually a selection of frontier orbitals) are subject to no condition on their occupation. Hence, all the possible combinations in the active space constitute the set of available configurations. This method, while being suitable for the study of excited states, is limited by its computational complexity, due to the size dependence of the active space and by the difficulty of the simultaneous optimization of both wavefunctions and coefficients. Moreover CAS-SCF calculations somewhat overestimate excitation energies. For these reasons, CAS-SCF wavefunctions are typically used as initial guess for other high-level wavefunction methods, typically MP calculations. In fact,

corrections to HF method, provided by MP perturbation theory, suffer from the major drawback that are obtained with HF orbitals, which could be unsuitable for describing a multi-reference system. Therefore, using CAS-SCF in conjunction with MP calculations minimizes the drawbacks of both methods.

Notwithstanding the high level of accuracy reached by these methods, they are inadequate for our purposes. In fact, while previous works have restricted the analysis of SF in crystalline organic materials to the study of the electronic structure of a dimer system[28-31], we aim to overcome this limitation that does not allow to gain a complete physical picture of a process occurring in an organic crystal. This is not possible with these methods, due to the computational cost that makes impossible the description of large clusters (i.e. in a CAS-SCF calculation for 10 molecules, if just the active space is restricted to HOMO and LUMO of each molecule, the number of possible excited determinants would be enormous). Moreover, results obtained from calculations on dimers cannot provide general insights on the physical parameters affecting the SF process. For these reasons, we chose to use SDCI,in order to develop a minimal model Hamiltonian, mimicking the electronic structure of a linear chain of molecules (Chapter 6), where parameters can be tuned to simulate different materials. In this way, we adopt a conceptually intuitive method as CI, we avoid drawbacks due to an excessive computational cost, affecting calculations on more realistic systems, and we can investigate in detail which parameters play a key role in the physics of the system.

2.2.6 Basis sets

The wavefunction of a system is commonly expressed as a linear combination of a certain number of basis functions:

$$|\psi_i\rangle = \sum_j c_{ij}|\,\phi_j\rangle \tag{2.34}$$

$\{\phi_j\}$ represents the basis set for computing the wavefunction. Once a basis set has been defined, we just need to find the best set of coefficients $\{c_{ij}\}$. In principle, the true wavefunction of the system is provided only within a complete set of basis, which is infinite and, obviously, computationally intractable. Finite basis sets represent a viable solution and there is a wide literature on available basis sets.[153] We can define three distinct families of basis sets, differing for the nature of the basis functions: (i) Slater type orbitals (STO), (ii) Gaussian type orbitals (GTO) and (iii) planewaves. In the early days of quantum chemistry, STOs were adopted because of their similarity to hydrogen atom eigenfunction; a STO is expressed in polar coordinates as follows:

$$\mathrm{STO}(r,\vartheta,\varphi) = Nr^{n-1}e^{-\zeta r}\mathrm{Y}_l^m(\vartheta,\varphi) \tag{2.35}$$

Where N is a normalization factor, r is the electron-nucleus distance, ζ is a parameter representing a shielding of the nuclear charge, due to the electrons, and $\mathrm{Y}_l^m(\vartheta,\varphi)$ is a spherical harmonics function. STOs, while providing a direct physical interpretation, present major drawbacks in terms of computational efficiency. In particular, products of STOs are difficult to handle and integrals occurring in the SCF procedure have to be calculated with a computational demanding numerical procedure. A practical improvement has been provided by GTOs, which have the following form:

$$\mathrm{GTO}(\mathbf{r}) = N(x-R_1)^i(y-R_2)^j(z-R_3)^k e^{-\alpha(\mathbf{r}-\mathbf{R})^2} \tag{2.36}$$

where **R** and α are defined as the centre (usually the position of the atomic nucleus), and the exponent of the GTO, respectively. GTOs are not proper orbitals (they are also

called gaussian primitives) but possess a similar shape, even if in GTOs the variable **r** is squared. The type of GTO is determined by the i, j, k numbers: if their product is 0 we obtain an s-type GTO, if is 1 we have a p-type GTO and so on. The main advantage in using GTOs is that products of primitives centered on different atoms, labeled as a and b, can be expressed as follows:

$$\mathrm{GTO}(\mathbf{a})\mathrm{GTO}(\mathbf{b}) \cong e^{-\alpha_\mathrm{a}(\mathbf{r}-\mathbf{R_a})^2} e^{-\alpha_\mathrm{b}(\mathbf{r}-\mathbf{R_b})^2} = e^{-(\alpha_\mathrm{a}+\alpha_\mathrm{b})(\mathbf{r}-\mathbf{R}')^2} e^{-\alpha'(\mathbf{R_a}-\mathbf{R_b})^2} \tag{2.37}$$

$$\mathbf{R}' = \frac{\alpha_\mathrm{a}\mathbf{R_a} + \alpha_\mathrm{b}\mathbf{R_b}}{\alpha_\mathrm{a} + \alpha_\mathrm{b}} \tag{2.38}$$

$$\alpha' = \frac{\alpha_\mathrm{a}\alpha_\mathrm{b}}{\alpha_\mathrm{a} + \alpha_\mathrm{b}} \tag{2.39}$$

Therefore, a product of two GTOs centered on different atoms can be expressed as single GTO whose center $\mathbf{R}'$ is located between the centers of the initial GTOs.

In this thesis we use GTO basis sets; in particular we use, for most of our calculations, the 6-31G* basis set[154-156] (use of other basis sets is specified where pertinent). This acronym means that linear combinations of six (6) Gaussian (G) primitives are used to define the core orbitals, while the valence orbitals are divided between 2 basis functions: a linear combination of three (3) and a single (1) GTO, respectively. The symbol "*" indicates the use of polarization functions (d and f functions for main group elements and transition metals, respectively).

While GTOs are ubiquitous in *ab initio* calculations of molecular systems, a main alternative does exist for calculations on periodic systems and it is given by planewaves. A planewave is defined as a periodic function, whose periodicity is the same of the system under study:

$$\phi = e^{-i(\mathbf{k}+\mathbf{G})\cdot\mathbf{r}} \tag{2.40}$$

While in GTOs the number of gaussian primitives defines the size of the basis set and each GTO needs a large number of parameters to be optimized, the size of a planewave basis set is established by an energy cut-off. In fact, in the description of valence electrons of a solid, planewaves of high kinetic energy can be neglected. The basis set can be improved adjusting a single parameter (the energy cut-off); nevertheless, a large number of planewaves are required to obtain the same computational accuracy that is provided by few gaussian primitives. In term of computational cost, planewaves are preferred in *ab initio* molecular dynamics since are easier to handle in algorithms. However, planewaves cannot provide an all-electron description as GTOs, since modeling the rapidly varying wavefunction near the nuclei, along with multiple nodes, would require an extremely high energy cut-off. Therefore, planewaves are usually used in conjunction with pseupotentials, which describe core electrons.

2.3 Methods for theoretical evaluation of rates of electron transfer and radiationless decay

In this section, we introduce the theoretical foundations for the calculation of electron transfer and radiationless decay rates, performed in this thesis. For both electron injection in DSSCs and radiationless decay processes in SF, we adopt the physical picture, common to a variety of dynamical processes, of the transition from an initial state to a manifold of final states (see **Figure 2.1**). In the study of electron injection in DSSCs (Chapters 3-5), the initial state is an excited state, localized on a dye molecule

and dominated by the HOMO-LUMO excitation. The manifold of final states is constituted by the electronic states of the CB of TiO_2. Phonon degrees of freedom play no role and the electronic coupling between the molecule and the semiconductor is mediated by a molecular linker (the anchoring group). On the other hand, in our study of the mechanism of SF in organic crystalline materials (Chapters 6-7), we investigate the transition from an initially prepared Frenkel exciton state to a multi-excitonic state. In this case, the manifold of final states is given by the vibronic states of the multi-exciton, for which a model is provided in Chapter 7. The electronic coupling between the Frenkel exciton and the multi-excitonic state has to be weighed with the Franck-Condor factors. Notwithstanding the differences between these two phenomena, both can be studied with time dependent perturbation theory. In particular, for the study of the ME←S_1 radiationless decay, we adopt a wavefunction's approach as we compute transition rates using Fermi golden rule. On the other hand, the study of electron injection rates in DSSCs is performed within the framework of Green's functions, combined with a matrix partitioning scheme.

2.3.1 Time dependent perturbation theory and Fermi golden rule

Time dependent perturbation theory studies how a system responds to an external perturbation (i.e. an applied electric field) with particular focus on perturbation-induced transitions between eigenstates of the unperturbed system.[157] In time dependent perturbation theory, the Hamiltonian of a system and the time dependent Schrödinger equation are expressed in the following form:

$$\widehat{H}(t) = \widehat{H}_0 + \widehat{H}'(t) \tag{2.41}$$

$$|\widehat{H}_0 + \widehat{H}'(t)||\Psi(\mathrm{t})\rangle = \mathrm{i}\hbar\frac{\partial}{\partial t}|\Psi(\mathrm{t})\rangle \tag{2.42}$$

Where $\widehat{H}_0$ is the Hamiltonian of the unperturbed system, for which the Schrödinger equation can be solved, while $\widehat{H}'(t)$ is a time-dependent perturbation. At zeroth order, $\widehat{H}_0$ has E_n eigenvalues and ψ_n eigenvectors. The wavefunction of the system $|\Psi\rangle$ at a given time t can be expressed as linear combination of ψ_n:

$$|\Psi(\mathrm{t})\rangle = \sum_n c_n(t)\, e^{-\frac{iE_n t}{\hbar}} |\,\psi_n\rangle \tag{2.43}$$

Where $c_n(t)$ are expansion coefficients conveying the time dependence of $|\Psi(\mathrm{t})\rangle$, along with the phase factor $e^{-iE_n t/\hbar}$. Eq. 2.42 then becomes:

$$\left|\widehat{H}_0 + \widehat{H}'(t)\right| \sum_n c_n(t)\, e^{-\frac{iE_n t}{\hbar}} |\,\psi_n\rangle = \frac{\partial}{\partial t} \sum_n c_n(t)\, e^{-\frac{iE_n t}{\hbar}} |\psi_n\rangle \tag{2.44}$$

If we take the inner product with the bra $\langle\psi_m| e^{-iE_m t/\hbar}$ and introduce the notations $\omega_{mn} = \frac{E_m - E_n}{\hbar}$ and $V_{mn} = \left\langle\psi_m\left|\widehat{H}'(t)\right|\psi_n\right\rangle$ we obtain the following expression:

$$\frac{dc_m}{dt} = -\frac{\mathrm{i}}{\hbar} \sum_n c_n(t)\, e^{-\mathrm{i}\omega_{mn} t/\hbar} V_{mn} \tag{2.45}$$

We assume that, before the perturbation has been switched on, the system is in an initial state i. Replacing all the coefficients with their value at $t = 0$, every coefficient except one is eliminated. This is a weak perturbation limit, since we are assuming that the coefficients do not differ largely from their unperturbed value, as $\widehat{H}'(t)$ is small. The time dependent coefficient for a generic final state $f \neq i$ is given by the following expression[157]:

$$c_f(t) = -\frac{\mathrm{i}}{\hbar} \int_0^t V_{fi}(t') e^{\mathrm{i}\omega_{fi} t'} dt' \tag{2.46}$$

The square of the amplitude of the coefficient provides the transition probability from the initial state ($t = 0$) to the final state ($t \neq 0$):

$$P_f(t) = \frac{1}{\hbar^2}\left|\int_0^t V_{fi}(t')e^{i\omega_{fi}t'}dt'\right|^2 \tag{2.47}$$

This expression is useful if we are interested on the probability of leaving a state. This is common for processes where we want to calculate transition probabilities not to an individual state but to a manifold of final states $\{f\}$, as in the case of the transition from a Frenkel exciton to a manifold of vibronic multi-excitonic states in SF, or in the study of the electron transfer from an excited dye molecule to the conduction band of a semiconductor **(Figure 2.1**).

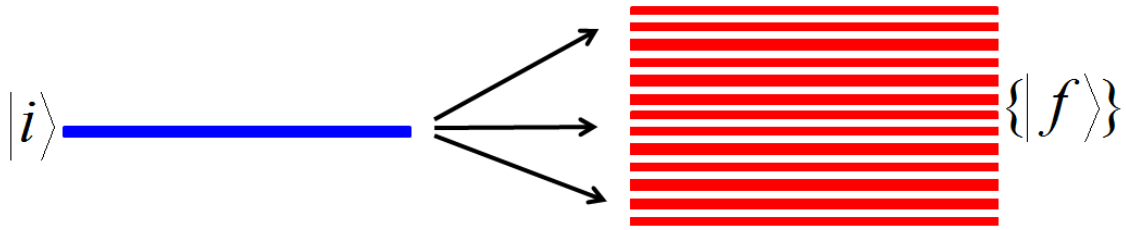

Figure 2.1: schematic representation of a system composed by an initial state |i⟩ coupled with a manifold of final states |f⟩.

In this framework, the total transition probability is given by the following expression, for a continuous distribution of final states:

$$\bar{P} = \int P_f \rho(E_f) dE_f \tag{2.48}$$

Where $\rho(E_f)$ is the density of final states. It is demonstrated that for a harmonic perturbation ($H'(t) = H'e^{-i\omega t} + H'e^{-i\omega t}$) :

$$\bar{P} = \int \rho(E_f)\, 4|V_{fi}|^2 \frac{\sin^2((E_f - E_i)t/2\hbar)}{|E_f - E_i|^2} dE_f \tag{2.49}$$

If we assume that $\rho(E_f)$ is a slowly varying function of E_k, Eq. 2.49 becomes:

$$\bar{P} = 4\rho \int_{-\infty}^{+\infty} |V_{fi}|^2 \frac{\sin^2((E_f - E_i)t/2\hbar)}{|E_f - E_i|^2} dE_k \tag{2.50}$$

The expression of the transition probability is simplified solving the integral:

$$\int_{-\infty}^{+\infty} \frac{\sin^2(a\Delta)}{\Delta^2} d\Delta = a\pi \Longrightarrow \bar{P} = \frac{2\pi}{\hbar} \rho |V_{fi}|^2 t \tag{2.51}$$

Finally, differentiating the transition probability, we obtain the transition rate:

$$k_{i\to\{f\}} = \frac{\partial \bar{P}}{\partial t} = \sum_f \frac{2\pi}{\hbar} \rho |V_{fi}|^2 = \sum_f \frac{2\pi}{\hbar} |V_{fi}|^2 \delta(E_f - E_i) \tag{2.52}$$

where $\delta(E_f - E_i)$ is a delta Dirac function. Eq. 2.52 is the Fermi golden rule (FGR), stating that, at the first order perturbation theory, the rate of transition depends on the square of the V_{fi} matrix element.

In this thesis, FGR is used to study the non radiative decay from a singlet exciton state to a manifold of vibronic multiexcitonic states, for a phenomenological Hamiltonian, mimicking a linear chain of molecules undergoing to SF. In Chapter 7 we specify the details of the system under study and how the FGR has been implemented, along with its limits of applicability.

2.3.3 The matrix partitioning scheme within retarded Green's functions framework

A different approach to the time dependent evolution of a molecular system is given within the framework of retarded Green functions (GFs) and we are going to use this approach, along with a matrix partitioning scheme, to study electron injection in

DSSCs, as ideated by Jones and coworkers.[128] We use this method to study the electron transfer, without considering explicitly all the states of the system.

A retarded GF is an operator defined as follow[158]:

$$\hat{G}(t) = \begin{cases} -\mathrm{i}e^{-(\mathrm{i}\hat{H}t)}, & t > 0 \\ 0, & t < 0 \end{cases} \tag{2.53}$$

Sometimes, it is more useful to express the GF in terms of energy, by applying a Fourier transform:

$$\hat{G}(E) = \int_0^{+\infty} \hat{G}_R(t)\, e^{\left(\frac{\mathrm{i}Et}{\hbar}\right)} dt \tag{2.54}$$

$$\hat{G}(E) = \lim_{\varepsilon \to 0} \left[\frac{1}{(E - \hat{H} + \mathrm{i}\varepsilon)} \right] \tag{2.55}$$

Once the time independent Schrödinger equation for the system has been solved, the GF is given by the following expression:

$$\hat{G} = \sum_n \frac{|\,\psi_n\rangle\langle\psi_n|}{E - E_n + \mathrm{i}\varepsilon} \tag{2.56}$$

For a very large system, we want to evaluate the propagation of only a restricted subset of states of interest, without considering the whole set of states of the Hamiltonian. This goal can be fulfilled by using a partitioning of the Hamiltonian. Once a a basis set $\{\phi_j\}$ of N basis functions is defined (see Eq. 2.34), the separation of the Hamiltonian in two sub-systems is realized defining the projection operators $\hat{P}$ (for the n states of interest) and $\hat{Q}$ (for the remaining states):

$$\hat{P} = \sum_{i=1}^{n} |\phi_i\rangle\langle\phi_i| \tag{2.57}$$

$$\hat{Q} = \sum_{i=n+1}^{N} |\phi_i\rangle\langle\phi_i| \tag{2.58}$$

Time dependent Schrödinger equation can be hence rewritten as:

$$\frac{\partial}{\partial t}\begin{pmatrix}\boldsymbol{c}_P\\ \boldsymbol{c}_Q\end{pmatrix} = -\frac{\mathrm{i}}{\hbar}\begin{pmatrix}\mathbf{H}_{PP} & \mathbf{H}_{PQ}\\ \mathbf{H}_{QP} & \mathbf{H}_{QQ}\end{pmatrix}\begin{pmatrix}\boldsymbol{c}_P\\ \boldsymbol{c}_Q\end{pmatrix} \tag{2.59}$$

Since it is demonstrated that[158]:

$$|\psi(t)\rangle = \hat{G}(t)|\,\psi_o\rangle \tag{2.60}$$

we can express the retarded GF in a partitioned matrix form:

$$\begin{pmatrix}\boldsymbol{c}_P(t)\\ \boldsymbol{c}_Q(t)\end{pmatrix} = \begin{pmatrix}\mathbf{G}_{PP}(t) & \mathbf{G}_{PQ}(t)\\ \mathbf{G}_{QP}(t) & \mathbf{G}_{QQ}(t)\end{pmatrix}\begin{pmatrix}\boldsymbol{c}_P(0)\\ \boldsymbol{c}_Q(0)\end{pmatrix} \tag{2.61}$$

In a similar fashion of what has been done in Section 2.3.2, we can assume that, at $t = 0$, the system is in some initial state and, hence, all the other time dependent expansion coefficients are set to zero. We consider the case that, at $t = 0$, our state of interest is localized in the $\hat{P}$ subspace, thus implying that $\boldsymbol{c}_Q(0) = 0$. The immediate consequence of this statement is that the time dependence of the expansion coefficient $\boldsymbol{c}_P(t)$ is conveyed only by the retarded GF acting on the $\hat{P}$ subspace:

$$\boldsymbol{c}_P(t) = \mathbf{G}_{PP}(t)\boldsymbol{c}_P(0) \tag{2.62}$$

The final goal is finding a tractable expression for $\mathbf{G}_{PP}$. Combining the projection operators description of an Hamiltonian matrix and the fact that the Schrödinger

equation can be written in the matrix form $\mathbf{Mv} = 0$ ($\mathbf{M}$ is a matrix, $\mathbf{v}$ is a vector) we obtain the following expression[159]:

$$\begin{pmatrix} \mathbf{M}_{PP} & \mathbf{M}_{PQ} \\ \mathbf{M}_{QP} & \mathbf{M}_{QQ} \end{pmatrix} \begin{pmatrix} \mathbf{v}_P \\ \mathbf{v}_Q \end{pmatrix} = 0 \tag{2.63}$$

Solving this system of simultaneous equations for $\mathbf{v}_P$, we have:

$$\left[\mathbf{M}_{PP} + \mathbf{M}_{PQ}\left(\mathbf{M}_{QQ}\right)^{-1}\mathbf{M}_{QP}\right]\mathbf{v}_P = 0 \tag{2.64}$$

Analogously, if $\mathbf{M} = E_n\mathbf{1} - \mathbf{H}$,where $\mathbf{1}$ is the unitary matrix and $\mathbf{v} = \boldsymbol{c}_n$, the solution of the Hamiltonian matrix equations for $\mathbf{v}_P$ is the following:

$$\left[\mathbf{H}_{PP} + \mathbf{H}_{PQ}\left(E_n\mathbf{1} - \mathbf{H}_{QQ}\right)^{-1}\mathbf{H}_{QP} - \mathbf{1}E_n\right]\mathbf{v}_P = 0 \tag{2.65}$$

Where we define:

$$\mathbf{H}_{PP}^{eff} = \mathbf{H}_{PP} + \mathbf{H}_{PQ}\left(E\mathbf{1} - \mathbf{H}_{QQ}\right)^{-1}\mathbf{H}_{QP} \tag{2.66}$$

$\mathbf{H}_{PP}^{eff}$ is an effective Hamiltonian of the system, its size being determined by the zeroth order Hamiltonian of the $\hat{P}$ subspace, $\mathbf{H}_{PP}$. The effect of the subspace $\hat{Q}$ on subspace $\hat{P}$ is conveyed through the self energy operator defined as:

$$\mathbf{\Sigma}_{PP} = \mathbf{H}_{PQ}\left(E\mathbf{1} - \mathbf{H}_{QQ}\right)\mathbf{H}_{QP} \tag{2.67}$$

Finally, as we desired, the retarded GF in the subspace $\hat{P}$, $\mathbf{G}_{PP}$, is expressed in terms of an effective Hamiltonian, which includes implicitly all the effects of the $\hat{Q}$ subspace:

$$\mathbf{G}_{PP}(E) = \frac{1}{(E - \mathbf{H}_{PP} - \mathbf{\Sigma}_{PP})} \tag{2.68}$$

2.3.4 Application of matrix partitioning scheme to electron injection in DSSCs

In this section, we consider again the system depicted in **Figure 2.1** (an initial state $|i\rangle$ coupled with a manifold of final states $|f\rangle$) and analyze its time dependent evolution within the framework developed in Section 2.3.3. First, we define the following electronic Hamiltonian for the system:

$$H = E_i|i\rangle\langle i| + \sum_f E_f|f\rangle\langle f| + \sum_f (V_{if}|i\rangle\langle f| + (V_{fi}|f\rangle\langle i|) \tag{2.69}$$

Where $\{V_{if}\}$ represents the coupling matrix elements between the two sets of states. This Hamiltonian is purely electronic as we assume that the transition $i \to \{f\}$ occurs on a time scale faster than nuclear motion, which is the case for most electron injection phenomena. Since we are interested in the time dependent evolution of the initial state, we need to compute its retarded GF:

$$\mathbf{G}_{ii}(E) = \frac{1}{(E - E_i - \mathbf{\Sigma}_{ii}(E))} \tag{2.70}$$

We separate the self energy into real ($\Delta_{ii}(E)$) and imaginary ($\Gamma_{ii}(E)$) components, each having a distinct effect on the time dependent evolution of the system.

$$\mathbf{\Sigma}_{ii}(E) = \sum_f \frac{|V_{if}|^2}{E - E_f + \mathrm{i}\varepsilon} = \Delta_{ii}(E) - \frac{\mathrm{i}}{2}\hbar\Gamma_{ii}(E) \tag{2.71}$$

The different meaning of these two components is highlighted if we apply a Fourier transform into the domain of time:

$$\mathbf{G}_{ii}(t) = \int_{-\infty}^{+\infty} \mathbf{G}_{ii}(E)\, e^{(\mathrm{i}Et/\hbar)} dE = e^{[-\frac{\mathrm{i}(E_i+\Delta_{ii})t}{\hbar} - \frac{\Gamma_{ii}t}{2}]} \tag{2.72}$$

Hence, Δ_{ii} represents a shift on the energy level of the initial state, induced by the interaction with the manifold of final states. On the other hand, $1/\Gamma_{ii}$ is the lifetime of state $|i\rangle$.

Explicit expressions for Δ_{ii} and Γ_{ii} can be derived in terms of V_{if} and energy difference $(E - E_f)$, which are the physical parameters ruling the time-dependent evolution of the system:

$$\Delta_{ii} = \sum_f \frac{V_{fi}V_{fi}^*}{E - E_f} \tag{2.73}$$

$$\hbar\Gamma_{ii} = 2\pi \sum_f V_{fi}V_{fi}^* \, \delta(E - E_f) \tag{2.74}$$

The developed framework is ideal to study the electron injection rates in DSSCs. In fact, electron injection can be defined as a transition from an orbital localized on the dye molecule to a manifold of one-electron states of the continuum formed by the states of the semiconductor's CB. This picture is further simplified, considering that the orbital localized on the chromophore can be identified with its LUMO, if the excited state is dominated by the HOMO→LUMO transition, which is true for many organic chromophores.[160, 161]

If the system under study is simulated by a dye molecule attached covalently on a semiconductor's slab, the partitioning of the Hamiltonian in terms of a molecular and a surface subspaces is immediate. States belonging to the chromophore ($|i\rangle$) and to the semiconductor ($|f\rangle$) are diabatically separated and can be expressed in terms of localized basis functions, i.e. a linear combination of atomic orbitals:

$$|i\rangle = \sum_m c_m \chi_m \tag{2.75}$$

$$|f\rangle = \sum_k C_{fk} \phi_k \tag{2.76}$$

where $\{\chi_m\}$ is the basis set for the molecule and $\{\phi_k\}$ is the basis set for the semiconductor. The indices m (or n) and k (or k') refer to the molecule's and the semiconductor's basis functions, respectively. We hence define the semiconductor's energy-dependent density matrix:

$$\rho_{kk'}(E) = \sum_f C_{fk} C^*_{fk'}\, \delta(E - E_f) \tag{2.77}$$

where E_f are the energies of the one-electron states of the semiconductor. We further define the matrix elements V_{mk} as the electronic coupling between localized atomic orbitals on the semiconductor and on the dye. Following these definitions, the rate of electron injection Γ (for orthogonal basis sets, such as those mostly used in this thesis) can be expressed as:

$$\hbar\Gamma = 2\pi \sum_{mn} c_m c_n^* \sum_{kk'} V_{mk} V^*_{nk'} \rho_{kk'}(E_i) \tag{2.78}$$

This expression can be adapted to fit also non-orthogonal basis sets, as follows[128]:

$$\hbar\Gamma = 2\pi \sum_{m,n} c_m\, c_n^* \sum_{k,k'} (ES_{mk} - V_{mk})(ES_{nk'} - V_{nk'}) \rho_{kk'}(E_i) \tag{2.79}$$

where S_{mk} and $S_{nk'}$ are the overlap matrix elements.

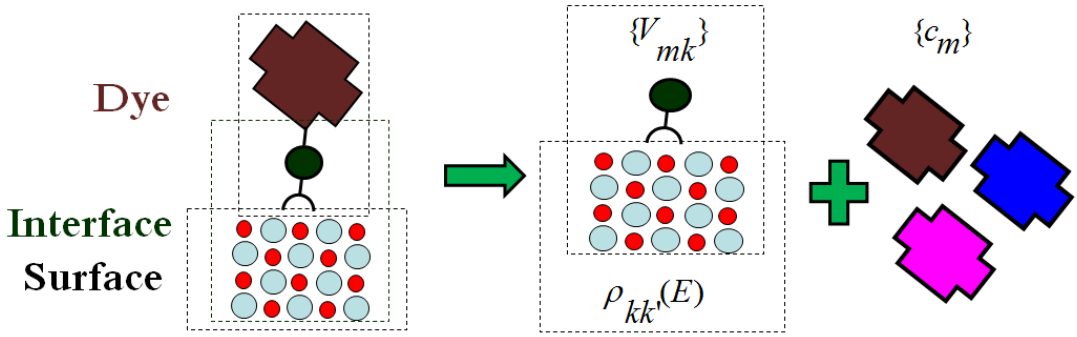

Figure 2.2: schematization of the matrix partitioning scheme for dye-semiconductor system; quantities appearing in Eq. 2.78 are computed in separated calculations, allowing high through put analysis.

Eq. 2.78 includes quantities that can be obtained from different DFT calculations, hence providing a practical outcome from the matrix partitioning scheme (see **Figure 2.2**). Because of the localized nature of atomic orbitals, the coupling terms V_{mk} (given by an off-diagonal Kohn-Sham matrix element) between the semiconductor's and molecule's localized basis functions are significantly different from zero only for those m and k that are at or near the semiconductor-dye interface. Hence, we can use the matrix elements only for k, k' close to the semiconductor surface. In our model, therefore, we represent a semiconductor surface with a slab, which is periodically repeated in two dimensions and has a finite depth, a widely used approach for modeling surfaces. [148, 162, 163] Then, to obtain V_{mk} values, instead of performing a calculation of an entire adsorbed dye, which is very computationally demanding and would be not feasible in screening a large number of potential chromophores, we can consider only the interface of the semiconductor slab with the chromophore's anchoring group. In fact, since we expect V_{mk} values to be large only in the interface region, V_{mk} values for m not belonging to the anchoring group are going to be negligible and can be considered to be zero. Of course, different chemical composition and attachment chemistries of the

anchoring group on the semiconductor surface will produce different V_{mk} matrix elements, thus influencing the computed injection times.

2.3.4 Why matrix partitioning scheme? A comparison with recent theoretical works

In this section, we remark the reasons behind our study of electron injection in DSSCs, comparing our method with recent theoretical approaches to this problem. Hence, we motivate our choice, analyzing advantages and drawbacks of the current methodologies, and explaining the novelty of the contribution we provide to this field.

(i) Prezhdo and coworkers have used intensively non adiabatic molecular dynamics (NAMD), within DFT and TD-DFT calculations, to study the electron transfer dynamics for few dyes (mainly bipyridine ligands and alizarin)[114, 115, 120-122].

In their NAMD approach, for a given set of nuclear coordinates, DFT calculations provide a set of Born-Oppenheimer states $\{\phi_i\}$, which are used to compute the wavefunction of the excited state:

$$\Psi = \sum_i c_i \, \phi_i \tag{2.80}$$

The time dependent evolution of the excited state is hence expressed for each time step Δt as follows:

$$\Psi(t + \Delta t) = \Psi(t - \Delta t) - \frac{2\mathrm{i}}{\hbar} \Delta t \widehat{H} \Psi(t) \tag{2.81}$$

Non adiabatic couplings between Born-Oppenheimer states are computed from overlap of the orbitals at subsequent time steps:

$$V_{ij}^{NA} \cong \left(\frac{1}{2\Delta t}\right)(\langle \phi_i(t)||\phi_j(t+\Delta t)\rangle - \langle \phi_i(t+\Delta t)||\phi_j(t)\rangle) \quad (2.82)$$

In order to probe the electron injection from a dye to a semiconductor surface, the time dependent electron density on the dye is monitored against the time, at each time step:

$$\rho_{dye}(t) = \sum_i |c_i(t)|^2 \int_{dye} |\phi_i(t)|^2 \quad (2.83)$$

$$\frac{d\rho_{dye}(t)}{dt} = \sum_i \frac{|c_i(t)|^2}{dt} \int_{dye} |\phi_i(t)|^2 + \sum_i |c_i(t)|^2 + \frac{d\int_{dye} |\phi_i(t)|^2}{dt} \quad (2.84)$$

Eq.2.84 shows clearly that the rate is given by two contributions: (i) a non adiabatic one, which is conveyed by the time dependence of the expansion coefficients $c_i(t)$, determining the change in occupation of ϕ_i; (ii) and adiabatic contribution represented by $\frac{d\int_{dye} |\phi_i(t)|^2}{dt}$, hence the time dependent evolution within the adiabatic states ϕ_i.

More recently, Prezhdo and coworkers employed a similar methodology to study the dynamics of SF in a model donor-acceptor system, with a particular focus on the competition between SF and exciton dissociation. In this case, however, DFT is not sufficient to describe the electronic structure of the system and the Kohn-Sham orbitals are corrected, using the results obtained by more sophisticated *ab initio* calculations.[27]

NAMD represents a powerful tool for the study of different pathways in electron transfer processes. Nevertheless, the large computational cost of this method makes it not suitable for the theoretical analysis of a large number of candidate dyes and the calculations are limited only to small model systems. In principle, each dye would need

an expansive simulation of the interface and, even if a large number of simulations could be performed, the obtained results would not be useful to isolate the individual factors (i.e. structure of the dye, chemical nature of the anchoring group) affecting the injection rates. This is true also for SF, as DFT and TD-DFT calculations cannot provide a description of double excited states, such as the ME states. Parameters entering the simulations must be fitted to other post-HF calculations, thus enhancing the computational cost of the whole procedure.

(ii) May and coworkers developed a semi-empirical model to study electron injection for a variety of dye-semiconductor systems (mainly perylene-TiO_2 interface)[125, 126].Their work share with our approach a similar diabatization of molecular (ground and excited states of the molecule, labeled as g and e) and semiconductor states (k)[125]:

$$H = \sum_{a=g,e,\mathbf{k}} H_a(Q)\,|\varphi_a\rangle\langle\varphi_a| + \sum_k (V_{ke}(Q)|\varphi_k\rangle\langle\varphi_e| + h.c.) \tag{2.85}$$

H_a is a vibronic Hamiltonian including explicitly vibrational degrees of freedom within the harmonic oscillator model. This is related to the empirical part of the method, because the parameters entering Eq. 2.85 are optimized against experimental absorption spectra. Once optimal parameters have been obtained, the rates are computed with an expression which does not depend on vibrations and is very similar to the one used in this thesis:

$$2\Gamma = \frac{2\pi}{\hbar^2}\bar{\rho}|\bar{V}|^2 \tag{2.86}$$

Where $\bar{\rho}$ and $\bar{V}$ are average values of the acceptor's density of states and of electronic coupling, respectively.

The major difference with our approach is given by its semi-empirical nature, represented by the fact that parameters entering the Hamiltonian of Eq. 2.85 are fitted, in order to mimic experimental absorption spectra. For this reason, this method cannot be considered a "stand-alone" procedure, capable of predicting the injection properties of a dye, without the aid of experiments. In fact, a candidate dye has to be, in any case, synthesized and has to undergo to a series of experiments. This is not convenient if one desires to rapidly screen a large number of candidate dyes.

(iii) Thoss and coworkers also expressed the Hamiltonian in terms of diabatic states[119]:

$$H_S = T + |\varphi_d\rangle V_{dd} \langle\varphi_d| + \sum_k |\varphi_k\rangle V_{dd} \langle\varphi_k| + \sum_k (|\varphi_d\rangle V_{dk} \langle\varphi_k| + |\varphi_k\rangle V_{kd} \langle\varphi_d|) \quad (2.87)$$

where again $|\varphi_d\rangle$ represents the donor state localized on the chromophore, and $|\varphi_k\rangle$ the acceptor states localized on the semiconductor. T is a kinetic energy term including nuclear degrees of freedom. Parameters entering this Hamiltonian have been computed from a tight-binding model in ref.[118] and from *ab initio* calculations, with a matrix partitioning scheme (as in this thesis) in ref.[113, 119]. In their work, however, the effect of the solvent is included as a bath of harmonic oscillators, which are coupled with the dye semi-conductor system:

$$H_B = \frac{1}{2} \sum_j (p_j^2 + \omega_j^2 x_j^2) \quad (2.88)$$

$$H_{SB} = |\varphi_d\rangle \sum_j (c_j^d \, x_j)\langle\varphi_d| + \sum_k |\varphi_k\rangle \sum_j (c_j^k \, x_j)\langle\varphi_d| \tag{2.89}$$

where H_B is the Hamiltonian of the bath and H_{SB} contains couplings of the bath with dye's and semiconductor's states, respectively. Once the Hamiltonian has been defined ($H = H_S + H_B + H_{SB}$), the electronic structure of a dye-semiconductor cluster is studied with DFT and, finally, the quantum dynamics of the system is studied with the multi-layer (ML) multi-configurational time-dependent Hartree method (MCTDH).[117] This is a multi-reference method, where, instead of expressing the wavefunction as a linear combination of time-independent states, it is given by a linear combination of time-dependent configurations:

$$|\Psi(t)\rangle = \sum_j A_j(t)\psi_j(t) \tag{2.90}$$

In a single layer (1L) MCTDH, $\{\psi_j(t)\}$ set is given by CI expansion of the time-dependent basis functions. In a ML approach, the wavefunction is obtained by a recursive procedure, where also $\{\psi_j(t)\}$ are expressed as a time-dependent expansions (2L-MCTDH). Extension to a larger number of layers is conceptually simple but the computational cost is increased. This method has been used to study the coumarin343-TiO_2 and the alizarin-TiO_2 systems, providing results in good agreement with experimental evidences.[113, 118, 119] Nevertheless, while sharing general aspects with our approach, this method features calculations of the whole dye-semiconductor interface and requires computational demanding quantum dynamics simulations, thus preventing its use for high through-put analysis.

In summary, our approach to the study of electron injection in DSSC, presented in Section 2.3.3, shows some clear advantages if compared with previous works: (i) it does not require computational demanding quantum dynamics simulations; (ii) it does not require *ab initio* calculations of the electronic structure of the whole dye-semiconductor's surface; (iii) it is a completely *ab initio* procedure: no physical parameter needs to be adjusted to fit experiments. For this reason, our methodology, instead of previous works, allows to rapidly predict electron injection rates: i.e. families of dyes sharing the same anchoring group can be rapidly screened, since only a single calculation of the anchoring-group + slab system is needed to compute V_{mk} and $\rho_{kk'}(E)$ for all of them. $\{c_m\}$ can be computed from simple calculations of isolated molecules, thus enabling to screen a large number of dyes at a reduced computational cost. Moreover, within the partitioning scheme, we are able to disentangle different effects, influencing the electron injection rates, which is not possible even for the most accurate simulation of the entire system.

In this thesis, we use this approach to study three different problems. In Chapter 3, we perform an analysis of electron injection for 16 different organic dyes, sharing the same anchoring group (a phosphonated moiety), and compare the results with available experiments, in order to test the model and investigate the possible use of phosphonic acid as an alternative to common carboxylated dyes. In Chapter 4, we apply this method differently, analyzing the effect of the anchoring group on electron injection; electron injection rates are computed for organic dyes sharing the same structure (a perylene) but possessing different anchoring groups. This is done in conjunction with a study of the attachment chemistry of each considered moiety, in order to screen anchoring groups that bind strongly to TiO_2 surface and have a positive effect on the injection properties

of a dye, at the same time. Finally, in Chapter 5 we verify the applicability of the partitioning scheme for metal-organic dyes, which have a complex attachment chemistry on the semiconductor surface, studying the adsorption modes and the electron injection properties of the N3 dye on rutile (110).

Chapter 3:

Theoretical study of phosphonated dyes for dye-sensitized solar cells

Abstract

The attachment chemistry of the chromophore onto the semiconductor surface influences the efficiency of electron injection in dye-sensitized solar cells (DSSCs). In this chapter, we study injection times for dyes that bind to the semiconductor surface via the phosphonic acid anchoring group and the effect on the injection time of different binding modes (molecular or dissociative, monodentate or bidentate) of phosphonic acid for both TiO_2 rutile (110) and anatase (101) surfaces. We calculate electron injection times for a large set of organic dyes on TiO_2 rutile (110) and anatase (101) surfaces for the most stable adsorption geometries of the phosphonic acid anchoring group, using a model based on partitioning the semiconductor-chromophore system into fragments. We analyze the influence of the size and nature of the anchoring group on the injection times, performing calculations with larger models of the anchoring group (e.g. phenyl-phosphonic acid). Through the partitioning procedure we are able to separate the effect of the binding geometry from other effects influencing the efficiency of the electron injection. The results show that dissociative bidentate adsorption modes generally lead to faster injection, compared to monodentate and molecular ones. Our results are in good agreement with experiments (where available), showing that our model is capable of predicting the effects of the anchoring groups and of different spacer groups on the

injection times, and is, therefore, suitable for designing new and more efficient chromophores.

3.1 Introduction

In this chapter we employ the matrix partitioning scheme, discussed in Chapter 2, in order to study the injection characteristics of dyes that bind to the semiconductor surface with a phosphonate moiety and to analyze the effects of the attachment chemistry on injection rates. In fact, the binding configuration of the anchoring group on TiO_2 surface is fundamental, since it is responsible for both the stable adsorption of the dye and for the coupling of the anchoring group with TiO_2. Moreover phosphonated dyes are very interesting for DSSC devices; in fact, theoretical studies of phosphonic acid show that it binds more strongly than formic acid to TiO_2 surfaces.[164, 165] Therefore, the use of phosphonated dyes can improve the long-term stability of the device. However, there are few experimental and theoretical studies of the electron injection characteristics of phosphonated dyes. Experimental studies of perylene derivatives on TiO_2 suggest that electron injection from phosphonated dyes is somewhat slower than from their carboxylated analogues.[88, 91, 92, 98, 166, 167] This result is supported by theoretical studies of the same molecules, using the full width at half maximum (FWHM) of the dye's LUMO state as a measure of injection time[168] and using model Hamiltonian calculations.[165] However, there is no definite agreement between the theoretical predictions made using different computational approaches. For example, for pyridine-4-phosphonic acid, calculated injection times range from 10 fs (using parameterized Hamiltonian[168]) to 460 fs (using a semi-empirical Hückel

Hamiltonian combined with molecular dynamics[169]). Moreover, theoretical modeling suggests that injection times strongly depend on the adsorption mode (e.g., 60 fs injection time for the bidentate mode, and 460 fs for the monodentate adsorption of the above molecule).[169] Therefore, at present, there is no systematic study of phosphonated dyes and, among these few studies, there is a significant discrepancy between different methods and with experimental results too. Moreover, the attachment chemistry of phosphonic acid on TiO_2 and the effects of the different binding modes on the injection characteristics have not been considered yet. This is an important aspect, because the theoretical description of the electronic structure at the interface and, consequently, of the charge transfer need an accurate description of the adsorption geometry of the dye.

Several theoretical studies addressed the adsorption geometry of phosphonic or methylphosphonic acid on rutile (110) and anatase (101), using DFT[164, 165, 170] and density-functional tight-binding (DFTB).[171] A large number of possible configurations have been identified: four on rutile (110) and eight on anatase (101). Thus, phosphonic acid has a much richer adsorption chemistry on TiO_2 than seen for carboxylic acids, which have one stable adsorption configuration on rutile (110) (dissociated bidentate)[148, 162, 172] and two configurations on anatase (101) (molecular monodentate adsorption and dissociative bridging-bidentate).[148, 163] For phosphonic acid, the bidentate configurations were identified as the most stable ones on rutile (110), particularly the fully dissociative one with two protons adsorbed on the semiconductor surface.[165, 171] On anatase (101) slabs, DFT-B3LYP calculations favoured the monodentate configuration[164], while DFTB studies favoured the bidentate configuration with two protons adsorbed on the surface[171], even if the

differences between the best monodentate and bidentate structures in both of these studies were no more than 0.2 eV (of the order of the accuracy of DFT calculations, and smaller than the accuracy of DFTB calculations). These results suggest that different adsorption modes are likely to co-exist, and an accurate theoretical prediction of the injection times of phosphonated dyes must take into account and analyze the effects of the different adsorption modes.

3.2 Computational strategy

3.2.1 Model of electron injection

Injection times are computed adopting the methodology reported in detail in Chapter 2 where the injection rate Γ is computed through the following expression:

$$\hbar\Gamma = 2\pi \sum_{mn} c_m c_n^* \sum_{kk'} V_{mk} V_{nk'}^* \rho_{kk'}(E_i) \tag{3.1}$$

where $\{c_m\}$ is the set of coefficients of the dye LUMO, $\{V_{mk}\}$ are the coupling coefficients between dye and TiO_2, $\{\rho_{kk'}\}$ is the density of states of TiO_2, E_i is the dye LUMO energy (hence, the injection energy). $\{c_m\}$ and E_i are computed from a calculation of the dye alone, $\{\rho_{kk'}\}$ and $\{V_{mk}\}$ are computed from a calculation of a TiO_2 slab with the anchoring group of the dye attached on its surface. In fact, as explained in Chapter 2, because of the localized nature of atomic orbitals, the coupling terms V_{mk} between the semiconductor's and molecule's localized basis functions are significantly different from zero at or near the semiconductor-dye interface and, for the same reason, we can use the $\rho_{kk'}(E)$ matrix elements only for k, k' close to the semiconductor surface.

3.2.2 Electronic structure calculations

In our model, we represent a semiconductor surface with a slab, which is periodically repeated in two dimensions and has a finite depth. Then, to obtain V_{mk} values, instead of performing a calculation of an entire adsorbed dye, which is very computationally demanding and would be not feasible in screening a large number of potential chromophores, we can consider only the interface of the semiconductor slab with the chromophore's anchoring group. In fact, since we expect V_{mk} values to be large only in the interface region, V_{mk} values for m not belonging to the anchoring group are going to be negligible and can be considered to be zero.

We modeled the TiO_2+anchoring group system, as well as the isolated dye molecules, using DFT calculations. We used the CRYSTAL09 code.[173] CRYSTAL09 computations employed an explicit all-electron representation of TiO_2 with triple valence plus polarization Gaussian basis sets first used in ref.[174] for Ti and O, and a double valence plus polarization Gaussian basis set first used in ref.[175] for P. These basis sets are available on CRYSTAL website.[243] We employed the B3LYP functional[147] which was proven to give a reasonable description of the TiO_2 electronic structure.[148, 177] The **k**-points sampled were chosen using a Monkhorst-Pack net using a 2 × 2 × 1 **k**-points grid for slabs with adsorbates. The convergence criteria used for geometry optimization were: energy tolerance 10^{-4} Ha, root-mean-square (RMS) of the gradient 10^{-3} Ha/Bohr, RMS of the displacement 0.0012 Bohr. Rutile (110) and anatase (101) surfaces were both modeled using two-layer slabs with the 2×2 cell area (**Figure 1a,b**). The modeling of molecular adsorption was obtained using constrained slabs with the adsorbate placed at one side of the slab, and the bottom layer atoms fixed at their respective bulk geometry. This scheme is used in the majority

of simulations of surfaces, including TiO_2.[148, 162, 163] Similar computational setup (CRYSTAL09 calculations using B3LYP functional and the same convergence criteria as above) was used to model isolated dye molecules, but in this case the simulated system was non-periodic, and a single **k**-point (**Γ**-point) was used. Double valence plus polarization Gaussian basis sets, available on the CRYSTAL website[243], were used for C, N and P, and a triple valence plus polarization Gaussian basis set for O.

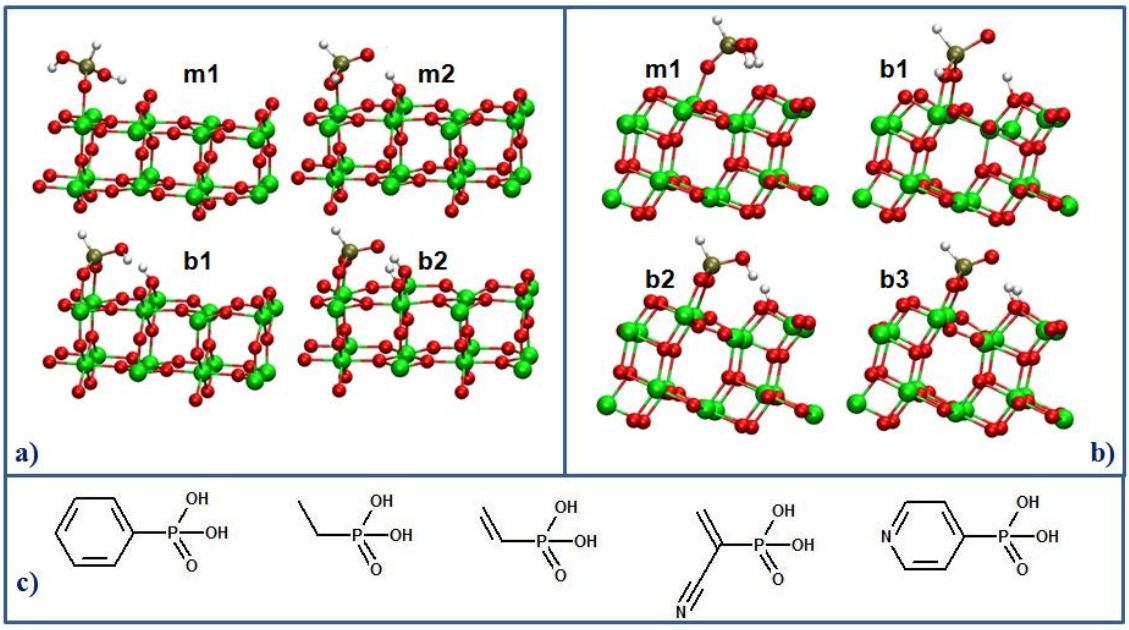

Figure 3.1: Optimized structures (a) of the 2-layer rutile (110) slab with phosphonic acid, and (b) of the 2-layer anatase (101) slab with phosphonic acid systems with different adsorption modes. Ti atoms are in green, O in red, P in brown and H in white (see text for the description of the adsorption modes). (c) Structures of the studied larger binding groups.

3.2.3 Surface-adsorbate systems

In the majority of the calculations discussed below, phosphonic acid on TiO_2 was used to represent the TiO_2-anchoring group interface. There are several alternative adsorption modes for such anchoring groups as carboxylic and phosphonic acid, *e.g.* molecular, bridging or chelating. A large number of adsorption modes were reported for phosphonic (and alkylphosphonic) acids on TiO_2: up to four on rutile (110)[165, 170,

171] and eight on anatase (101)[164, 171], including both bidentate and monodentate modes, with and without the acidic proton transferred to the surface. As a starting point for modeling the different adsorption modes of phosphonic acid (and phosphonic acid functionalized with organic groups), we choose the structures studied in the work of Luschtinetz and coworkers, who computed four adsorption geometries for rutile (110) and eight for anatase (101).[171] For consistency, and to verify that the predicted structures are not modified by a different computational method, we re-optimize Luschtinetz's structures.

In **Figure 3.1a** and **Figure 3.1b** we show the optimized structures for the adsorption of phosphonic acid on the rutile (110) and the anatase (101) surfaces. For rutile, the m1 and m2 structures feature a monodentate adsorption mode, molecular and dissociative with a proton transferred to a surface O, respectively. The latter, according to previous theoretical work[171], is more stable than the former by ≈9 kcal/mol. The b1 and b2 structures show a bidentate adsorption mode with one and two adsorbed protons, respectively, and they are the most stable adsorption modes, a result which is confirmed by a recent study of adsorption of methyl phosphonate on rutile (110).[170] The b2 structure is the most stable adsorption configuration, due to the adsorption of both protons on the slab surface (≈5 kcal/mol more than the b1 structure). Our results agree to this picture of the system, with the m2 mode being the most stable monodentate (≈10 kcal/mol more than m1) and with the b2 mode being the most stable adsorption mode (≈20 kcal/mol more than the b1 structure) overall.

For anatase (101), although previous studies considered eight adsorption configurations[164, 171], we choose to study only the four most stable ones. We have a monodentate molecular adsorption mode (m1) and three bidentate modes, two of them

with a single proton adsorbed on the surface (b1 and b2) and one with both protons adsorbed on the slab (b3). Luschtinetz and co-workers, using DFTB, found that bidentate modes, in particular the b3 adsorption mode, represent the most stable binding geometry (the difference with the least stable considered bidentate mode is ≈5 kcal/mol while the difference with the most stable monodentate mode is around ≈20 kcal/mol)[171], while an earlier work by Nilsing and coworkers, using DFT-B3LYP, suggests that the m1 structure has the strongest adsorption (relative adsorption energies are contained in a small range ≈7 kcal/mol for all the studied configurations).[164] Nevertheless, these earlier studies agree that the difference in stability of the various adsorption modes is small. In our study, the most stable adsorption mode is the b3; the difference between b3 and the least stable considered bidentate (b1) is 12 kcal/mol and the difference with the most stable monodentate is 16 kcal/mol. Our structures are in good agreement with previous works, and the P-H bond, in all these configurations, is pointing upwards, compatible with possible adsorption geometries of a complete chromophore on the slab.

Additionally, we performed several calculations using larger anchoring group models: instead of just the phosphonic acid group, we considered larger fragments of the dyes (i.e. phosphonic acid with various linker groups, shown in **Figure 1c**), adsorbed on the rutile (110) surface. For these substituted phosphonic acids, we used the same adsorption modes (m1, m2, b1 and b2) as for the phosphonic acid on rutile (110). These calculations were done in order to check if the size of the anchoring fragment, used in the TiO_2-anchoring group interface model, affects the accuracy of the calculated injection times.

3.3 Results and Discussion

We chose a set of dye molecules featuring phosphonic acid as a binding group (**Figure 3.2**). Among them, there are some perylene derivatives whose charge injection on rutile and anatase surfaces has been studied experimentally (P1-P3)[91, 92] but we also model some new perylene derivatives (P4-P7), in order to explore the effect of simple modifications of the spacer group chemistry, near the phosphonic acid anchoring group. We have also considered a set of dyes (D1-D9 in **Figure 3.2**), similar to those studied in an earlier work[129] but with carboxylic group replaced by phosphonic group, to evaluate the difference between these two anchoring groups.

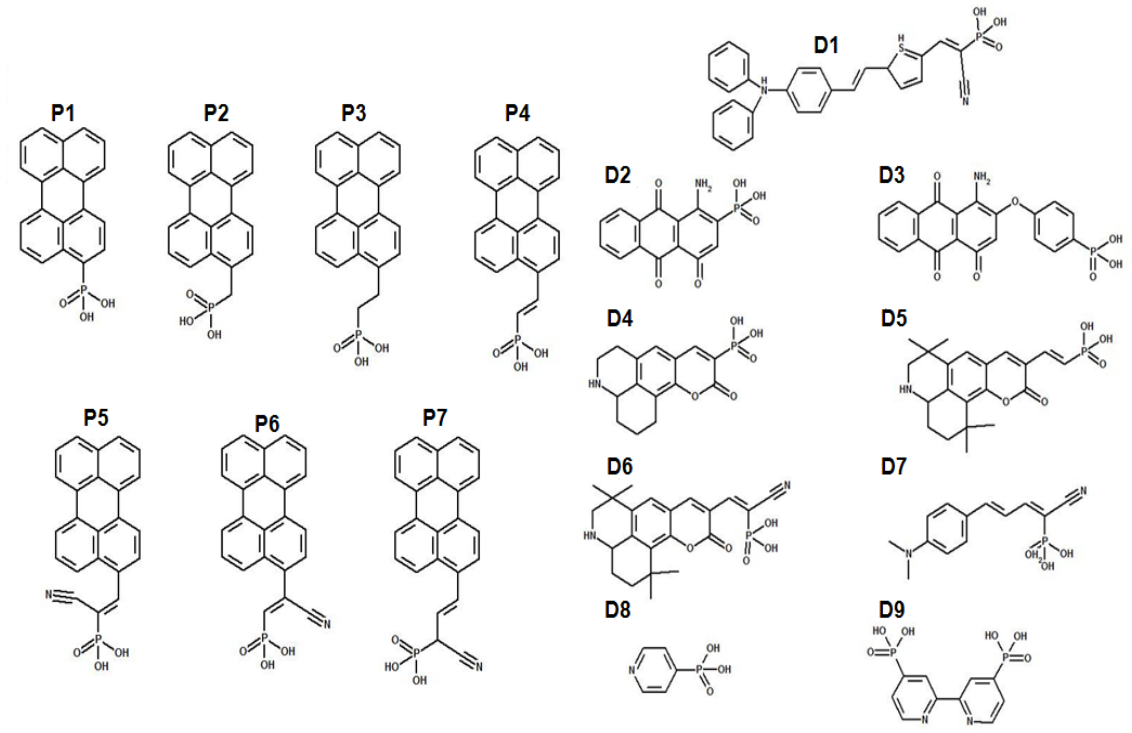

Figure 3.2: Structures of the studied perylene derivatives (P1-P7) and of the other chromophores (D1-D9).

In **Table 3.1** we collect the injection times for the P1-P7 dyes on rutile (110) and anatase (101), respectively. First, we compare the obtained results with the known experimental values for the P1 and P2 dyes on rutile (110) and on anatase (101). For the P1 dye on rutile (110) we compute the injection times of 2.6 fs and 2.9 fs for the most stable adsorption modes (b1 and b2), somewhat faster than the experimental value of 23.5 fs, while for P2 we obtain 40.2 fs and 73.2 fs, similar to the experimental result (35.9 fs). Injection times for the less stable adsorption modes m1 and m2 are slower than for b1 and b2. For the P1 dye on anatase (101) the computed injection times are smaller than the experimental value (28 fs) for the all the adsorption modes (between 0.44 and 2.9 fs), while for P2 dye the computed injection times are also somewhat smaller for the bidentate adsorption modes but slightly larger than the experimental time for the monodentate adsorption modes. The agreement between the calculated and experimental values is reasonably good (within an order of magnitude – which is acceptable considering that experimental estimates of injection times are often the upper limits of injection times, limited by the instrument resolution, which ranges from few femtoseconds[98] to as high as 100 fs[89], depending on the technique used).

We observe that injection is faster for the most stable adsorption modes (the bidentate ones) and that there is no remarkable difference between the injection times calculated for rutile (110) and anatase (101). Nevertheless, we can pinpoint that the anatase b3 adsorption mode features the fastest injection for all the dyes. We observe that the effect of the different attachment modes on the injection time is more evident for slower dyes, while for the fast dye P1 the difference between the adsorption modes is less pronounced. Unfortunately, there are experimental data only for few perylene-phosphonic dyes, but this theoretical study of their electron injection properties is

useful, because it allows us to analyze systematically the efficiency of different dyes, e.g. with different spacer groups. For example, we observe similar results for the P2 and P3 dyes (which feature a CH_2 and a CH_2CH_2 spacer groups, respectively) with slower injection than the simple P1 dye, due to the presence of *sp3* carbon atoms separating the aromatic part of the dyes from the anchoring group. On the other hand, the injection is remarkably fast for the P4 dye, which contains the CH=CH spacer group, an effect that has already been observed for carboxylic acid-binding dyes.[92, 129]

Table 3.1: Calculated and experimental (where available) injection times (fs) of the P1-P7 dyes on rutile (110) for their m1, m2, b1 and b2 adsorption modes and on anatase (101) for their m1, b1, b2 and b3 adsorption modes, respectively.

Dye on Rutile	**t_{m1} (fs)**	**t_{m2} (fs)**	**t_{b1} (fs)**	**t_{b2} (fs)**	**t_{exp} (fs)[91]**
P1	14.8	7.6	2.6	2.9	23.5
P2	150.3	117.9	40.2	73.2	35.9
P3	42.8	67.9	28.0	33.4	
P4	27.8	33.1	8.3	4.9	
P5	22.6	10.2	2.8	3.3	
P6	3.4	2.8	1.55	1.5	
P7	136.2	213.9	44.0	14.2	
Dye on Anatase	**t_{m1} (fs)**	**t_{b1} (fs)**	**t_{b2} (fs)**	**t_{b3} (fs)**	**t_{exp} (fs)[92]**
P1	2.9	1.6	2.4	0.44	28
P2	176.0	123.4	41.5	9.6	63
P3	177.8	18.0	27.3	2.1	
P4	35.8	1.5	4.5	0.32	
P5	63.4	6.1	1.7	0.87	
P6	2.3	2.9	0.4	0.13	
P7	15.1	90.0	9.5	19.4	

In the P5 and P6 dyes we study the effect of the CN moiety on the injection times, placing this group in two different positions. In P5, we place it on the same *sp2* carbon

linked to the $PO(OH)_2$ moiety (a motif used in many carboxyl-containing dyes).[178] In the P6 dye, we investigate an alternative position of the cyano group on the next *sp2* carbon atom, in the β position to the phosphonate group, which has not been considered so far for DSSC dyes, to the best of our knowledge. The results for the two chromophores are similar, featuring a very fast injection due to the presence of the CN moiety, which is a strong electron withdrawing group. This agrees with experiments reporting that dyes with the CH=CH moiety connected to the cyano group lead to an increased efficiency in the DSSC device.[178] It is worth noting that injection from the P6 dye (with the new position of the cyano group) is slightly faster than P5, suggesting that this novel attachment chemistry may be used to realize more efficient charge injection in DSSC dyes.

Finally, we study the P7 dye that we conceived in order to analyze the effect of the different groups at the same time: it contains the vinyl group, an *sp3* carbon and a CN moiety attached to it. The results show an injection which is faster than for P2 and P3 dyes but slightly slower than the other dyes, as we could expect knowing the effect of the different groups: the CN group in P7 ensures faster injection than for P2 and P3, but the presence of the *sp3* carbon slows injection compared to the dyes P1, P4-P6 with all unsaturated carbons. These results suggest that, to some extent, the effect of these structural modifications is additive.

To validate one of the approximations used in this chapter, we investigate how the calculated injection time is affected by the size of the anchoring fragment in the TiO_2-anchoring group interface model, including various linker groups in the anchoring group (see **Figure 3.1a** and **Table 3.2**).

For example, for the P3 dye we calculate injection times, employing phosphonate or ethyl-phosphonate adsorbed on TiO_2 as models for the TiO_2-anchoring group interface, and we obtain results in very good agreement with each other. For the D6 dye we consider two alternative models of the interface, with anchoring groups containing the CH_2=CH and the CH_2=C(CN) moiety. The effect of the introduction of the double bond and of the cyano group in the anchoring group model does not affect the result significantly.

Table 3.2: Comparison of the injection times (fs) for P3, D6 and D8 dyes on rutile (110), calculated with different models of the anchoring group.

Dye	Anchor group	t_{m1} (fs)	t_{m2} (fs)	t_{b1} (fs)	t_{b2} (fs)
P3	$HPO(OH)_2$	42.8	67.9	28.0	33.4
	CH_3-CH_2-$PO(OH)_2$	24.5	64.2	34.3	21.0
D6	$HPO(OH)_2$	6.3	3.2	1.8	2.3
	CH_2=CH-$PO(OH)_2$	5.5	3.5	2.3	1.3
	CH_2=C(CN)-$PO(OH)_2$	6.5	2.3	1.8	1.6
D8	$HPO(OH)_2$	7.3	1.5	0.54	0.76
	Ph-$PO(OH)_2$	1.03	0.92	1.3	0.73
	Py-$PO(OH)_2$	3.6	0.93	1.1	0.46

Finally, we study the injection of D8, considering phenyl (Ph)-phosphonate and pyridyl (Py)-phosphonate as anchoring groups in the interface model (in this case the latter represents also the complete dye), and the results are definitely very similar, in particular for the two different aromatic groups. This proves that the coupling terms

between the dye's and semiconductor's orbitals are significant only immediately at the binding interface, and even a small model anchoring group, such as phosphonic acid, is sufficient to describe the interface, making the full dye-surface calculation not necessary in most cases.

Table 3.3: Injection times (fs) of the P1-P7 and D1-D9 dyes on rutile (110) for the m1, m2, b1 and b2 adsorption geometries, respectively, and injection times of the same dyes featuring carboxylic acid as binding group calculated in this chapter and from literature[129]. Ratios between injection times for carboxylated and phophonated dyes (for the former we consider our values for the P1-P7 dyes and Ref.[129] values for D1-D9 dyes; for the latter we consider the injection times belonging to the most stable adsorption mode b2).

Dye	**t_{m1} (fs)**	**t_{m2} (fs)**	**T_{b1} (fs)**	**t_{b2} (fs)**	**t_{COOH} (fs)**	**t_{COOH}(fs) ref.[129]**	**t_{b2}/t_{COOH} ratio**
P1	14.8	7.6	2.6	2.9	6.5	5.3	0.44
P2	150.3	117.9	40.2	73.2	269.5		0.27
P3	42.8	67.9	28.0	33.4	109.9	282	0.30
P4	27.8	33.1	8.3	4.9	11.7	6.0	0.42
P5	22.6	10.2	2.8	3.3	10.8		0.31
P6	3.4	2.8	1.55	1.5	3.4		0.44
P7	136.2	213.9	44.0	14.2	30.7		0.46
D1	19.8	5.1	3.1	3.9		17.2	0.23
D2	4.1	1.8	9.00	6.9		33.0	0.21
D3	210.2	126.0	81.9	71.8		157	0.46
D4	30.2	11.3	5.4	13.1		10.0	1.31
D5	14.5	13.7	12.4	29.8		11.6	2.57
D6	6.3	3.2	1.8	2.3		4.8	0.48
D7	5.1	4.0	2.9	1.4		5.6	0.25
D8	7.3	1.5	0.54	0.76		0.73	1.0
D9	4.5	3.2	0.51	1.0		0.68	1.47

In **Table 3.3** we show the injection times calculated for the P1-P7 dyes and D1-D9 dyes on rutile (110) and compare them with the results for their carboxylated analogues. Injection times for similar dyes containing a carboxylic acid, instead of a phosphonic acid group, were recently studied (molecular monodentate and dissociative bidentate adsorption modes for anatase (101), dissociative bidentate for rutile (110); DFT-PBE level of theory[129]). Here we compare injection times for carboxylic and phosphonic groups. First, we compare the earlier results for carboxylic-containing molecules (adsorbed on rutile (110) in the bridging-bidentate configuration)[129], computed using the PBE functional[179] within the SIESTA code[176], with our new results computed using CRYSTAL09 and the B3LYP functional. **Table 3.3** (columns 6-7 for P1-P7 dyes) clearly shows that the results obtained in this work are consistent with the PBE calculations, where the largest discrepancy arises for the P3 dye, and are in slightly better agreement with experimental values (which are 9 fs for P1, 47 fs for P3, 13.5 fs for P4).[91] This shows that the choice of the exchange-correlation functional (pure DFT, e.g. PBE, or hybrid, e.g. B3LYP), does not strongly influence the alignment of the dyes' and semiconductor's electronic energy levels and the resulting electron injection times. We can also compare the injection times calculated for dyes featuring the two different binding groups. While we can clearly state that b2 mode for phosphonated dyes gives a faster injection, compared to the carboxylated analogues for most of the considered dyes, the results for the two anchoring groups are similar and the general trend is comparable. We point out that, since the difference in stability of the different adsorption modes of phosphonic acid is small[164, 165, 171], in the real system several adsorption modes are likely to co-exist, and the average injection times for

phosphonated dyes are likely to be longer than the results for the b2 mode (by no more than an order of magnitude, according to the data in **Table 3.3**) and closer to an average value among the several most stable configurations. In summary, we show that our model gives reliable estimates of injection times and can be used to predict injection properties of new dyes. Our results suggest that the phosphonic acid anchoring group is as good as the carboxylic acid group in DSSC dyes, because its adsorption is stronger, while injection times are similar.

3.4 Conclusions

In this chapter we discussed the results obtained from a systematic analysis of the electron injection characteristics for a large set of phosphonated dyes on TiO_2. We modelled the TiO_2-anchoring group system adopting phosphonic acid as anchoring group, and we studied the most stable adsorption modes on both rutile (110) and anatase (101) surfaces. We then computed the injection times for a large set of phosphonated dyes, for all considered adsorption modes, observing the fastest rates for bidendate dissociative modes. However, different adsorption modes are likely to coexist, due to the small difference in adsorption energies, thus lowering the effective rate. Our study of the size of the anchoring group showed that a very simple model, featuring only the phosphonic acid attached to the surface, is sufficient to simulate the TiO_2-dye interface, thus granting a very low computational cost to our method, if compared to the study of the full dye at the interface. Our results are in good agreement with the available experimental results and our model is capable of predicting the effects of different spacer groups on the injection times, thus being suitable for designing new and more

efficient chromophores. In this way we can assist experimental studies, providing a reliable qualitative and quantitative prediction of the injection characteristics of a dye, before it has been synthesized. A natural extension of our method, therefore, includes calculations of injection times for other less common binding groups for organic dyes and the extension of the study to metal-organic dyes, topics that will be covered in the following chapters. In fact, a fundamental advantage of our method is the capability of isolating the effect of the anchoring group from other effects and its low computational cost (compared to other methods that could be more accurate for a single calculation), that paves the way to high trough-put studies.

Chapter 4:

Systematic study of several anchoring groups for dye sensitized solar cells dyes

Abstract

The choice of the anchoring group of the dye in a DSSC device is crucial since it influences both the long term stability and the electron transfer properties. Lack of systematic studies on anchoring groups have narrowed the choice of the anchoring group to few moieties, leaving this element of the device far from being optimized. We have developed a computational procedure to screen different anchoring groups used or usable to connect a dye to the semiconducting surface in a dye sensitized solar cell (DSSC). In this chapter, we study the performance of several anchoring groups used in DSSC, which have been chosen both for their different chemical properties and for the different chemistry of adsorption on the semiconductor surface. The injection times have been evaluated for perylene derivatives bearing these anchoring groups, applying the matrix partitioning scheme. Our procedure leads to a clear identification of the anchoring groups that bind strongly to the surface and facilitate the electron injection *at the same time*, providing clear cut indications for the design of new dyes. The complicated interplay of factors that determine the final results (preferred adsorption mode, the anchor's effect on the dye's electronic structure, and dye-semiconductor

coupling) are illustrated through few examples, showing how chemical intuition can often be misleading in this problem.

4.1 Introduction

Improving the efficiency of DSSCs is very challenging because each one of their components (nanocrystalline TiO_2, dye adsorbed on TiO_2, electrolyte or solid state hole transporter, additives and electrodes) cannot be improved independently from all the others. For example, a good dye should (i) be stably bound to the semiconductor surface, (ii) absorb solar radiation, (iii) in its photoexcited state inject very rapidly the electron into TiO_2, (iv) be easily regenerated by the redox pair in solution (or the hole transporting material), (v) avoid photodegradation, (vi) recombine as slowly as possible with the electrons in the semiconductor when oxidized. This very long list of requirements is even more complicated to satisfy if we consider that, by simply changing the additive[180] or the redox couple[13] in the cell, the energetics of the interface and therefore the electron transfer kinetics is completely changed and the best dye in some experiment is not necessarily the best in some other. The current research efforts include so many different directions (as described in Chapter 1) that, clearly, there are no established “optimal” components of the DSSC yet.

We show in this chapter that, notwithstanding the current limitations of computational chemistry methods, it is possible to define with a good degree of confidence at least one of the chemical characteristics of the solar cell: the anchoring group that connects the dye to the semiconductor.

The anchoring group determines the binding energy of the dye on TiO_2 (largely affecting its long term stability), the injection rate (mediating the electron transfer from the chromophore to the semiconductor) and can also modulate the injection energy by altering the energy of the dye's excited state. Introducing alternative anchoring groups can be synthetically laborious and, in the absence of alternative indications, the vast majority of dyes are anchored to TiO_2 with the carboxylic[12] and, sometimes, phosphonic[98] acid groups.

It is relatively straightforward to compute the binding energy of different anchoring groups.[171, 172] On the other hand, injection rate is affected by the dye's anchoring group in two ways: through the electronic coupling between the dye and the semiconductor, mediated by the anchoring group, and through the position of the dye's virtual orbital and its energy alignment with the TiO_2 conduction band. The former is the inherent property of the anchoring group, while the latter (the energy of the dye's virtual orbital) can also be altered by varying other functional groups in the dye, and its evaluation is also affected by the uncertainty in the computation of energy levels. Therefore, calculating the injection energy for a dye connected to TiO_2 through different anchoring groups will *not* provide a good indication of the inherent propensity of the anchoring group to facilitate the charge injection, because it will include both the effect of the semiconductor-dye coupling and of the variable injection energy. However, by a simple adaptation of the method already employed in Chapter 3, it is possible to compute the injection time for dyes connected through different anchoring groups, assuming (imposing) a constant energy levels alignment between dye and semiconductor levels. In other words, it is possible to compare computationally the effect of changing *only* the anchoring group, obtaining insight that a collection of

experiments or straightforward computations cannot achieve. As discussed more extensively in ref.[15], fast injection is a necessary but not sufficient condition for high power conversion efficiencies (PCE). We stress that in this chapter we identify anchoring groups with fast injection rather than high PCEs, the latter being determined by the combination of all processes in the cell.

In this chapter, we consider a series of dyes that have the same aromatic part (perylene) but various anchoring groups, illustrated in **Figure 4.1** and labeled from (a) to (o), that will be considered together with the previous results on carboxylic and phosphonic acid binding groups. Perylene was chosen as it is a common reference for spectroscopic and computational studies and it is often used for fundamental studies of electron transfer in DSSC-related systems.[113] Perylene itself is not a very efficient DSSC dye compared to dyes with a donor-π-acceptor structure, which offers better efficiency.[39] However, our study aims to be almost independent from the choice of the dye and should be relevant to any organic dye containing one anchoring group.

The choice of anchoring groups is based on the available literature and several chemical considerations. Sulphonic acid anchors (a) have been used in ref.[181] with hemicyanine and merocyanine dyes; a modified N3 dye with a boronic acid linker (b) has been reported;[182] acetyl-acetone (c) and hydroxamic acid (d) groups have been used for TiO_2 nanoparticle functionalization and to connect Mn(II)-complexes to the TiO_2 surface;[183, 184] (e), (f), (g), (h), (i) are studied here to make a detailed comparison between carboxylic acid and the aldehyde, ketone, amine, thiocarboxylic acid and nitro-group. The models (j) and (k) are studied to describe the adsorption on TiO_2 of anhydrides and imides present in the commonly used PTCDA and PTCDI dyes.[185-187] (l) is first proposed as a DSSC dye in this chapter: its high acidity

facilitates the adsorption of a proton on the semiconductor surface, thus favoring the formation of Ti-N bond and a possible tridentate adsorption mode. Ruthenium complexes featuring (m) as anchoring group have been initially proposed in ref.[188]. Finally, we study (n) and (o) because the cyano (CN-) and isothiocyano (NCS-) moieties are often featured in both organic and metal-organic dyes[39] (including the solvent, acetonitrile, used in many DSSCs) and, by including them in the calculations, we can estimate their contribution to the dyes' surface binding energy and evaluate the possibility of electron injection mediated by them.

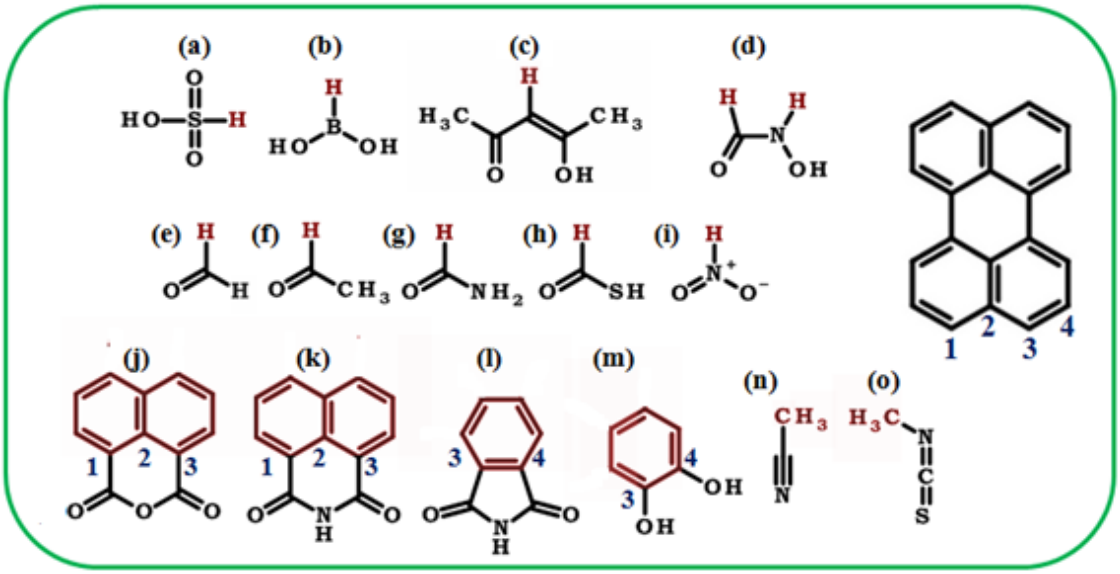

Figure 4.1: (a)-(o) are the molecules with model anchoring groups studied in this chapter for the calculation of the binding energy. For the calculation of the injection time these molecules have been modified to include the perylene dye. In (a)-(j) the H atom in red was substituted with the perylene connected via the carbon in position 1 (for molecules in (d) two separate dyes have been considered by substituting selectively only one of the two H atoms). For (j)-(m), the aromatic portion in red was augmented to give the full perylene structure keeping the indicated atom numbering of the perylene. For (n) and (o) the methyl group was substituted with the perylene, connected with the anchoring group from position 1.

4.2 Computational strategy

The method described in Chapter 2 and already adopted in Chapter 3 is employed to compute electron injection rates that are expressed by the following equation:

$$\hbar\Gamma = 2\pi \sum_{mn} c_m c_n^* \sum_{kk'} V_{mk} V_{nk'}^* \rho_{kk'}(E_i) \qquad (4.1)$$

In this case, we exploit the partitioning scheme to consider the injection through a large number of anchoring groups without repeating the calculation of the full chromophore on the TiO_2 slab. As we want to consider the effect of the anchoring group on the TiO_2-dye coupling independently from its role in shifting the LUMO energy, we enforce the LUMO energy E_i to be constant for each dye (0.4 eV above the CB edge). This also allows us to use a smaller slab than in ref.[148] (the thickness of the slab affects the position of the TiO_2 conduction band and, therefore, the energy level alignment, but not the dye-TiO_2 coupling). This is not to be considered an approximation but a numerical strategy to separate the anchoring group's effect on the coupling and to factor out its effect on the LUMO energy. **Table 4.2** reports also the (similar) results obtained using the calculated dyes' LUMO energies.

All-electron quantum chemical calculations were performed with CRYSTAL09 code[173] using the B3LYP density functional[147] and Gaussian basis set (triple valence plus polarization for Ti, O, and S and double valence plus polarization for C, N, B and H).[243] For the periodic calculations the k-points sampled were chosen using a Monkhorst-Pack net with a 2 × 2 × 1 k-points grid. Rutile (110) and anatase (101) surfaces were modeled using slabs containing two Ti_2O_6 layers with the 2×2 (as done in Chapter 3) or 2×4 cell area (the larger cell was used for the larger molecules (c), (i), (j) and (k)). The reported binding energies are corrected for basis set superposition error.[189]

TD-DFT calculations at the B3LYP/6-31G* level of theory were performed with Gaussian03[190] for isolated functionalized perylene molecules, in order to compute oscillator strengths and absorption energy shifts induced by the anchoring group.

4.3 Results and discussion

We studied the attachment chemistry and computed the binding energies of 15 different anchoring groups on both anatase (101) and rutile (110) surfaces. Most of the groups have multiple stable adsorption modes, with different adsorption energies (see **Table 4.1, Figure 4.2** and **Figure 4.3** for adsorption energies and geometries, respectively).

For example, boronic acid on anatase (101) adsorbs in two monodentate configurations (i.e. with one oxygen in close contact with one Ti atom); one is dissociative (i.e. with one acidic hydrogen adsorbed on the surface as a separate atom) and one is molecular (i.e. keeping the same chemical connectivity of the isolated molecule). The boronic acid has also four bridging bidentate adsorption modes (two oxygens of the molecule closely interact with two different Ti atoms); one is molecular and the other three dissociative. We have identified in total 35 adsorption modes on anatase (101) and 26 adsorption modes on rutile (110). For each anchoring group and each observed adsorption geometry we computed the electron injection time, for a perylene molecule bearing the group on anatase (101) and rutile (110). The full set of results is provided in **Table 4.1**, where we report the full set of adsorption energies (the negative of the binding energies) of the studied anchoring groups on anatase (101) and rutile (110). The energies are calculated for all the optimized adsorption geometries, which are labeled according to the following criterion: for each anchoring group, labeled as in **Figure 4.1**, we describe

the adsorption geometry as “M” for monodentate adsorption, “CB” for chelating bidentate, “BB” for bridging bidentate, “BT” for bridging tridentate. Different adsorption modes of an anchoring group, belonging to the same class, are numbered. Next to the adsorption energy, we also report the information on the connectivity of the adsorbate: we distinguish among molecular adsorption (*m*), where the molecule has the same connectivity as if isolated, dissociative adsorption (*d*) where a proton belonging to the molecule is adsorbed on a surface oxygen, and double dissociative adsorption (*dd*) where two protons belonging to the anchoring group are adsorbed on two different surface oxygens. We also report the computed injection times for a perylene molecule bearing the anchoring group. In the studied chromophores, the aromatic core of the perylene molecule substitutes the red coloured hydrogen atoms for anchoring groups (a)-(i). For hydroxamic acid (d) the perylene core can be attached substituting the hydrogen belonging either to the carbon or to the nitrogen, therefore we considered the injection for both, where allowed by the adsorption geometry, and we labeled them as dN and dC, respectively; for anchoring groups (j)-(m) the aromatic cores of naphthalene, phtalimide and catechol are expanded; finally, for (n) and (o), the perylene replaces the methyl moieties of the anchoring groups (see **Figure 4.1**). The most stable geometries are highlighted in bold. The injection times are computed for each optimized adsorption geometry, using the energy of injection 0.4 eV above the CB edge of anatase (101) and rutile (110) slabs.

Table 4.1: Adsorption energies (kcal/mol) of anchoring groups (a)-(o) for each optimized adsorption geometry and electron injection times (fs) of the respective functionalized perylene molecules on anatase (101) and rutile (110), respectively.

Anchoring group	**Ads. Geom.**	**Anatase (101)**		**Rutile (110)**	
		Ads. energy (kcal/mol)	**Injection time (fs)**	**Ads. energy (kcal/mol)**	**Injection time (fs)**
(a) Sulphonic acid	M	**−26.48 *d***	**11.02**	–	–
	BB	−20.14 *d*	5.18	**−26.45 *d***	**2.66**
(b) Boronic acid	M1	**−23.84 *m***	**49.97**	−23.81 *m*	76.14
	M2	−0.66 *d*	24.40	–	–
	BB1	−14.46 *m*	61.92	−21.47 *m*	23.47
	BB2	−19.40 *d*	38.27	**−34.28 *d***	**9.33**
	BB3	−15.27 *dd*	12.27	−23.04 *dd*	19.69
	BB4	−23.08 *dd*	10.74	–	–
(c) Acetyl-acetone	M1	−13.33 *d*	4.69	−11.58 *m*	11.07
	M2	**−25.80 *d***	**3.90**	–	–
	BC	−5.78 *d*	2.96	–	–
	BB	−25.26 *d*	2.75	**−22.36 *d***	**1.35**
(d_c)	M	−17.01 *m*	21.3	–	–
Hydroxamic acid	BB	**−26.48 *d***	**4.02**	**−31.53 *d***	**5.00**
(d_n)	M	−17.01 *m*	14.04	–	–
Hydroxamic acid	BB	**−26.48 *d***	**3.05**	**−31.53 *d***	**2.08**
(e) Formaldehyde	M	**−18.10 *m***	**21.96**	**−10.96 *m***	**9.43**
(f) Acetaldehyde	M	**−14.53 *m***	**25.15**	**−12.06 *m***	**13.13**
(g) Formamide	M1	**−26.25 *m***	**18.21**	−20.19 *m*	12.54
	M2	−17.58 *m*	12.65	–	–
	BB	−16.97 *d*	4.96	**−21.75 *d***	**9.63**
(h)Thioformic acid	M1	**−27.11 *m***	**4.98**	−14.91 *m*	3.13
	M2	−7.44 *m*	33.60	–	–
	CB	+ 0.52 *d*	8.088	–	–
	BB1	−24.37 *d*	1.013	−18.44 *d*	2.64
	BB2	–	–	**−24.72 *d***	**1.92**
(i) Nitro-group	M	**−8.41 *m***	**35.20**	–	–

	BB	–	–	**−13.49 *m***	**12.58**
(j) Dianhydride	M	−13.88 *m*	10.88	–	–
	BT	–	–	−7.97 *m*	24.43
(k) Naphthalimide	M	**−20.67 *m***	**3.42**	−10.74 *m*	4.64
	BB	−6.57 *d*	9.71	–	–
	BT	–	–	**−21.07 *d***	**2.02**
(l) Phtalimide	M1	**−29.43 *m***	**3.33**	−8.07 *m*	6.14
	M2	−17.11 *d*	4.44	–	–
	BB	−11.51 *d*	1.59	–	–
	BT	–	–	**−28.18 *d***	**2.56**
(m) Catechol	M1	–	–	−8.50 *m*	252.14
	M2	−15.57 *d*	1.02	−18.32 *d*	3.36
	BB1	−14.23 *dd*	0.59	**−22.24 *dd***	**2.12**
	BB2	**−21.14 *dd***	**0.22**	–	–
(n) Acetonitrile	M	**−15.22 *m***	**3.25**	**−16.44 *m***	**7.22**
(o)Thiocyanomethane	M	**−3.60 *m***	**55.41**	**−4.97 *m***	**44.57**

In **Table 4.2**, we report the electron injection time for the (a)-(i) functionalized perylene molecules on the anatase (101) surface, for the most stable adsorption geometries, computed also adopting the proper LUMO energy for each dye. We observe that the effect of the LUMO energy is less strong than the effect of the coupling but still significant. In particular, we observe that injection times decrease as the injection energy (given by the LUMO energy) increases, as expected using the concept of the injection driving force (the difference between the dye LUMO and the bottom of the conduction band). We also observe a negative (slowing down) effect on injection for molecules whose LUMO is positioned too deep in the CB (e.g. for dye (b) LUMO = -2.03 eV) or too close to the CB edge. The most important observation, however, is that there is a very strong correlation and similarity between the injection time computed

with the two values of the LUMO energy, i.e. the rates as presented in this work of thesis are very close to those expected for a realistic perylene molecule with the corresponding anchoring group.

Table 4.2: Electron injection times for functionalized perylene molecules (a)-(i) on anatase (101) computed considering $E_{inj}=E_{LUMO}$. We also report the computed LUMO energy for each dye.

Anchoring group	**Ads. geometry (anatase 101)**	**LUMO energy (eV)**	**Injection time using E_{inj} = E_{LUMO} (fs)**	**Injection time using E_{inj} = E_{CB}+0.4 eV (fs)**
(a) Sulphonic acid	M	−2.51	5.53	11.02
(b) Boronic acid	M1	−2.03	65.69	49.97
(c) Acetyl-acetone	M1	−2.26	3.01	3.90
(d_C) Hydroxamic acid	BB	−2.35	4.20	4.02
(d_N) Hydroxamic acid	BB	−2.23	1.70	3.05
(e) Formaldehyde	M	−2.50	18.03	21.96
(f) Acetylaldehyde	M	−2.34	14.53	25.15
(g) Formamide	M1	−2.09	14.32	18.21
(h) Thioformic acid	M1	−2.54	3.75	4.98
(i) Nitro-group	M	−2.90	40.63	35.20

Finally, we verify if the introduction of certain anchoring groups may have an effect on the optical properties of the molecule. In **Table 4.3**, we report the excitation energies and the respective oscillator strengths for the (a)-(i) perylene molecules, computed with TD-DFT calcultions on the optimized structures, at the B3LYP/6-31G* level of theory. Only molecules (l), (i) and, to some extent, (d_C) are substantially modified in their optical properties by the anchoring group.

Table 4.3: Absorption energies (eV) and oscillator strenghts for the first three excitations of the (a)-(o) functionalized perylene molecules. Level of theory: TD-DFT/B3LYP/6-31G*.

Anchoring group	**First excitation**		**Second excitation**		**Third excitation**	
	Abs. energy	**Osc. strength**	**Abs. energy**	**Osc. strength**	**Abs. energy**	**Osc. strength**
(a) Sulphonic acid	2.7816	0.3982	3.6980	0.0033	3.9120	0.0181
(b) Boronic acid	2.7928	0.3987	3.6922	0.0140	3.8821	0.0031
(c) Acetyl-acetone	2.6935	0.4746	2.8680	0.0441	3.6323	0.0040
(d_C) Hydroxamic acid	2.8828	0.3833	3.7593	0.041	3.8647	0.018
(d_N) Hydroxamic acid	2.7091	0.4566	3.5538	0.0610	3.9423	0.0050
(e) Formaldehyde	2.6747	0.4072	3.2645	0	3.6002	0.0163
(f) Acetylaldehyde	2.7135	0.4379	3.3766	0.0030	3.6589	0.0271
(g) Formamide	2.7835	0.3964	3.6847	0.0013	3.7867	0.0101
(h) Thioformic acid	2.6077	0.4285	3.5334	0.0100	3.6167	0.0035
(i) Nitro-group	2.5123	0.3798	3.4138	0.0330	3.4704	0.0259
(j) Dianhydride	2.6230	0.4870	3.5645	0	3.5874	0.0010
(k) Naphthalimide	2.6199	0.5005	3.3367	0.0010	3.5717	0
(l) Phtalimide	2.4451	0.2487	3.2360	0.1165	3.4540	0
(m) Catechol	2.702	0.333	3.5481	0.0215	3.7102	0.0114
(n) Acetonitrile	2.7587	0.4144	3.6748	0.0013	3.8411	0.0035
(o)Thiocyanomethane	2.6921	0.5997	3.5926	0.0101	3.6626	0.0023

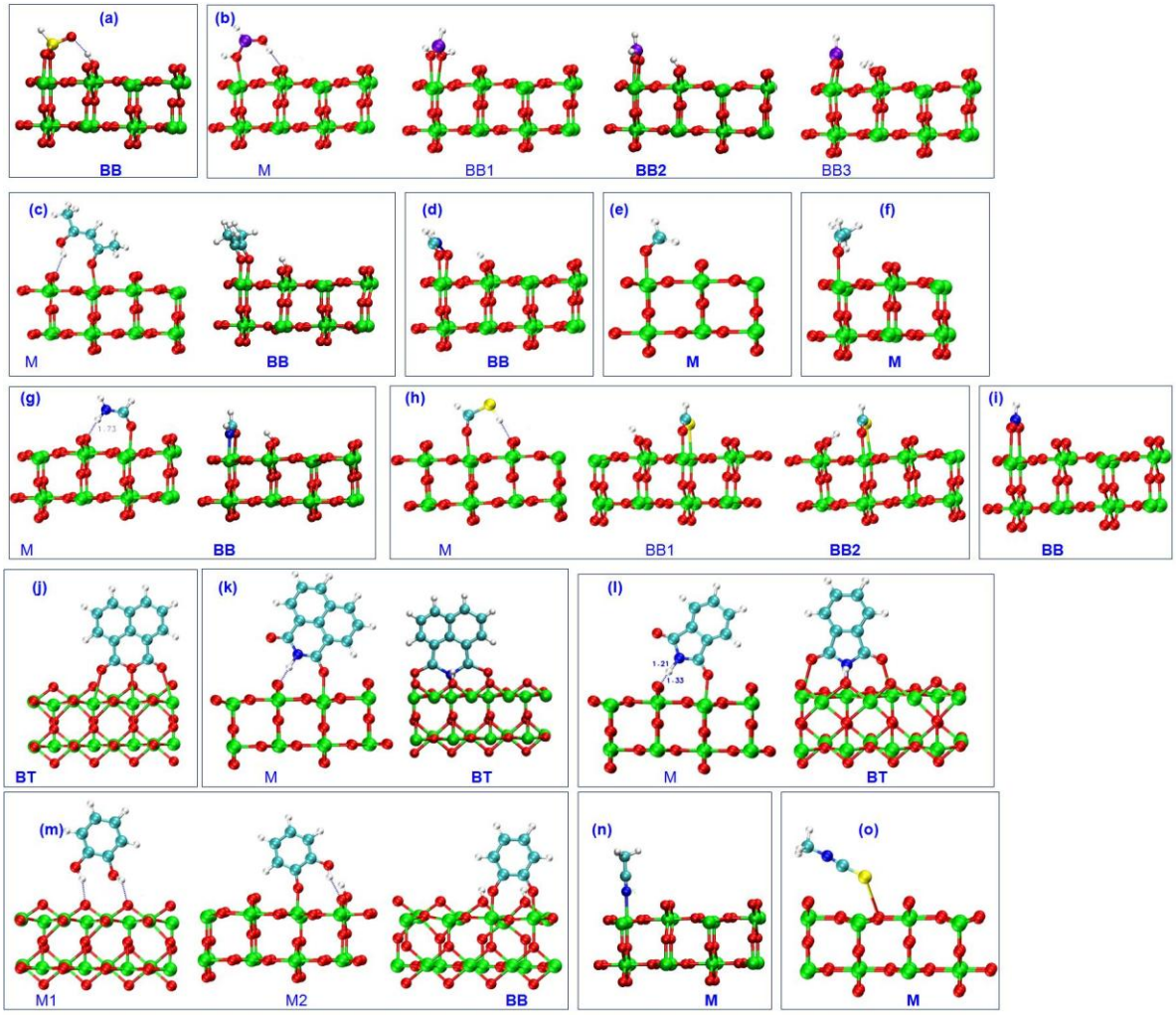

Figure 4.2: Adsorption configurations of anchoring groups (a)-(o) on rutile (110). Ti atoms are in green, O in red, C in cyano, H in white, N in blue, S in yellow and B in violet.

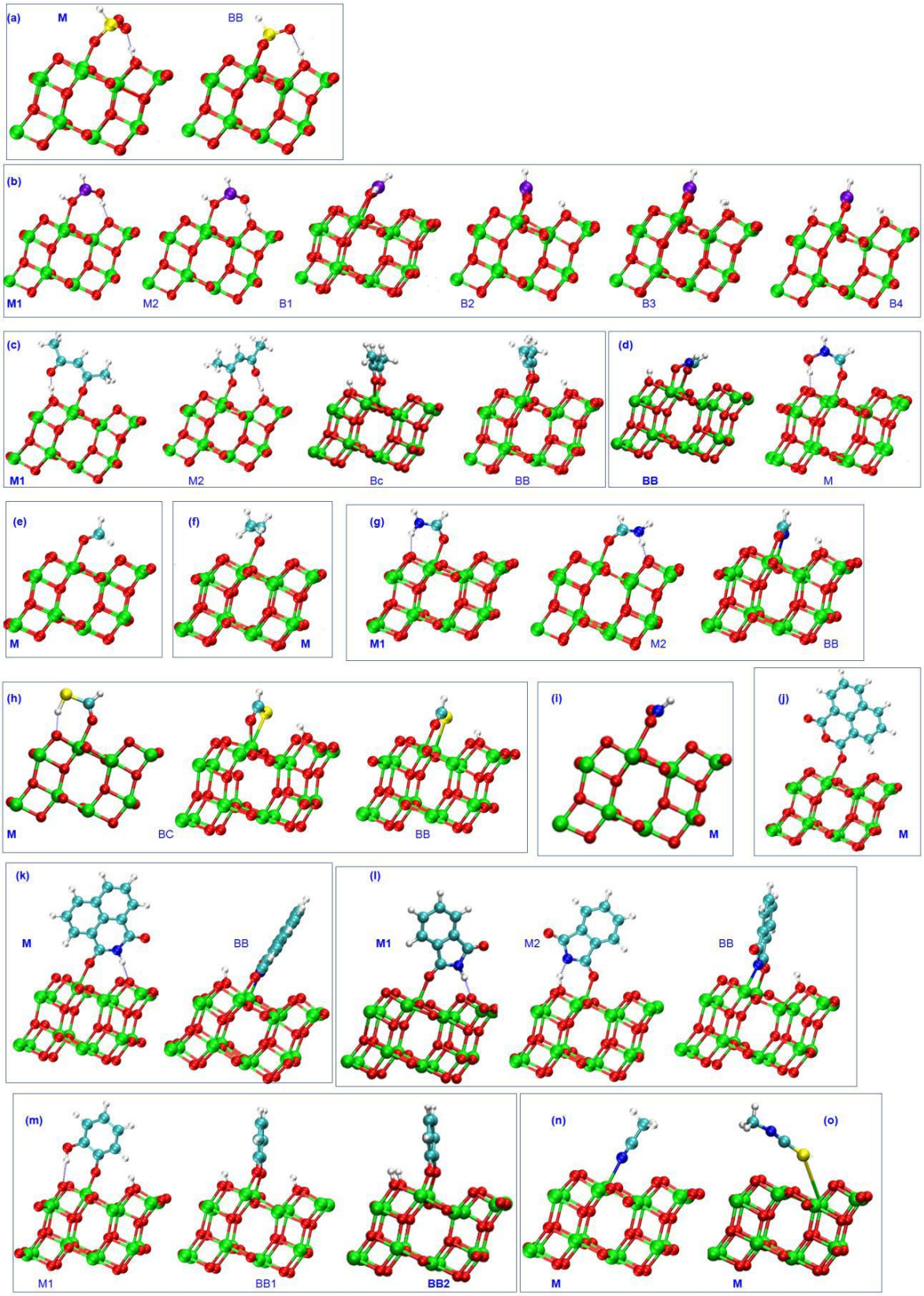

Figure 4.3: Adsorption configurations of anchoring groups (a)-(o) on anatase (101). Ti atoms are in green, O in red, C in cyano, H in white, N in blue, S in yellow and B in violet.

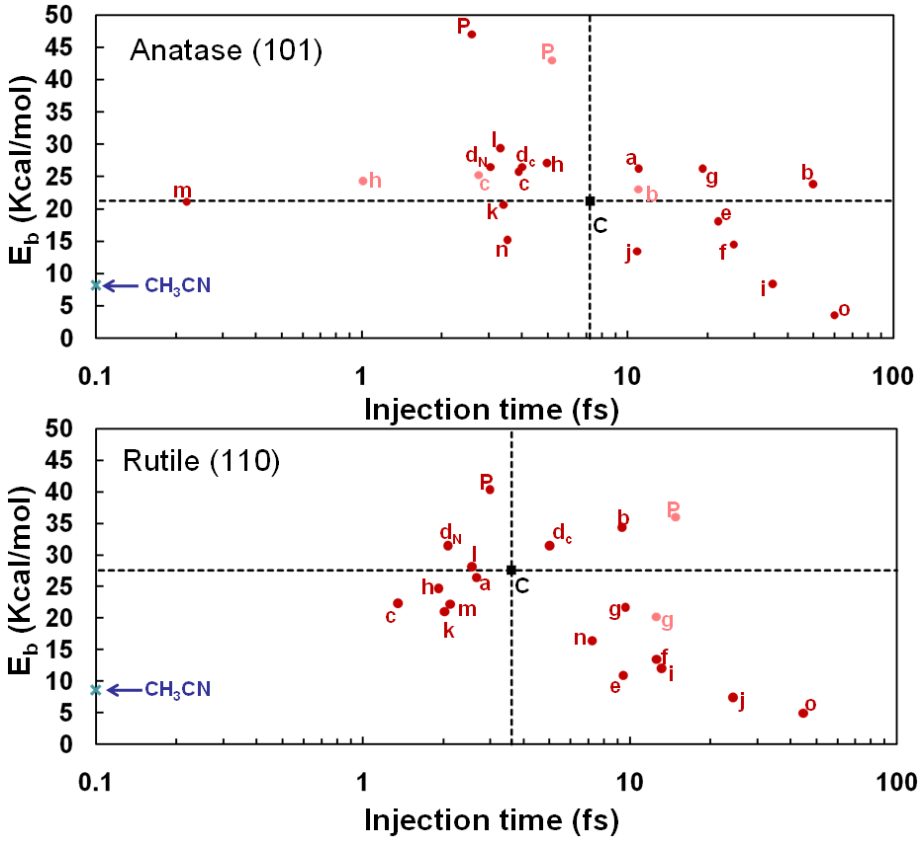

Figure 4.4: Electron injection times vs adsorption energy for different anchoring groups (a-o) for anatase (101) and rutile (110). Calculations of carboxylic acid (C) and phosponic acid (P) (from Chapter 3) are included. The adsorption energy of the solvent (acetonitrile) is indicated for reference. The data points in red are for the most stable adsorption geometry, in lighter color for the second most stable adsorption geometry (if within 4kcal/mol).

In the top panel of **Figure 4.4** we report a chart of the computed electron injection times of functionalized perylene molecules on anatase (101) vs the binding energy on the surface for each anchoring group in its most stable adsorption geometry. We have also reported (in lighter color) the data for the second most stable adsorption geometry if less than 4 kcal/mol higher in energy. To better evaluate the relative magnitudes of adsorption energies, the figure contains a horizontal dotted line corresponding to the binding energy of the carboxylic group (the most used anchoring group). The figure also reports, for reference, the binding energy for acetonitrile (the solvent commonly used in DSSCs), since binding energies close or smaller to that of the solvent are clearly too

low. In the same figure we represent with a vertical dotted line the injection time of the perylene chromophore connected to TiO_2 through the carboxylic acid. This representation allows an immediate visualization, in the top left quadrant of the diagram, of the anchoring groups that can be considered promising alternatives to the common carboxylic acid. Anchoring groups outside this quadrant should be discarded because they will be lacking in good properties of stability and/or injection. Some correlation between strong binding and fast injection can be observed in the figure, but this is too weak to be used for predicting one property from the other and the results should be analyzed individually.

Acetyl-acetone (c) and hydroxamic acid (d) anchors display good computed binding and injection characteristics, in agreement with the experiments.[183, 184] In particular, hydroxamic acid in its bridging bidentate configuration has a stable di-ionic form and features very fast injection when the dye is attached replacing the hydrogen bonded to the nitrogen atom. Catechol (m), in its bridging bidentate mode with two hydrogens donated to the surface, is the fastest injecting anchoring group (0.47 fs), due to the strong coupling given by the two oxydril groups directly linked to the aromatic core of the dye, with an adsorption energy similar to the carboxylic acid. The injection time of sulphonic (a) and boronic (b) acid are worse than the carboxylic acid (because of a low electron density of the LUMO on the atoms attached to the surface, see **Figure 4.5**) and the increase of adsorption energy is not enough to suggest their employment.

This is to be contrasted with phosphonic acid (P) (studied in Chapter 4) which has good injection properties and the strongest adsorption energy. Anchoring groups (e)-(i) are included as they all feature a simple modification of the common carboxylic acid. Somewhat expectedly, we find that the aldehyde (e) and the ketone (f) anchoring groups

give weaker binding and slower injection than the carboxylic acid: the lack of hydrogen bonds reduces the interaction with the surface and the coupling of the dye's LUMO with the CB of the semiconductor. The amide (g) has an increased binding energy (26.25 kcal/mol), but the effect of this anchoring group on electron injection is undesirable: due to its electron donating characteristics, the LUMO is more localized on the aromatic core of the dye, leading to a slower injection.

The relative injection time, however, is affected not only by the LUMO shape. The comparison between the anchors (g) and (i) illustrates well the importance of the full computational scheme, including the coupling with the semiconducting substrate, in comparison with simple chemical intuition. The strongly electron withdrawing nitro-group (i) would be expected to decrease the injection time, while the computed value is very large (35.20 fs) (considering its modest binding energy this is a very poor anchoring group). On the opposite end within the (e)-(i) family we find the thiocarboxylic acid (h) (4.98 fs). An inspection of the LUMO isodensity for the two dyes (**Figure 4.5**) does not explain the difference since they are fairly similar and the weight of the LUMO coefficients on the oxygen atoms attaching to the TiO_2 surface (see **Figure 4.3** for the anchor-slabs structures) is actually larger for the nitro-group than for the thio-acid. Analyzing the terms entering the rate equation we observe, in this case, that the difference is due to a larger coupling of the thio-acid with the TiO_2 orbitals (partially due to the S-Ti coupling and an additional hydrogen bond). This difference could not be predicted without an explicit calculation. Another clear example of the importance of calculations is the case of dye (m), which gives the fastest injection among all the considered functionalized perylene molecules. We observe, in this case, the competition between two effects. The two oxydril groups featured in (m) are π-

electron donating groups and the LUMO density on these two oxygen atoms is very low. However, when we look at the coupling between dye and semiconductor atomic orbitals we observe very strong coupling between Ti and C atoms in position 3 and 4 (**Figure 4.1**) with moderate O-Ti coupling for oxygen connected to position 3. Overall, the (m) anchor modifies the LUMO density so that the injection time is reduced but it also brings this density closer enough to the surface that the coupling effect dominates and the injection is overall much faster.

The characteristics of dianhydride and di-imide groups are studied through the model compounds (j)-(l). While the dianhydride moiety (j) is both weakly adsorbed and a slow injector, naphthalimide (k) and phtalimide (l) groups bind strongly to the semiconductor surface (20.67 kcal/mol and 29.43 kcal/mol respectively), due to the imide's proton hydrogen bond with the surface oxygen, and provide efficient electron injection for the related perylene molecules (~3.4 fs). The less strained geometry of the phtalimide bond with the surface is the likely reason for the different adsorption energies of the two different imides. Finally, our results show that the electron withdrawing and electron donating characteristics respectively of (n) (–CN) and (o) (–NCS) are reflected in the electron injection time for the corresponding dyes (3.3 fs and 55 fs). The large difference is also due to a strong N-Ti coupling of the –CN group while the long S-Ti bond (2.90 Å) of the –NCS moiety prevents efficient coupling. We, therefore, conclude that, while both these groups provide an increased stability to dyes featuring them in proximity of the surface, only the –CN group provides an efficient alternative pathway of injection.

The bottom panel of **Figure 4.4** shows the analogous results obtained for the same anchoring groups on rutile (110). The trend observed is similar but, here, bridging

bidentate adsorption modes are dominant, where allowed, and this is reflected in increased electron injection efficiency for the anchoring groups that feature molecular monodentate modes on anatase (101) but bidentate modes on rutile (110). On rutile (110) the carboxylic acid has a much stronger binding energy (~27 kcal/mol) so that, while many anchoring groups feature faster electron injection, only hydroxamic acid (dN) and phosphonic acid (P) are better anchoring groups here.

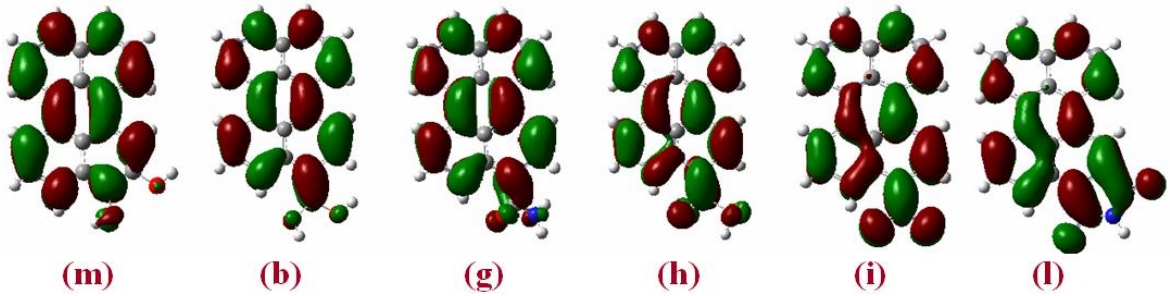

Figure 4.5: Isodensity representation of the LUMO orbital in the space for representative functionalized dyes (anchoring groups labeled as in **Figure 4.1**).

4.4 Conclusions

In this chapter we discussed a systematic procedure adopted to screen a large number of anchoring groups for dyes in DSSCs. Attachment chemistry and relative adsorption energies of a variety of moieties on both anatase (101) and rutile(110) have been investigated. Electron injection rates for perylene molecules bearing these groups have been computed, fixing the LUMO energy at 0.4 eV above the edge of the CB of the semiconductor, thus separating the effect of the anchoring group in shifting the LUMO energy from the effect of the semiconductor-anchor coupling, which is most interesting for us. This study led to a constructive design rule in the form of few promising anchoring groups for DSSC dyes (e.g. phosphonic acid, di-hydroxyl and some imides)

that can be used in substitution of the carboxylic acid and which should be intrinsically better at facilitating one of the key DSSC processes, electron injection, regardless of the other dye and device parameters. They should also preserve the long term stability of the device, granting stable adsorption on the semiconductor surface. Through a simple computational procedure we were able to decouple the ability of an anchoring group to inject an electron from all other effects that can be observed when a dye is modified in an experiment or in a computation (e.g. alteration of the surface dipole, coverage, adsorption energy). The proposed methodology is particularly important as we have shown that some of the results are not easily predictable on the basis of chemical intuition alone, because the electron injection rate is determined by the delicate balance between weights of dye's LUMO and orbital's couplings. While the former is due to the electron distribution of the dye, which can be intuitively predicted, the latter is influenced by the adsorption geometry and the surface electronic structure, which is much harder to guess and need an explicit calculation of the dye-semiconductor interface. However, this calculation can save weeks of experimental efforts in the design and synthesis of DSSC dyes bearing a novel anchoring group, since it provides all the information required to estimate adsorption strength on semiconductor surface and capability of favoring injection, through semiconductor-dye coupling.

Chapter 5:

Adsorption and electron injection of the N3 metal-organic dye on the TiO_2 rutile (110) surface

Abstract

Metal-organic ruthenium-based dyes are often used as a source of photogenerated electrons in dye sensitized solar cells and photocatalysis. Here, we study the relationship between adsorption geometry and electron injection properties of one of the most successful metal-organic dyes, N3 (cis-bis(isothiocyanato)-bis(4,4'-dicarboxy-2,2'-bipyridyl)-ruthenium(II)), on the TiO_2 rutile (110) surface. We systematically construct all possible adsorption configurations of the N3 molecule on this surface. By combining density functional theory calculations and electron transfer calculations, we find that a large number of adsorption configurations are possible – more than ten structures, which differ in the number of carboxylic and thiocyanate groups adsorbed and in the adsorption mode of the carboxylic groups, have similar adsorption energies and similar electron injection times. Therefore, the observed fast electron injection from this dye may originate either from one adsorption configuration or from several co-existing configurations. Our results suggest that related substituted metal-organic dyes with fewer anchoring groups will have good electron injection properties, even if only a small subset of adsorption configurations is available for them.

5.1 Introduction

As we addressed in the previous chapters, the development of new efficient dyes should be achieved systematically rather than by trial and error. To fulfill this goal, it is necessary to know the relationship between the dye's electron transfer properties and its structure and adsorption configuration. Ruthenium dyes, thanks to the experimental information already available, are a good model system to find such relationships, which can then be applied to design new metal-organic dyes. In fact, metal-organic ruthenium-based dyes are often used as a source of photogenerated electrons in dye-sensitized solar cells and photocatalysis.[12, 39] This class of dyes has good optical absorption properties and, until recently, provided the highest DSSC efficiencies.[13, 54-56] Moreover, metal-organic dyes represent a new challenge for the matrix partitioning scheme adopted in previous chapters as we would like to explore the potential of this method on this class of compounds. Ruthenium dyes usually have a complex attachment chemistry on TiO_2 surface with multiple carboxylic acid moieties binding the semiconductor. Therefore, the choice of the model for the anchoring group is not obvious and require a careful analysis of different possibilities and a comparison with the results obtained using the full dye.

One of the best known and most successful dye sensitiser molecules is the N3 dye (cis-bis(isothiocyanato)-bis(4,4'-dicarboxy-2,2'-bipyridyl)-ruthenium(II)) shown in **Figure 5.1**. DSSCs based on this dye showed up to 10% light conversion efficiencies.[54] Femtosecond spectroscopy measurements of electron injection from N3 into anatase and rutile polymorphs of TiO_2 (the most commonly used DSSC semiconductor) found that the fast component of electron injection takes place on the femtoseconds timescale:

<20 fs into nanocrystalline anatase[191-193] and <12 fs into rutile (110)-oriented single crystals[100, 101].

Numerous experimental and theoretical studies have investigated the details of the adsorption of N3 on TiO_2 surfaces, but the exact adsorption configuration remains unknown. Vibrational spectroscopy studies suggest that this molecule adsorbs via two[194] or more[195] deprotonated carboxylate groups, either in bridging bidentate or chelating configuration[194-197], although ester-type bonding was also proposed[198] and dismissed in later studies;[194-197] photoemission studies also point to adsorption via two deprotonated carboxylic groups.[100, 101, 199-201] In a scanning tunnelling microscopy (STM) study of N3 molecules adsorbed on the rutile (110) surface, the molecules were observed to be elongated along the [1-10] direction.[202] However, these studies still leave the question of whether this molecule adsorbs via carboxylate groups of the same or different bipyridyls, and whether there is one preferred adsorption configuration or several configurations co-existing or transforming into one another. First models of N3 adsorption were based on simple lattice matching, i.e. matching COOH-COOH distances in the molecule to various Ti-Ti distances on the TiO_2 surfaces.[196, 202-206] Theoretical calculations of N3 and a related doubly-deprotonated N719 dye on anatase (101) showed configurations adsorbed via the same[108, 207-212] or different bipyridyls[108, 208-211], either double bidentate[207, 210, 211] or mixed bidentate + monodentate[108, 208-212], as well as the presence of intermolecular hydrogen bonding[210, 211] and a possibility of interconversion between different configurations,[209, 210] e.g. depending on surface protonation. Electron transfer times only for one type of configuration (adsorbed via the same

bipyridyl) have been calculated,[207, 212] while the effect of adsorption configuration on electron transfer properties has not been studied theoretically.

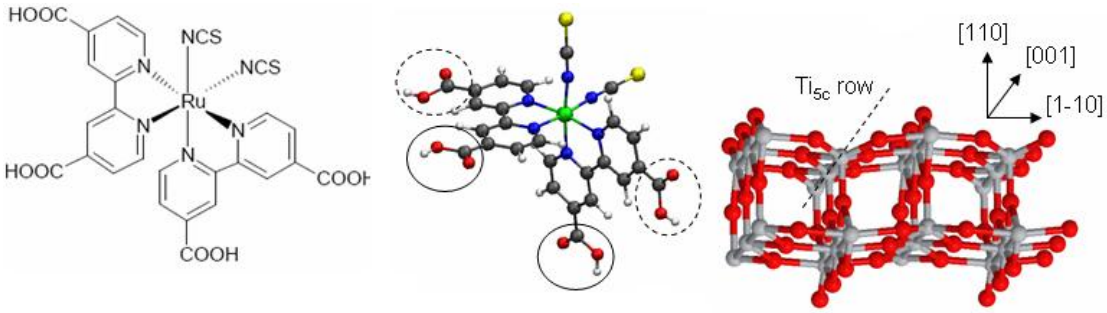

Figure 5.1: Chemical structure and molecular model of the N3 dye (cis-bis(isothiocyanato)-bis(4,4'-dicarboxy-2,2'-bipyridyl)-ruthenium(II)), with COOH groups trans to NCS marked with solid circles, and COOH groups cis to NCS with dashed circles; (2x3)-extended two-layer TiO_2 rutile (110) slab (half the area of the cell used in our DFT calculations) with the row of 5-coordinated Ti atoms marked.

The anatase polymorph of TiO_2 is the one most commonly used in DSSCs because it has a larger band gap than rutile (3.2 and 3.0 eV, respectively)[39] and because nanoscale anatase particles are more stable thanks to their low surface energy.[42, 43] However, nanoparticles are not ideal for obtaining atomic-scale information on molecular adsorption, because of the presence of different crystallographic surfaces and edges between different facets,[213, 214] while large anatase nanocrystals have not been artificially grown. On the other hand, rutile single crystals exposing the most stable (110) surface are available and widely studied, for example, as model surfaces for measurements of electron transfer.[102, 103, 167]

Recently, core-level photoemission spectroscopy studies of the N3 molecule have been reported[100], which provided insight into the dye-TiO_2 bonding. According to Ref.[100], the ratio of carbonyl oxygens (C=O bonding) to carboxylate oxygens (C-O bonding) in the adsorbed molecule is 1:3, this relationship suggests that the molecule adsorbs via two deprotonated carboxylic groups; the sulphur atom of one of the

thiocyanate groups also interacts with the substrate. Tentative models of adsorption configurations were proposed; calculations showed that the configuration involving two carboxylic groups of the same bipyridyl was more stable than the one involving carboxylic groups of different bipyridyls, and interaction of the S atom with the surface additionally stabilized the former structure.[100] However, in these calculations, only the molecule was optimized, while the surface atoms were fixed at their bulk positions, thus ignoring surface relaxation, which is significant for the rutile (110) surface.[215]

It is interesting to know how the adsorption mode influences the injection time in a system for which some information on the adsorption mode is accessible, in order to be able to apply this information to new related dyes. In this chapter, we study theoretically the adsorption of the N3 molecule on the TiO_2 rutile (110) surface and electron injection from N3 to TiO_2. We construct and optimise all possible adsorption configurations compatible with the rutile (110) surface. Then, we calculate the time of electron injection from the dye's lowest unoccupied molecular orbital (LUMO) to TiO_2 in these configurations, using the methodology described in detail in Chapter 2. We analyze the relationship between the adsorption configuration and electron injection properties, to find out which configuration or configurations are responsible for the observed fast electron injection from the N3 molecule to TiO_2. The adsorption-electron transfer relationship for the N3 dye is important not only for understanding this particular dye's behaviour, but also as a foundation for understanding and improving electron transfer properties of other metal-organic dyes.

5.2 Computational strategy

We performed DFT calculations using the CRYSTAL09 code[173], using B3LYP hybrid density functional[147] and localised all-electron basis sets. The following basis sets (available on CRYSTAL website[243]) were used: 86-411(d31) (triple valence plus double polarization) for Ti, 8-411(d1) (triple valence plus polarization) for O, 86-3111(d11) (quadruple valence plus double polarization) for S, 6-31(d1) (double valence plus polarization) for C and N, 31(p1) (double valence plus polarization) for H, 9766-311(d31) for Ru, where the numbers before the dash denote the number of primitive Gaussian-type orbitals (GTOs) in contraction for the basis functions of the core shells, the numbers after the dash – the same for valence shells, and in brackets – the outer p- (for H) or d-shell (polarization shell for Ti, O, S, C, N, H; partially filled shell for Ru). The basis for Ru (optimized for a mixed oxide $RuSr_2GdCu_2O_8$) was taken from M. Towler's web page (University of Cambridge);[216] the same basis was used in a recent study of ruthenium-tetracarbonyl polymers.[217]

The rutile (110) surface was modelled using a (2x6) slab with two O-Ti-O trilayers (6 atomic layers). **Figure 5.1** (right panel) illustrates the rutile (110) surface. Oblique cells were used, with the lattice vectors chosen so that the shortest distance between adsorbate molecules and their images is at least 5.5 Å. The complete system contained 203 atoms (144 in the substrate and 59 in the adsorbate). Atoms in the bottom O-Ti-O trilayer were fixed in their bulk positions, while the top trilayer and all atoms of the adsorbate were allowed to optimise. The Brillouin zone was sampled with four **k**-points.

The structures described in the following sections were initially optimized using the generalized gradient approximation (GGA) PBE functional[179], with the energy

threshold of 10^{-4} Ha, root-mean-square (RMS) of the gradient 10^{-3} Ha/Bohr, RMS of the displacement 1.2×10^{-3} Bohr; threshold for the self-consistent (SCF) loop convergence was 10^{-6} Ha. The optimized structures were then re-optimized using the B3LYP functional and the same optimization criteria. The B3LYP functional was used because it gives reasonable values of the TiO_2 band gap[148], as well as of HOMO-LUMO gaps of metal-organic molecules.[109]

Adsorption energies were calculated as the difference between the optimized surface-adsorbate system and the separately optimized surface and adsorbate, and corrected for the basis set superposition error (BSSE) using the counterpoise method.[189] The SCF loop of the "molecule + ghosts of surface" systems was difficult to converge for double bridging bidentate configurations, therefore we used an uniform value of 0.25 eV for the adsorbate contribution to the BSSE correction in these structures (cf. 0.13-0.22 eV values calculated for monodentate configurations), which is approximately 1/3 of the total BSSE correction.

The rates of electron injection were calculated using the procedure described in Chapter 2 and already adopted in Chapter 3 and Chapter 4.

$$\hbar\Gamma = 2\pi \sum_{m,n} c_m \, c_n^* \sum_{k,k'} (ES_{mk} - V_{mk})(ES_{nk'} - V_{nk'})\rho_{kk'}(E_s) \tag{5.1}$$

We showed in previous chapters, that the quantities appearing in Eq. 5.1 can be obtained with a high degree of accuracy from separate calculations of a slab with the dye's adsorbed anchoring group and the isolated dye. This partitioning allows us to avoid lengthy calculations of the full surface-adsorbate system. In this way, we were able to scan through many different dyes and anchoring groups.

However, in this case, because of the complex adsorption geometry of the dye, we considered the complete dye molecule instead of just the anchoring group for the calculations of V_{mk} and S_{mk}. The coefficients $\{c_m\}$ were calculated (i) for the isolated dye fixed in its adsorbed geometry (any deprotonated carboxylic groups were re-protonated for this purpose) and (ii) for the optimized isolated dye (oriented in such a way as to match the adsorbed dye structure). The resulting injection times for the two sets of $\{c_m\}$ were very similar, therefore we present only the results using the coefficients from calculation (i). We also compare these injection times obtained in the full surface-adsorbate system with injection times obtained by partitioning the system into smaller components, i.e. by using a smaller anchoring group.

We used the LUMO of the N3 molecule as the orbital from which injection takes place. Computational studies of electronic and optical absorption properties of isolated ruthenium dyes (in the gas phase and in solution) showed that the lowest excited state involves a combination of transitions from the HOMO, HOMO-1 and HOMO-2 to the LUMO, LUMO+1 and LUMO+2, and all these LUMOs are similarly localized on the bipyridyl ligands and their carboxylic groups.[218, 219] For simplicity, we consider only the LUMO orbital, and we expect that injection properties of the other low-lying LUMOs are similar.

5.3 Results and discussion: attachment chemistry of N3 dye on TiO_2 rutile (110)

5.3.1 Adsorption configurations of N3 dye on TiO_2 rutile (110)

We systematically constructed all possible adsorption configurations for the N3 dye on the rutile (110) surface, taking into consideration the earlier theoretical and

experimental results on the adsorption of carboxylic acids[105, 172], including biisonicotinic acid[220, 221] (the 4,4'-dicarboxy-4,4-bipyridine molecule, which is a ligand in the N3 molecule), on this surface. It is known from experimental and computational studies that simple carboxylic acids, such as formic and benzoic acid, bind to two 5-coordinated Ti atoms (Ti_{5c}) in a bridging bidentate (BB) configuration;[172] a non-dissociated monodentate (MH) configuration has also been studied theoretically, but it had a smaller adsorption energy on sufficiently thick slabs,[162, 172] and has not been observed experimentally.[105] Biisonicotinic acid, according to semi-empirical calculations[220] adsorbs on the rutile (110) surface diagonally over two Ti_{5c} rows, with the two deprotonated carboxylic groups being shifted with respect to each other by one crystallographic unit cell along the [001] direction: this configuration both had a larger adsorption energy than the alternative deprotonated structures, and the molecule's tilt angle was compatible with experimental NEXAFS results;[220] the stability of this configuration was later confirmed also by DFT calculations.[221]

The chemical structure and a molecular model of the N3 molecule, as well as a two-layer rutile (110) slab, are shown in **Figure 5.1**. Below, we will discuss the possible adsorption configurations compatible with the (110) surface, which are schematically illustrated in **Figure 5.2**. The rows of 5-coordinated Ti atoms are shown in **Figure 5.2** as dashed lines, adsorbed carboxylic groups are marked with red circles (connected by a thick red line if they belong to the same bipyridyl), and S atoms of the NCS group (if close to the surface) are also indicated. The molecule can, in principle, adsorb via one, two or three carboxylic groups (configurations 1, 2-11 and 12, respectively).

Note that there are two inequivalent types of carboxylic groups in the N3 molecule – cis and trans to the NCS group (see **Figure 5.1**); their deprotonation constants were shown experimentally to be different[222]. Thus, even in the simplest configuration 1 adsorbed via one carboxylic group, there are two possible structures – adsorbed via the cis or trans carboxylic group.

When we consider adsorption via two carboxylic groups, these two groups can belong to the same or different bipyridyls. In configurations involving the same bipyridyl, the molecule can adsorb across two Ti_{5c} rows (configuration 2, the most stable biisonicotinic acid adsorption configuration according to Ref.[220]) or along one Ti_{5c} row – configuration 3 (not considered in earlier studies of biisonicotinic acid adsorption), and the molecule adsorbed in either of these ways can be tilted so that the NCS group is close to the surface (configurations 4 and 5, respectively).

There are even more possibilities for adsorption via carboxylic groups of different bipyridyls, if we take into account the inequivalence of the cis and trans carboxylic groups. The molecule can adsorb via two carboxylic groups trans to NCS or one group cis and the other trans to NCS across two Ti_{5c} rows (configurations 6 and 7, respectively), and similarly above one Ti_{5c} row (configurations 8 and 9, respectively). Adsorption via two carboxylic groups cis to NCS is not possible, because they are at the opposite ends of the molecule. Additionally, when the molecule is adsorbed via one trans and one cis carboxylic group, the NCS group can be close to the surface – configurations 10 and 11 above two or one Ti_{5c} rows, respectively. Finally, the molecule can adsorb via three carboxylic groups – we found only one such configuration compatible with the periodicity of the rutile (110) surface, configuration 12.

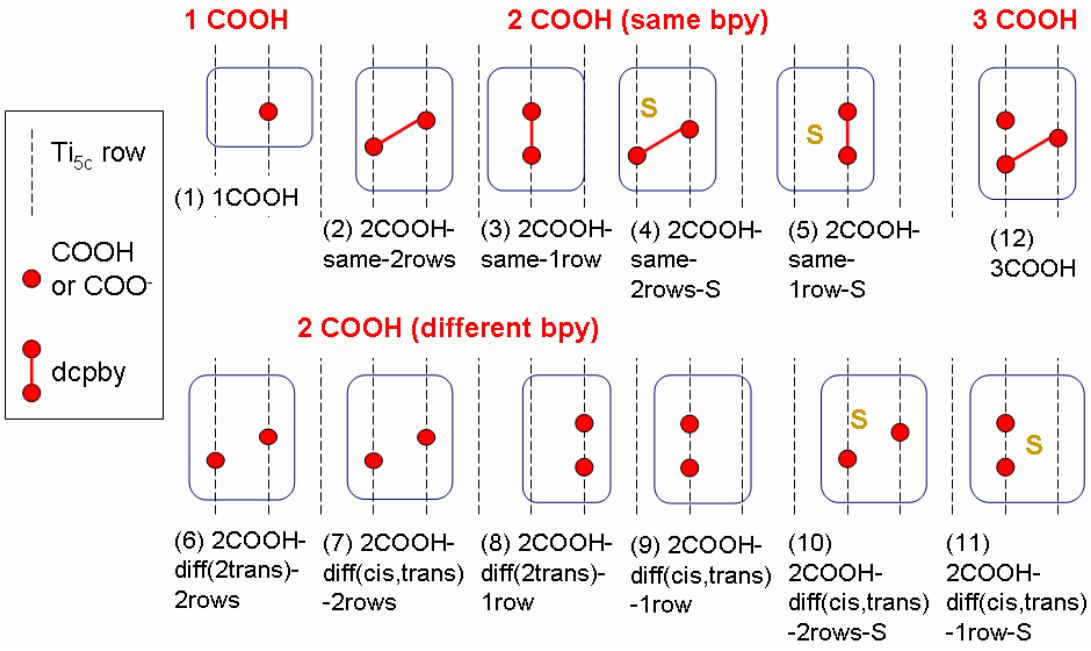

Figure 5.2: Schematic representation of adsorption configurations of the N3 molecule on the rutile (110) surface. Rows of 5-coordinated Ti atoms are shown as dashed lines (see also **Figure 5.1**); adsorbed carboxylic groups are marked with red circles (connected by a thick red line if they belong to the same bipyridyl), and S atoms of the NCS group (if close to the surface) are also indicated. The configurations are labelled according to the number and type of adsorbed carboxylic groups and according to the number of Ti_{5c} rows (one or two) covered.

5.3.2 Stabilities of the adsorption configurations

We simulated the configurations corresponding to the schematics in **Figure 5.2** adsorbed on the (2×6) periodic rutile (110) slab. For all the structures, we modelled adsorption of the carboxylic groups in the bridging bidentate mode, which is the most stable one for carboxylic acids on rutile (110). However, for structures where the BB configuration is strained, or where it converted into a deprotonated monodentate ester-type structure (labelled M), we additionally considered protonated monodentate adsorption (labelled MH). In the following, we use the word "configuration" to describe adsorption sites (as shown in **Figure 5.2**), and "structure" or "geometry" to describe the details of adsorption, such as BB, M or MH adsorption modes and hydrogen bonding to the surface.

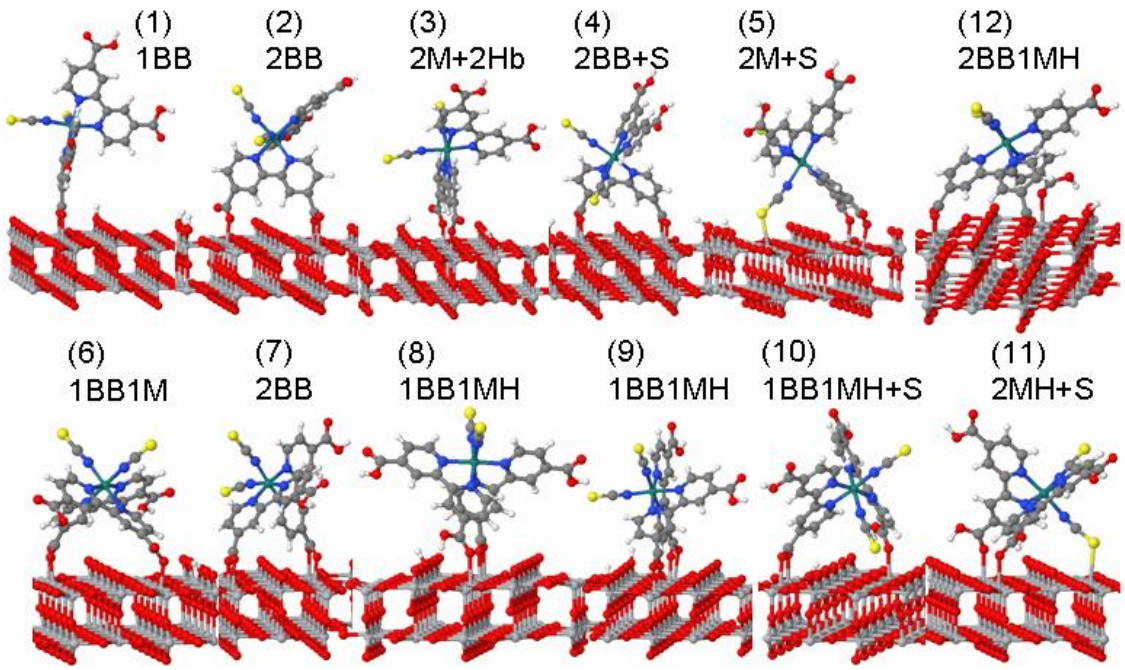

Figure 5.3: Most stable adsorption geometries for each configuration (see also **Table 5.1**).

Figure 5.3 shows the adsorption geometries for the most stable structure for each configuration. The adsorption energies of all studied structures are presented in **Table 5.1**. Adsorption energies are mainly between -1.09 and -0.5 eV (negative adsorption energy means the strongest adsorption; the positive adsorption energy of 0.09 eV is due to the approximate nature of the BSSE correction and certainly corresponds to the weakest adsorption); these energies are in agreement with the literature values for N3 an N719 on anatase (101)).[210, 211] The two-layer slab is too thin to accurately represent adsorption energies on a large semi-infinite slab (at least four or five TiO_2 trilayers would be needed to reach converged slab thickness[148]), but our adsorption energies allow us to do a qualitative comparison of different structures.

Table 5.1: Adsorption configurations of N3 on the rutile (110) slab, their adsorption energies and injection times.

N°	Configuration	Structure		Adsorption energy, eV	Injection time, fs
		Starting	Final		
1	1COOH-trans	1BB	1BB	-1.07	11.8
	1COOH-cis	1BB	1BB	-1.08	26.3
2	2COOH-same-2rows	2BB	2BB	-0.99	4.1
3	2COOH-same-1row	2BB	2M+2Hbonds	-0.90	4.4
		2BB	2M	-0.62	23.2
		2MH	2MH	-0.68	19.6
4	2COOH-same-2rows-S	2BB+S	2BB+S	-1.01	4.6
5	2COOH-same-1row-S	2BB+S	2M+S	-0.96	11.4
		2MH+S	2MH+S	-0.84	90.7
6	2COOH-diff(2trans)-2rows	2BB	1BB1M	0.09	8.9
7	2COOH-diff(cis,trans)-2rows	2BB	2BB	-0.86	26.9
8	2COOH-diff(2trans)-1row	2BB	2BB	-0.10	6.0
		1BB1MH	1BB1MH	-0.67	11.9
		2MH	2MH	-0.63	26.7
9	2COOH-diff(cis,trans)-1row	2BB	1BB1M	-0.12	10.2
		1BB1MH	1BB1MH	-0.80	3.0
		2MH	2MH	-0.76	10.8

10	2COOH-diff(cis,trans)-2rows-S	2BB+S	1BB1M+S	-0.91	6.5
		1BB1MH+S	1BB1MH+S	-0.95	7.3
		2MH+S	2MH+S	-0.83	17.0
11	2COOH-diff(cis,trans)-1row-S	2BB+S	1BB1M+S	-0.91	5.9
		1BB1MH+S	1BB1MH+S	-0.79	4.7
		2MH+S	2MH+S	-1.04	14.0
12	3COOH	2BB1MH	2BB1MH	-1.04	7.3
	3COOH	3BB	3BB	-0.26	3.3

Surprisingly, even the best adsorption energies of the configurations adsorbed via two or three carboxylic groups are not larger than the configurations adsorbed via just one carboxylic group, and are close to the adsorption energies of formic and benzoic acid on a similar two-layer rutile (110) slab.[148] This shows that the energetic cost of deformation of this molecule is large and is comparable with the adsorption energy per single carboxylic group.

In the configurations adsorbed via two carboxylic groups, double BB adsorption is often unstable, and one or both of the carboxylic groups adopt monodentate adsorption M, where only one of the oxygens of the carboxylate is bonded to Ti, while the other oxygen forms a double bond to the carboxylate carbon. This ester-type adsorption was considered in early vibrational spectroscopy studies of N3 on anatase[198] and ruled out in later spectroscopic studies.[194-197] Where double BB structures exist in our calculations (configurations 2, 4 and 7), they have large adsorption energies.

Monodentate ester-type (M) and monodentate protonated (MH) structures have adsorption energies similar to each other, even though the details of the geometries are different: the former structures contain a double-bonded carbonyl oxygen and the latter have a carboxylic OH group, often hydrogen-bonded to the surface. According to calculations of formic acid on rutile (110)[148], the BB-MH energy difference is smaller for even-layer slabs than for odd-layer slabs, thus, in these thin two-layer slabs, the MH structure may be artificially stabilized. Still, our adsorption energies suggest that MH adsorption in this complex dye may be possible.

Configurations adsorbed via the same or different bipyridyl are similar in energies, unlike the results of Ref.[100] where adsorption via the same bipyridyl was significantly more favourable; adsorption across two rows was usually slightly (by 0.1-0.3 eV for same-bipyridyl structures) more favourable than across one row. Interaction of the sulphur atom of the NCS group with the surface additionally stabilized the structures by 0.05-0.3 eV, in qualitative agreement with the results of Ref.[100]. Only few structures can be definitely ruled, because of their adsorption energies: configurations 6 and 8 adsorbed via two carboxylic groups trans to NCS, and configuration 3 adsorbed via carboxylic groups of the same bipyridyl above one Ti_{5c} row. The configuration 12, adsorbed via three carboxylic groups, is comparable in energy to the most favourable two-carboxylate structures (double-BB configuration 4 and double-MH configuration 11, with sulphur-surface interaction present in both of these structures).

It is not possible, on the basis of our adsorption energies, to identify a single adsorbed structure which is more favourable than others. Instead, we find several configurations with similar stabilities, which may co-exist or convert into one another (as suggested in Ref.[210]). As discussed in earlier theoretical studies of ruthenium dyes on anatase

(101) [210, 211], the data on adsorption energies may be not enough to decide which adsorption configurations take place, and other properties of the adsorbate should be analyzed as well, such as the core-level spectra in Ref.[211], vibrational spectra in Ref.[210] and injection time in this chapter.

We can compare our results with published photoemission spectroscopy results.[100] The study in Ref.[100] found that the ratio of carbonyl oxygens (C=O) to carboxylic oxygens (C-O in COO^- of COOH groups) is 1:3, and interpreted it as double BB adsorption, which is consistent with our configurations 2, 4 and 7. We note that the results of Ref.[100] are also consistent with MH adsorption, which also would have two carbonyl oxygens (in the free COOH groups) and 6 carboxylic (C-O) oxygens: two in the free groups and four in the adsorbed groups. MH adsorption, to the best of our knowledge, has not been discussed experimentally for this dye, although we show in the next section that its slow electron injection is in disagreement with experiments.[100, 101, 191-193] Ref.[100] also found two different types of sulphur atoms and suggested that some of the sulphur atoms in the molecule interact with the surface, which is consistent with our configurations 4, 10, 11. Thus, configuration 4 is the one in best agreement with the conclusions of the study in Ref.[200], but we cannot rule out other two-carboxylate structures.

Our structures can also be compared with the STM studies of Ref.[202], where N3 molecules are imaged as ovals elongated along the [1-10] direction (although earlier STM studies by the same group, under different experimental conditions, imaged the N3 molecules as uniform bright spots without any special direction[205, 206]). STM measurements of TiO_2 surfaces image empty electronic states, therefore the unoccupied orbitals of N3 (localized on bipyridyl groups) are imaged. If we assume that the

adsorbed carboxypyridyl groups, which are coupled to the surface, are responsible for the STM image, configurations 2, 4, 6, 7, 10 adsorbed across two Ti_{5c} rows will be in agreement with the STM results of ref.[202] However, it is not possible to make further conclusions on the preferred structures without doing a simulation of their STM images.

When we compare stabilities of the different configurations, we should bear in mind that they correspond to the situation of adsorption in vacuum, whereas in real systems, the dye is adsorbed from solution (usually ethanol) and the DSSC is kept in acetonitrile (or sometimes water) solution. Thus, solvent molecules compete with the dye's carboxylic groups for adsorption sites. The adsorption energy of a single acetonitrile molecule (-0.7 eV as computed in Chapter 4) or water molecule on rutile (110) (-1.4 - -0.8 eV according to various DFT calculations reviewed in Ref.[223]) are larger than the difference between two-carboxylate and three-carboxylate adsorption and than the difference between one and two adsorbed carboxylates. Therefore, in solution, the competition with solvent molecules for Ti_{5c} adsorption sites is likely to favour two-carboxylate rather than three-carboxylate structures.

In this study we ignored adsorbate-adsorbate interaction, such as hydrogen-bonding. There is evidence of adsorbate-adsorbate interaction from experiment[202, 205, 206] (STM images showed the presence of both isolated and aggregated N3 molecules on the rutile (110) surface, with some preference for aggregation but no preferred direction of aggregation) and from calculations.[210, 211] Several of our structures can support hydrogen bonding with neighbour molecules (configurations 6 and 8 allow the formation of hydrogen-bonded chains and configurations 1-3, 7, 9, 10 allow hydrogen-bonded dimers) and can be additionally stabilized due to this hydrogen bonding. However, since intermolecular hydrogen-bonding involves free (not adsorbed)

carboxylic groups, we expect that it will not have a strong effect on electron injection times, which are the subject of the next section of the chapter.

5.4 Results and discussion: electron injection times of N3 dye on TiO_2 rutile (110)

5.4.1 Calculated injection times for the N3-TiO_2 system

We calculated injection times from the LUMO of the N3 molecule to the TiO_2 CB for all the studied configurations (last column of **Table 5.1**; the injection times for the most stable structure of each configuration are also plotted in **Figure 5.4**).

We find that injection from the molecule adsorbed via just one carboxylic group (configuration 1) is rather slow (12-26 fs), slower than the calculated[129, 168] and measured[102, 103] injection time from the isolated ligands (isonicotinic and biisonicotinic acid). The reason for this slower injection is probably that the LUMO is spread over several dicarboxybipyridyl ligands, not just the adsorbed ligand. The injection times for configuration 1 are also longer than the experimental injection time for N3 on rutile and anatase, 12-20 fs;[100, 101, 191-193] therefore, we can definitely conclude that the one-carboxylate configuration is not the one responsible for the measured fast injection from this molecule.

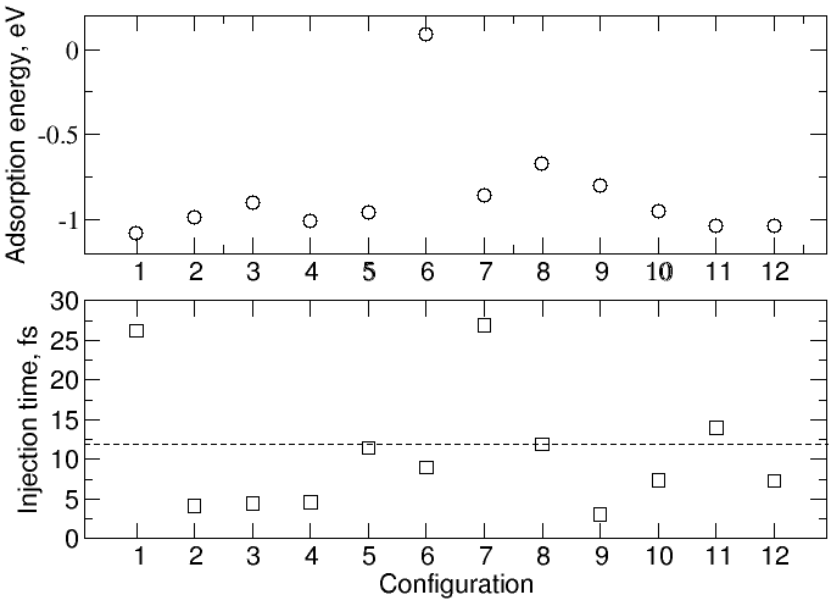

Figure 5.4: Adsorption energies (upper panel) and injection times (lower panel) for the most stable structure of each of the configuration (1-12). The dashed line in the lower panel shows the experimental upper limit for the injection time according to Ref.[101].

Among the configurations adsorbed via two or three carboxylic groups, the structures with only MH adsorption show slow injection, above the experimental value of 12 fs[101]; purely M adsorption also gives relatively slow injection, unless assisted by adsorbate-substrate hydrogen bonding (e.g. compare the several structures of configuration 3). Configurations with BB adsorption (either double BB, e.g. configurations 2, 4, or mixed BB and M or MH) show the fastest injection, similar to or faster than the experimental upper limit.

Thus, we have several configurations (2-4, 6, 9, 10, 12) with very different adsorption geometries, which, nevertheless, show similar adsorption energies and similar very fast injection times of <12 fs. This result (as well as adsorption energies being very similar

for many configurations) suggests that the measured injection times not necessarily originate from a single configuration. Instead, several adsorption configurations may co-exist and have similar fast injection times.

These results explain why both homoleptic dyes (having two equivalent bipyridyl ligands) and heteroleptic (having two different bipyridyl ligands), which are likely to have different adsorption geometries, have been efficient in DSSCs.[108, 109, 193, 224, 225] Our results on the similarity of different configurations' injection properties also reconcile several experimental studies, where, on the one hand, adsorption of N3 and its homoleptic analogue N719 are suggested to be the same,[196] and, on the other hand, electron injection properties of N3 are very similar to heteroleptic dyes that can adsorb only via carboxylic groups of the same bipyridyl.[193, 226] Co-existing configurations adsorbed via the same or different bipyridyl may be responsible for these conflicting results. Both homoleptic-type and heteroleptic-type sensitizers will have adsorption structures that have good electron injection properties.

5.4.2 Applicability of the matrix partitioning approach for calculating injection times

Even without the full search for the best adsorption configuration, the calculations of the N3 + surface system are very time-consuming and cannot realistically be done for each new metal-organic dye. It is desirable to have a quicker computational scheme for electron transfer rates calculations. In the previous chapters, we proposed the partitioning scheme for calculating electron injection times: instead of a full DFT calculation of the surface with adsorbed dye, separate calculations are done for (i) a small area of the surface, (ii) the surface's interface with a small anchoring group, and (iii) the isolated dye molecule; then, the electronic properties of these fragments are

combined to calculate injection time. This partitioning allowed us to avoid lengthy calculations of the full surface-adsorbate system and enabled us to calculate electron injection times for a series of organic dyes (Chapter 3), and for different anchoring groups attached to the same dye (Chapter 4). Here, we calculate the injection times of N3 using the partitioning approach and compare them with injection times calculated in the previous section for the full TiO_2 + N3 dye system, to check if the partitioning approach is applicable for the complex metal-organic dyes.

When we use a biisonicotinic acid molecule (in an adsorption configuration similar to Refs.[220, 221]) as an anchoring group, combined with the LUMO coefficients of an isolated N3 molecule, we obtain injection time of 11.3 fs, which is similar to the values obtained from the full calculation (slightly slower than the fastest times for the full system, 3-6 fs, but in very good agreement with the experimental upper limit of 12 fs[101]).

When we use benzoic acid as the anchoring group, the calculated injection time is 40 fs, which is comparable to the calculated injection time of N3 adsorbed via a single carboxylic group but too slow, compared to experiment. Therefore, we conclude that an anchoring group with two carboxylic groups attached to the surface (such as biisonicotinic acid) is needed for an accurate calculation of the coupling between complex metal-organic dyes and the surface. The relatively large anchoring group is needed because the dye is attached to the surface via two carboxylic groups, and not because of the presence of the metal atom in the metal-organic dye. The good agreement of the injection times calculated using the full adsorbed dye and the biisonicotinic acid anchoring group shows that it is not necessary to include a metal centre in the anchoring group model. Therefore, the partitioning scheme with the same

anchoring group (biisonicotinic acid) can be used to calculate electron transfer properties of many different metal-organic dyes, both ruthenium-based and containing other metal centres, such as Cu and Fe.[39]

5.5 Conclusions

In this chapter, we studied adsorption and electron injection from the metal–organic N3 dye to the TiO_2 rutile (110) surface. Our systematic investigation of all possible adsorption configurations on this surface suggests that there are many adsorption configurations with similar energies which may exist, co-exist or convert into one another. The structures with two or three adsorbed carboxylic groups are likely to form, and are additionally stabilized by the sulphur atom of the thiocyanate group interacting with the surface (in agreement with core-level photoemission spectroscopy experiments). The energy gain due to these groups binding to the surface is counterbalanced by the energy cost of deforming the molecule, giving the final adsorption energies usually in a range from −1.1 to −0.6 eV. Many of the low-energy configurations have very similar fast electron injection times. Thus, fast electron injection observed in experiments can equally likely originate from several co-existing structures or from one preferred structure. Therefore, there is no need to control the adsorption configuration of N3 and related dyes to improve their electron injection properties.

We can expect that the rate of electron back transfer from TiO_2 to the oxidized dye, which is also dependent on the dye–surface coupling, will also be similar for the different adsorption configurations; however, different adsorption configurations may

lead to a difference in the interaction of the dye cation with the redox species, therefore it may be necessary to control the dye's adsorption configuration (by modifying functional groups attached to the dye's ligands), to achieve favourable interaction of the dye cation with the redox species and thus facilitate the regeneration of the dye cation. However, this is beyond the scope of this thesis.

This study also sets the foundation for studies of electron injection properties of other metal–organic dyes. We show that injection times of the N3 dye can be reliably predicted using a computationally efficient partitioning procedure. This opens a possibility to quickly calculate injection times for many other metal-organic dyes with different structures and to draw conclusions on electron transfer properties of metal-organic dyes.

Chapter 6:

A model configuration interaction Hamiltonian for the study of the multi-excitonic states in singlet fission

Abstract

In this chapter we develop a model configuration interaction Hamiltonian in order to study the electronic structure of a chain of molecules undergoing singlet fission. We first consider a model for a dimer with tunable inter-monomer distance, introducing a parameterization of matrix elements, in order to mimic physical properties of organic crystalline materials. We show that the ME state is stabilized at short inter-monomer distance and the extent of this stabilization depends upon the size of overlap dependent matrix elements. We then extend our study to a linear trimer, where we observe that two types of ME states arise: bound ME states which are stabilized if compared to the energy of two separate triplets, and unbound ME states whose stabilization is negligible. We hence propose simple design rules in order to build Hamiltonians for chains of N monomers, from the matrix elements of the trimer Hamiltonian. This study provides a powerful tool for the study of singlet fission and in particular for the calculation of the S1←ME transition rates, that will discussed in Chapter 7.

6.1 Introduction

As reported in Chapter 1, SF has been theoretically studied through different methods (*ab initio* calculations,[28-31] non adiabatic molecular dynamics[27], phenomenological models[22-26]). However most of these studies are generally limited only to a dimer system, which is not enough to describe a process taking place in a crystalline material. In particular *ab initio* calculations were employed to compute the electronic structures of pentacene and tetracene dimers, in order to investigate the energetic levels of ME, S and CT states;[28-30] high level methods (i.e. CAS-SCF) are impossible to apply to larger systems, even for a minimal choice of the active space. Moreover, they would give results valid only for a particular choice of the system under study, thus not allowing to draw more general conclusions. CDFT-CI method has also been used to study energy differences and coupling between states involved in SF. SF rates were computed adopting Jortner and Bixon theory,[133-135] obtaining results in agreement with experimental findings.[31] Nevertheless, these calculations were still performed on dimers extracted from crystallographic structures, hence they cannot fully represent the physics of the system and the mechanism of SF. Phenomenological models have also been considered but they usually feature only a minimal Hamiltonian of the system, neglecting the vast majority of double excited configurations. Moreover, energies of the excited configurations of interests are still acquired from *ab initio* calculations of dimers.[22-26] Again this limits the applicability and the generality of these methods, and prevents them from going beyond the dimer picture, which is incapable of capturing the whole physics of the SF process in crystalline organic materials.

For these reasons, we choose to approach our study on SF, by computing the electronic structure of a chain of molecules undergoing to SF, through a generic model Hamiltonian. In particular, we start by constructing a CI Hamiltonian for a dimer, containing all the singles and doubles excitations, obtaining a more accurate description of the electronic structure. We adopt CI, which is the only feasible method and it is also conceptually simple, in order to build a generic model.[138] The parameters used to express the matrix elements can be changed to mimic physical properties of different molecules, thus granting versatility to the model, which do not depend on any *ab initio* calculation. The CI model is then extended to the study of a linear trimer chain, showing that two types of ME arise for $N > 2$: bound ME states (MEb), possessing a stabilization energy, and unbound ME states (MEu). We then extend our study to the electronic structure of a generic chain of N molecules undergoing to SF, thus paving the way for the study of the non radiative decay from a S_1 state to a manifold of MEb and MEu states, a topic that will be covered in Chapter 7.

6.2 CI model for singlet fission in a dimer

The starting point of our study of SF is a simple system of two sites (monomers), each possessing two orbitals a^1, r^1 on site 1 and a^2, r^2 on site 2 (a^1/a^2 orbitals (HOMO) and r^1/r^2 orbitals (LUMO) are degenerate). The two monomers are separated by a distance d, which is a tunable parameter. In this "dimer" model, at the ground state a^1 and a^2 orbitals are fully occupied. We choose to describe the electronic structure of this model system using CI theory, where the expansion of the CI wave function is truncated to

doubles configurations (SDCI). For a generic cluster of N monomers the wave function is given by:

$$\Phi = c_0|0\rangle + \sum_{ij}^{N} c_j^i \,|\,{}^{j}_{i}\rangle + \sum_{\substack{i<k \\ j<l}}^{N} c_{ik}^{jl}\,|\,{}^{jl}_{ik}\rangle \tag{6.1}$$

All the possible singlet singles and doubles excited configurations for this system are depicted in **Figure 6.1**. We introduced a simplified notation (respect to the one used in Chapter 2) for the excited configurations: for single excitations, the notation $|\,{}^{j}_{i}\rangle$ indicates a single excited configurations from the HOMO orbital of the i-th monomer to the LUMO orbital of the j-th monomer while $|\,{}^{jl}_{ik}\rangle$ indicates a double excited configurations from the HOMO orbital of monomers i and k to the LUMO orbitals of monomers j and l.

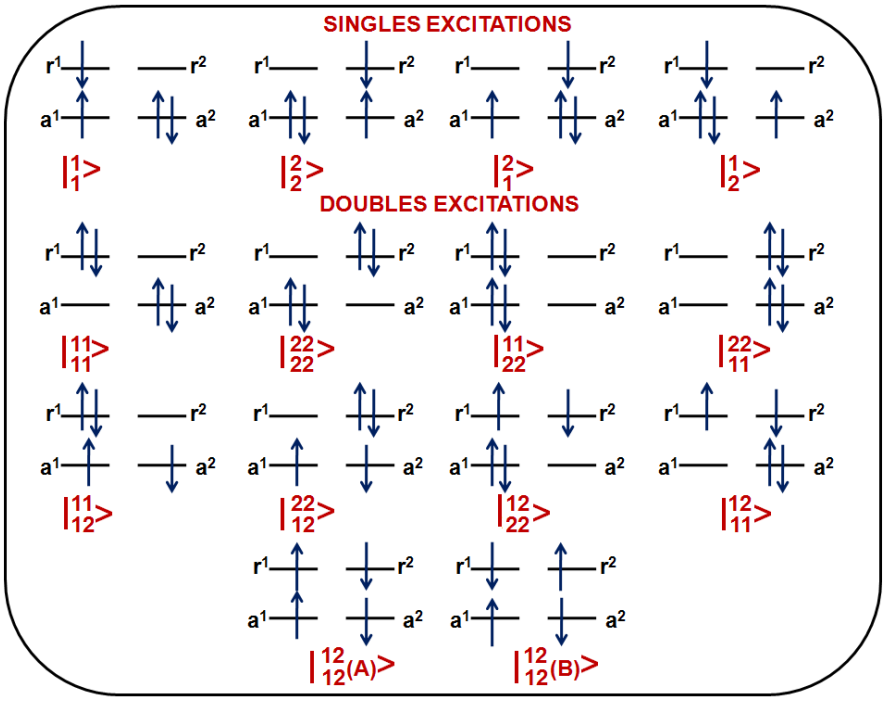

Figure 6.1: Schematic representation of singlet excited configurations for a dimer model.

H_{CI} for the dimer system has been obtained modifying the basis functions and the matrix elements, from Ref.[227] and the energy of the ground state is set to zero. The following list of equations represents the full set of matrix elements of H_{CI} for the dimer model.

$$\left\langle {}^{1}_{1}\middle|H_{\mathrm{CI}}\middle|{}^{1}_{1}\right\rangle = \left\langle {}^{2}_{2}\middle|H_{\mathrm{CI}}\middle|{}^{2}_{2}\right\rangle = \varepsilon_{\mathrm{r}} - \varepsilon_{\mathrm{a}} - J_{\mathrm{r}^1\mathrm{a}^1} + 2K_{\mathrm{r}^1\mathrm{a}^1} \tag{6.2}$$

$$\left\langle {}^{2}_{1}\middle|H_{\mathrm{CI}}\middle|{}^{2}_{1}\right\rangle = \left\langle {}^{1}_{2}\middle|H_{\mathrm{CI}}\middle|{}^{1}_{2}\right\rangle = \varepsilon_{\mathrm{r}} - \varepsilon_{\mathrm{a}} - J_{\mathrm{r}^1\mathrm{a}^2} \tag{6.3}$$

$$\left\langle {}^{11}_{11}\middle|H_{\mathrm{CI}}\middle|{}^{11}_{11}\right\rangle = \left\langle {}^{22}_{22}\middle|H_{\mathrm{CI}}\middle|{}^{22}_{22}\right\rangle = 2(\varepsilon_{\mathrm{r}} - \varepsilon_{\mathrm{a}}) - 4J_{\mathrm{r}^1\mathrm{a}^1} + J_{\mathrm{r}^1\mathrm{r}^1} + J_{\mathrm{a}^1\mathrm{a}^1} + 2K_{\mathrm{r}^1\mathrm{a}^1} \tag{6.4}$$

$$\left\langle {}^{22}_{11}\middle|H_{\mathrm{CI}}\middle|{}^{22}_{11}\right\rangle = \left\langle {}^{11}_{22}\middle|H_{\mathrm{CI}}\middle|{}^{22}_{11}\right\rangle = 2(\varepsilon_{\mathrm{r}} - \varepsilon_{\mathrm{a}}) - 4J_{\mathrm{r}^1\mathrm{a}^2} + J_{\mathrm{r}^1\mathrm{r}^1} + J_{\mathrm{a}^1\mathrm{a}^1} \tag{6.5}$$

$$\left\langle {}^{11}_{12}\middle|H_{\mathrm{CI}}\middle|{}^{11}_{12}\right\rangle = \left\langle {}^{22}_{12}\middle|H_{\mathrm{CI}}\middle|{}^{22}_{12}\right\rangle = $$

$$= 2(\varepsilon_{\mathrm{r}} - \varepsilon_{\mathrm{a}}) + K_{\mathrm{r}^1\mathrm{a}^1} - 2J_{\mathrm{r}^1\mathrm{a}^1} + J_{\mathrm{r}^1\mathrm{r}^1} - 2J_{\mathrm{r}^1\mathrm{a}^2} + J_{\mathrm{a}^1\mathrm{a}^2} \tag{6.6}$$

$$\left\langle {}^{12}_{11}\middle|H_{\mathrm{CI}}\middle|{}^{12}_{11}\right\rangle = \left\langle {}^{12}_{22}\middle|H_{\mathrm{CI}}\middle|{}^{12}_{22}\right\rangle = $$

$$= 2(\varepsilon_{\mathrm{r}} - \varepsilon_{\mathrm{a}}) + K_{\mathrm{r}^1\mathrm{a}^1} - 2J_{\mathrm{r}^1\mathrm{a}^1} + J_{\mathrm{a}^1\mathrm{a}^1} - 2J_{\mathrm{r}^1\mathrm{a}^2} + J_{\mathrm{r}^1\mathrm{r}^2} \tag{6.7}$$

$$\left\langle {}^{12}_{12}(\mathrm{A})\middle|H_{\mathrm{CI}}\middle|{}^{12}_{12}(\mathrm{A})\right\rangle = 2(\varepsilon_{\mathrm{r}} - \varepsilon_{\mathrm{a}}) - 2J_{\mathrm{r}^1\mathrm{a}^1} \tag{6.8}$$

$$\left\langle {}^{12}_{12}(\mathrm{B})\middle|H_{\mathrm{CI}}\middle|{}^{12}_{12}(\mathrm{B})\right\rangle = 2(\varepsilon_{\mathrm{r}} - \varepsilon_{\mathrm{a}}) - 2J_{\mathrm{r}^1\mathrm{a}^1} + 4K_{\mathrm{r}^1\mathrm{a}^1} \tag{6.9}$$

$$\left\langle 0\middle|H_{\mathrm{CI}}\middle|{}^{2}_{1}\right\rangle = \left\langle 0\middle|H_{\mathrm{CI}}\middle|{}^{1}_{2}\right\rangle = F_{\mathrm{r}^1\mathrm{a}^2} \tag{6.10}$$

$$\left\langle 0\middle|H_{\mathrm{CI}}\middle|{}^{11}_{11}\right\rangle = \left\langle 0\middle|H_{\mathrm{CI}}\middle|{}^{22}_{22}\right\rangle = K_{\mathrm{r}^1\mathrm{a}^1} \tag{6.11}$$

$$\left\langle 0\middle|H_{\mathrm{CI}}\middle|{}^{12}_{12}(\mathrm{B})\right\rangle = -\sqrt{3}(\mathrm{r}^1\mathrm{a}^1|\mathrm{r}^2\mathrm{a}^2) \tag{6.12}$$

$$\left\langle {}^{1}_{1}\middle|H_{\mathrm{CI}}\middle|{}^{2}_{2}\right\rangle = 2(\mathrm{r}^1\mathrm{a}^1|\mathrm{r}^2\mathrm{a}^2) \tag{6.13}$$

$$\left\langle {}^{1}_{1}\middle|H_{\mathrm{CI}}\middle|{}^{2}_{1}\right\rangle = \left\langle {}^{2}_{2}\middle|H_{\mathrm{CI}}\middle|{}^{1}_{2}\right\rangle = F_{\mathrm{r}^1\mathrm{r}^2} \tag{6.14}$$

$$\left\langle {}^{1}_{1}\middle|H_{\mathrm{CI}}\middle|{}^{1}_{2}\right\rangle = \left\langle {}^{2}_{2}\middle|H_{\mathrm{CI}}\middle|{}^{2}_{1}\right\rangle = -F_{\mathrm{a}^1\mathrm{a}^2} \tag{6.15}$$

$$\left\langle {}^{1}_{1}\middle|H_{\mathrm{CI}}\middle|{}^{11}_{12}\right\rangle = \left\langle {}^{2}_{2}\middle|H_{\mathrm{CI}}\middle|{}^{22}_{12}\right\rangle = -F_{\mathrm{r}^1\mathrm{a}^2} \tag{6.16}$$

$$\left\langle {}^{1}_{1}\middle|H_{\mathrm{CI}}\middle|{}^{12}_{11}\right\rangle = \left\langle {}^{2}_{2}\middle|H_{\mathrm{CI}}\middle|{}^{12}_{22}\right\rangle = F_{\mathrm{r}^1\mathrm{a}^2} \tag{6.17}$$

$$\left\langle {}^{2}_{1}\middle|H_{\mathrm{CI}}\middle|{}^{22}_{11}\right\rangle = \left\langle {}^{1}_{2}\middle|H_{\mathrm{CI}}\middle|{}^{11}_{22}\right\rangle = \sqrt{2}F_{\mathrm{r}^1\mathrm{a}^2} \tag{6.18}$$

$$\left\langle {}^{2}_{1}\middle|H_{\mathrm{CI}}\middle|{}^{12}_{12}(\mathrm{A})\right\rangle = \left\langle {}^{1}_{2}\middle|H_{\mathrm{CI}}\middle|{}^{12}_{12}(\mathrm{A})\right\rangle = -\sqrt{3/2}F_{\mathrm{r}^1\mathrm{a}^2} \tag{6.19}$$

$$\left\langle {}^{11}_{11}\middle|H_{\mathrm{CI}}\middle|{}^{11}_{12}\right\rangle = \left\langle {}^{22}_{22}\middle|H_{\mathrm{CI}}\middle|{}^{22}_{12}\right\rangle = \sqrt{2}F_{\mathrm{a}^1\mathrm{a}^2} \tag{6.20}$$

$$\left\langle {}^{11}_{11}\middle|H_{\mathrm{CI}}\middle|{}^{12}_{11}\right\rangle = \left\langle {}^{22}_{22}\middle|H_{\mathrm{CI}}\middle|{}^{12}_{22}\right\rangle = \sqrt{2}F_{\mathrm{r}^1\mathrm{r}^2} \tag{6.21}$$

$$\left\langle {}^{12}_{11}\middle|H_{\mathrm{CI}}\middle|{}^{22}_{12}\right\rangle = \left\langle {}^{12}_{22}\middle|H_{\mathrm{CI}}\middle|{}^{12}_{11}\right\rangle = -(\mathrm{r}^1\mathrm{a}^1|\mathrm{r}^2\mathrm{a}^2) \tag{6.22}$$

$$\left\langle {}^{11}_{12}\middle|H_{\mathrm{CI}}\middle|{}^{12}_{12}(\mathrm{A})\right\rangle = \left\langle {}^{22}_{12}\middle|H_{\mathrm{CI}}\middle|{}^{12}_{12}(\mathrm{A})\right\rangle = \sqrt{2}F_{\mathrm{a}^1\mathrm{a}^2} \tag{6.23}$$

$$\left\langle {}^{12}_{11}\middle|H_{\mathrm{CI}}\middle|{}^{12}_{12}(\mathrm{A})\right\rangle = \left\langle {}^{12}_{22}\middle|H_{\mathrm{CI}}\middle|{}^{12}_{12}(\mathrm{A})\right\rangle = \sqrt{2}F_{\mathrm{r}^1\mathrm{r}^2} \tag{6.24}$$

Where the notation (ab|cd) denotes the following two-electron integral:

$$(ab|cd) = \iint \psi_a\,(x_1)\psi_b\,(x_2)\frac{1}{x_{12}}\psi_c\,(x_1)\psi_d\,(x_2)dx_1dx_2 \tag{6.25}$$

In **Table 6.1** we list the parameters used for computing the matrix elements for the CI matrix. In particular, we choose two sets of parameters: a tetracene-like (T) set of parameters and pentacene-like (P) one. Some of these parameters are constant, hence, they do not depend on the inter-monomer distance d. These parameters are:

(i) the orbital energies ε_{r} and ε_{a} whose values have been reported from available literature;[228, 229]

(ii) intra-monomer coulomb integrals ($J_{\mathrm{r^i a^i}}$, $J_{\mathrm{r^i r^i}}$, $J_{\mathrm{a^i a^i}}$) represent Coulombic repulsion between two electrons which is expressed by the following bi-electronic integral (i.e. for $J_{\mathrm{r^i a^i}}$) :

$$J_{\mathrm{r^i a^i}} = \left(\mathrm{r^i r^i}\middle|\mathrm{a^i a^i}\right) = \iint \psi_{r^i}^2(x_1)\frac{1}{x_{12}}\psi_{a^i}^2(x_2)dx_1dx_2 \tag{6.26}$$

where x_{12} is the distance between the two electrons. The equation shows also why these elements do not depend on *d*, since Eq. 6.26 involves coulombic repulsion of electrons on the same i-th site. We assume that all the integrals of this type ($J_{\mathrm{r^i a^i}}$, $J_{\mathrm{r^i r^i}}$, $J_{\mathrm{a^i a^i}}$) are equal to a common constant J. In particular the computed value is $J_{\mathrm{r^i a^i}}$, computed from Eq. 6.2, for tetracene and pentacene.

(iii) The exchange integral $K_{\mathrm{r^i a^i}}$, is defined as:

$$K_{\mathrm{r^i a^i}} = \left(\mathrm{r^i a^i}\middle|\mathrm{a^i r^i}\right) = -\iint \psi_{r^i}(x_1)\psi_{a^i}(x_2)\frac{1}{x_{12}}\psi_{a^i}(x_1)\psi_{r^i}(x_2)dx_1dx_2 \tag{6.27}$$

The exchange integral is a quantum mechanical construct, based on the Pauli exclusion principle. It takes into account the effect of the antisymmetry of the electron wavefunctions.

For this parameter, values are taken from available literature as the energy difference between S_1 and T_1.[17] In fact, the energy of a triplet single excitation for a dimer SDCI Hamiltonian of triplet excitations ($H_{\mathrm{CI}}^{\mathrm{T}}$) is given by Eq. 6.28. It differs from Eq. 6.2 for twice $K_{\mathrm{r^1a^1}}$.

$$\left\langle \begin{matrix} 1 \\ 1 \end{matrix} \middle| H_{\mathrm{CI}}^{\mathrm{T}} \middle| \begin{matrix} 1 \\ 1 \end{matrix} \right\rangle = \varepsilon_{\mathrm{r}} - \varepsilon_{\mathrm{a}} - J_{\mathrm{r^1a^1}} \tag{6.28}$$

$K_{\mathrm{r^ia^i}}$ is the only element of its type. Therefore, for the sake of simplicity, we impose $K = K_{\mathrm{r^ia^i}}$.

The other terms depend on d and their $f(d)$ behaviour is also described in **Table 6.1**. We include:

(i) inter-monomer coulomb integrals ($J_{\mathrm{r^ia^j}}$, $J_{\mathrm{r^ja^i}}$, $J_{\mathrm{r^ir^j}}$, $J_{\mathrm{a^ia^j}}$) whose d-dependent behaviour is described by Coulomb's law. They represent the electronic repulsion for two electrons on different sites:

$$J_{\mathrm{r^ia^j}} = \iint \psi_{r^i}^2(x_1)\frac{1}{x_{12}}\psi_{a^j}^2(x_2)dx_1dx_2 \tag{6.29}$$

where, here, x_{12}, the distance between the two electrons, contains the d parameter, since the electrons are located on different sites. We assume that all the integrals of this type follow the same distance dependent behavior, described in **Table 6.1** as J'.

(ii) $V_{ex} = (\mathrm{r^i a^i | r^j a^j})$ is called the excitonic coupling and for a dimer is typically measured as one half of the splitting of the Frenkel excitonic states (see Eq. 6.13). It represents an interaction energy due to exchange of excitation energy between two excitations, on two different molecules i and j. In exciton theory, it is described by the interaction between two point dipoles separated by d.[230]

(iii) Fock matrix elements ($F_{\mathrm{r^i a^j}}$, $F_{\mathrm{r^j a^i}}$, $F_{\mathrm{r^i r^j}}, F_{\mathrm{a^i a^j}}$) decrease exponentially with increasing distance *d*. We assume that all the elements of this type show the same distance dependent behavior and, hence, we group them as F'. Reasonable values for F' for tetracene and pentacene pairs in the crystalline structure are reported in Ref.[231].

Table 6.1: List of parameters, their values (eV) and inter-monomer distance dependent behaviour; $\boldsymbol{l}$ is an approximate measure of the size of the electronic cloud of tetracene and pentacene, given by the length of the molecule. For distance dependent parameters, the value in table refers to $d_0 = 4$ Å, which is the minimum considered distance.

Parameters	Value (eV)	Distance dependent behavior
$\varepsilon_{\mathrm{r}} - \varepsilon_{\mathrm{a}}$ (Ref.[228, 229])	5.9 (T), 5.2 (P)	//
J	4.75 (T), 4.33 (P)	//
K (Ref.[17])	0.55 (T), 0.72 (P)	//
J'	1.37 (T), 1.14 (P)	$J' = \frac{1}{4\pi\varepsilon_0} \times \frac{e^2}{\sqrt{(d^2 + l^2)}}$
V_{ex}^0 (Ref.[230])	0.15 (T,P)	$V_{ex} = V_{ex}^0 \left(\frac{d_0^3}{d^3}\right)$
F'	0.15 (T,P)	//

Among the matrix elements, we underline that there are two different $|\begin{smallmatrix}12\\12\end{smallmatrix}\rangle$ excited state configurations, labeled as A and B. They differ because, as shown in **Figure 6.1**, $|\begin{smallmatrix}12\\12\end{smallmatrix}(\mathrm{A})\rangle$ is constituted by two triplets excited configurations (one on each site) with

opposite spin, thus granting an overall singlet nature to the configuration. On the other side, $|{}^{12}_{12}(\mathrm{B})\rangle$ can be viewed as composed by a single singlet excitation on each site. This is reflected also in the matrix elements reported in Eq. 6.8 and Eq. 6.9, as their energy difference is equal to twice the energy difference between a single singlet and a single triplet excited configuration.

6.3 CI dimer model: results

The main results obtained by the SDCI treatment of the dimer model, in a range of d between 4 and 100 Å, for P and T choice of parameters are depicted in **Figure 6.2**.

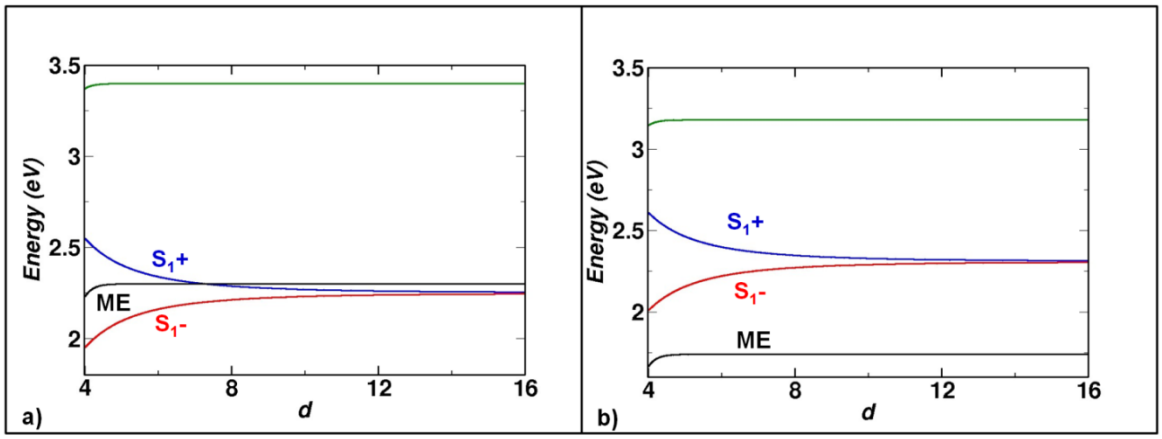

Figure 6.2: Eigenvalues for the states of interest as function of $\boldsymbol{d}$ for the T (panel a) and P (panel b) scenarios, respectively. Nearest state to the states of interest shown by green curve.

We notice, for both T and P, the splitting of the two singlets deriving from V_{ex}, leading to the formation of two mixed states that we call S_1+ and S_1-. They both derive from mixing of $|{}^{1}_{1}\rangle$ and $|{}^{2}_{2}\rangle$, which are coupled both directly through V_{ex} and indirectly through CT determinants ($|{}^{2}_{1}\rangle$, $|{}^{1}_{2}\rangle$). We define S_1- the lowest energy singlet excited state and S_1+ the other. The ME state is defined as the state dominated by the $|{}^{12}_{12}(\mathrm{A})\rangle$

configuration. The ME state is stabilized, if compared to the matrix element associated to $|{}^{12}_{12}(\mathrm{A})\rangle$ (which is equal to the energy of two separated triplet excited configurations), by the Fock elements which arise from the coupling of $|{}^{12}_{12}(\mathrm{A})\rangle$ with singles and doubles charge transfer (CT) determinants ($|{}^{2}_{1}\rangle$, $|{}^{1}_{2}\rangle$, $|{}^{21}_{11}\rangle$, $|{}^{12}_{22}\rangle$, $|{}^{11}_{12}\rangle$, $|{}^{22}_{12}\rangle$) at short distance.

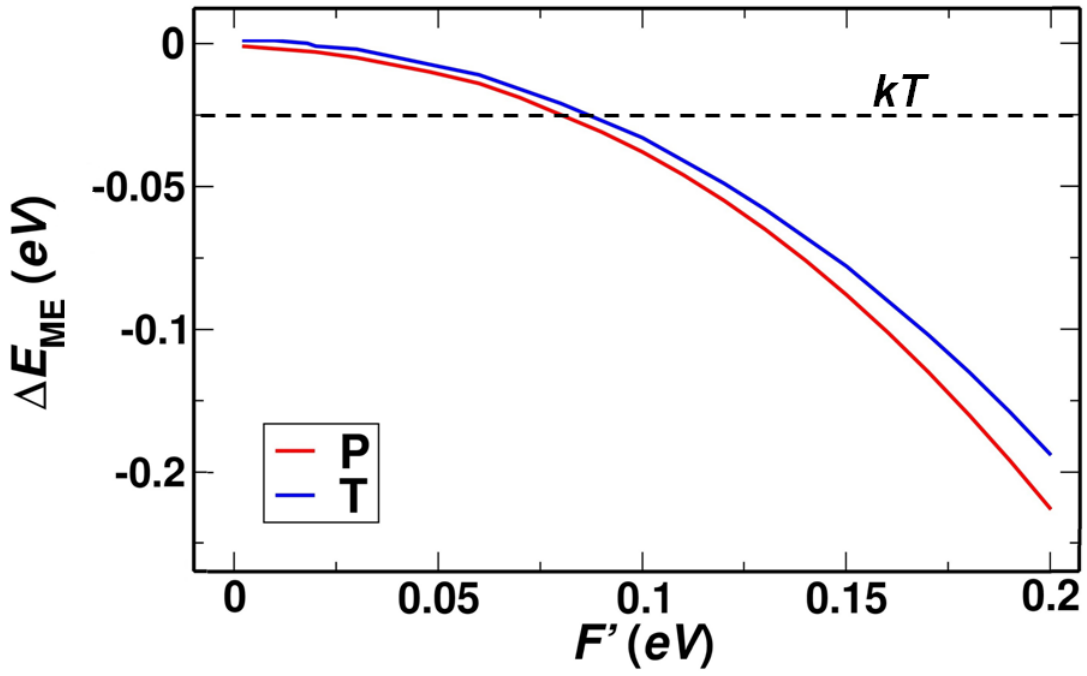

Figure 6.3: ME binding energy as function of F', for both P and T sets of parameters. Values of J' and V_{ex} are fixed.

Having noticed that the ME state is stabilized at lower inter-monomer distance, it is useful to consider under what condition the stabilization is larger than kT at room temperature. This may be relevant if one is interested in the case where the two monomers are free to move at any distance from each other, like in solution. The importance of the size of the F' elements for the stabilization of ME is highlighted in **Figure 6.3** where we compute this stabilization as the difference between the energy of

ME state at distance infinity (which is equal to twice the energy of the first triplet T_1) and its energy at increasing values of F', having fixed the other distance dependent parameters to their maximum value.

$$\Delta E_{\mathrm{ME}}(d) = E_{\mathrm{ME}}(d) - 2E_{\mathrm{T_1}} \tag{6.30}$$

Figure 6.3 shows that, for $F' > 0.1$ eV, the stabilization of the ME state is sensibly higher than kT, and, hence, ME states are energetically distinguishable from two separated triplets, in a wide range of F'.

6.4 CI model for singlet fission in linear trimer: bound and unbound multi-exciton states

As good as a starting point it might be, a dimer model is not capable of capturing the whole physics of a process taking place in a crystalline solid like pentacene or tetracene. If just a trimer model is considered instead of the dimer one, there will be new configurations appearing; in particular the two pseudo-triplets can be located on neighboring sites ($|\,{}^{12}_{12}\rangle$, $|\,{}^{23}_{23}\rangle$) as in the dimer case (we simplify the notation for these double excitations, since for the rest of the thesis we will only consider A-type configurations), but there is also a configuration where the two pseudo-triplets are separated: $|\,{}^{13}_{13}\rangle$. Moreover, these different configurations couple among each other both directly through a $(a^i a^j|r^i r^j)$ matrix element and indirectly through new ME-CT states appearing in the system (see **Figure 6.4**). The direct coupling is due to a $(a^i a^j|r^i r^j)$ matrix element (this is the matrix element that couples two different triplets) through the following expressions:

$$\left\langle \begin{matrix} 12 \\ 12 \end{matrix} \middle| H_{\mathrm{CI}} \middle| \begin{matrix} 13 \\ 13 \end{matrix} \right\rangle = -(\mathrm{a}^2\mathrm{a}^3|\mathrm{r}^2\mathrm{r}^3) \tag{6.31}$$

$$\left\langle \begin{matrix} 13 \\ 13 \end{matrix} \middle| H_{\mathrm{CI}} \middle| \begin{matrix} 23 \\ 23 \end{matrix} \right\rangle = -(\mathrm{a}^1\mathrm{a}^2|\mathrm{r}^1\mathrm{r}^2) \tag{6.32}$$

$$\left\langle \begin{matrix} 12 \\ 12 \end{matrix} \middle| H_{\mathrm{CI}} \middle| \begin{matrix} 23 \\ 23 \end{matrix} \right\rangle = -(\mathrm{a}^1\mathrm{a}^3|\mathrm{r}^1\mathrm{r}^3) \sim 0 \tag{6.33}$$

Where $(\mathrm{a}^1\mathrm{a}^3|\mathrm{r}^1\mathrm{r}^3)\sim 0$, since the matrix element is overlap dependent and, therefore, it will decay exponentially outside the overlap region, as in the case where are involved non-adjacent sites.

The indirect coupling is mediated by ME-type CT configurations:

$$\left\langle \begin{matrix} 23 \\ 13 \end{matrix} \middle| H_{\mathrm{CI}} \middle| \begin{matrix} 23 \\ 23 \end{matrix} \right\rangle = \left\langle \begin{matrix} 13 \\ 23 \end{matrix} \middle| H_{\mathrm{CI}} \middle| \begin{matrix} 13 \\ 13 \end{matrix} \right\rangle = -F_{\mathrm{a}^1\mathrm{a}^2} \tag{6.34}$$

$$\left\langle \begin{matrix} 13 \\ 12 \end{matrix} \middle| H_{\mathrm{CI}} \middle| \begin{matrix} 11 \\ 12 \end{matrix} \right\rangle = \left\langle \begin{matrix} 12 \\ 13 \end{matrix} \middle| H_{\mathrm{CI}} \middle| \begin{matrix} 13 \\ 13 \end{matrix} \right\rangle = -F_{\mathrm{a}^2\mathrm{a}^3} \tag{6.35}$$

$$\left\langle \begin{matrix} 23 \\ 13 \end{matrix} \middle| H_{\mathrm{CI}} \middle| \begin{matrix} 13 \\ 13 \end{matrix} \right\rangle = \left\langle \begin{matrix} 13 \\ 23 \end{matrix} \middle| H_{\mathrm{CI}} \middle| \begin{matrix} 23 \\ 23 \end{matrix} \right\rangle = F_{\mathrm{r}^1\mathrm{r}^2} \tag{6.36}$$

$$\left\langle \begin{matrix} 13 \\ 12 \end{matrix} \middle| H_{\mathrm{CI}} \middle| \begin{matrix} 13 \\ 13 \end{matrix} \right\rangle = \left\langle \begin{matrix} 13 \\ 12 \end{matrix} \middle| H_{\mathrm{CI}} \middle| \begin{matrix} 12 \\ 12 \end{matrix} \right\rangle = -F_{\mathrm{r}^2\mathrm{r}^3} \tag{6.37}$$

$$\left\langle \begin{matrix} 23 \\ 12 \end{matrix} \middle| H_{\mathrm{CI}} \middle| \begin{matrix} 23 \\ 23 \end{matrix} \right\rangle = \left\langle \begin{matrix} 12 \\ 23 \end{matrix} \middle| H_{\mathrm{CI}} \middle| \begin{matrix} 12 \\ 12 \end{matrix} \right\rangle = -F_{\mathrm{a}^1\mathrm{a}^3} \sim 0 \tag{6.38}$$

$$\left\langle \begin{matrix} 23 \\ 12 \end{matrix} \middle| H_{\mathrm{CI}} \middle| \begin{matrix} 12 \\ 12 \end{matrix} \right\rangle = \left\langle \begin{matrix} 12 \\ 23 \end{matrix} \middle| H_{\mathrm{CI}} \middle| \begin{matrix} 23 \\ 23 \end{matrix} \right\rangle = -F_{\mathrm{a}^1\mathrm{a}^3} \sim 0 \tag{6.39}$$

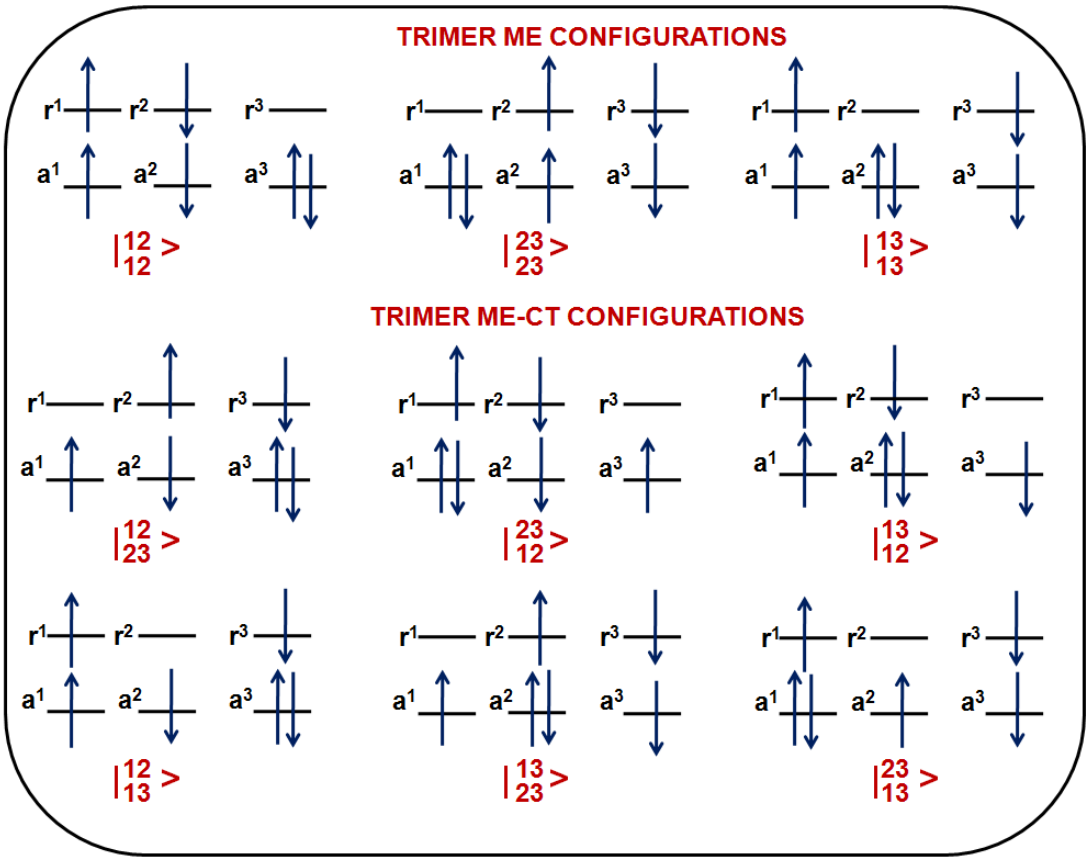

Figure 6.4: Schematic representation of configurations of interest for the trimer case.

The $(a^i a^j | r^i r^j)$ element is roughly estimated as one half of the splitting of the first triplet (T_1) in a dimer. In fact, the matrix element between two single triplet excitations in a dimer SDCI Hamiltonian of triplet excitations (H_{CI}^{T}) is given by[227]:

$$\left\langle \begin{matrix} 1 \\ 1 \end{matrix} \middle| H_{CI}^{T} \middle| \begin{matrix} 2 \\ 2 \end{matrix} \right\rangle = (a^1 a^2 | r^1 r^2) \tag{6.40}$$

From TD-DFT calculations at the B3LYP/6-31G* level of theory we obtain values from 0.006 eV to 0.015 eV for pentacene and from 0.002 eV to 0.05 eV for tetracene. In fact we have to consider that unit cells of organic crystals such as tetracene and pentacene present different possible "geometric couples" of molecules and the matrix element is therefore different for each chosen couple of molecules[231].

We diagonalize the SDCI Hamiltonian for the trimer case, for both T and P scenarios, considering an inter-monomer distance of 4 Å. $(a^i a^j | r^i r^j)$ element is set to the maximum value obtained from TD-DFT calculations for pentacene and tetracene respectively, and the other d-dependent elements are set to their maximum value at 4 Å (see **Table 6.1**). The energies of the states of interest for P and T scenarios are shown in **Figure 6.5**. The nearest state to the state of interest is a CT state whose energy is ~3.4 eV and it is not included in the figure.

The most interesting thing that is noticeable in the transition from the dimer to the trimer model is that there are multiple ME states and they are not at the same energy level. In particular we can divide the ME states in two sets: a first set at lower energy which is composed by linear combinations of $|{}^{12}_{12}\rangle$ and $|{}^{23}_{23}\rangle$: two states which are almost degenerate (bound states: MEb); a second set is composed by a single state (unbound state: MEu) dominated by the contribution of $|{}^{13}_{13}\rangle$ configuration and it is approximately 0.1 eV higher in energy than MEb states, for both tetracene-like and pentacene-like scenarios. Therefore, the relative position of the two pseudo-triplets of the ME state is fundamental: bound ME on neighbor sites are different from unbound ME where the two pseudo-triplets are far apart.

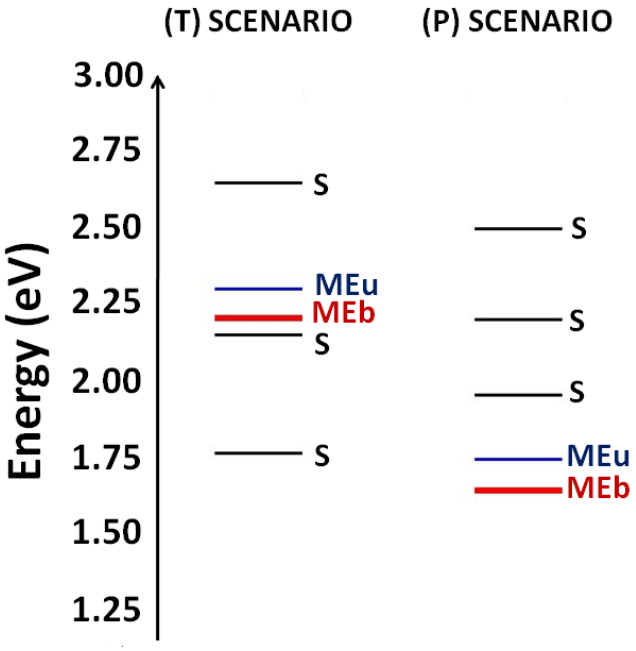

Figure 6.5: Representation of the energy levels for the states of interest in the trimer model, for T and P scenarios, respectively.

This helps the analysis of a chain constituted by N monomers and the study of the internal conversion that produces ME states from the S state. In fact, unbound ME states have negligible binding energy and, since the pseudo-triplet are far apart from each other, they can be considered as separated triplets. On the other hand, bound ME states do have binding energy and therefore the two pseudo-triplets are not independent, thus possibly affecting the singlet fission efficiency, since they will show a longer life-time.

6.5 Matrix partitioning method: from trimer model to N-mer

The number of double configurations that should be included for clusters with a larger number of molecules increases rapidly (approximately as N^4), hence for $N > 3$ it is not convenient to build H_{CI} as we did for dimer and trimer case. In principle, we would like to obtain an Hamiltonian for a chain of N monomers, containing only the N Frenkel-type excitons and the $N(N-1)/2$ ME states. This is possible, adopting the matrix

partitioning scheme. For the trimer model we can use matrix partitioning scheme to obtain an effective Hamiltonian containing only Frenkel excitons and ME matrix elements. Other configurations can be partitioned out since they are well separated in energy and they are not much mixed. We do not simply neglect them because they can mediate the coupling between the configurations of interest. Therefore the SDCI Hamiltonian for the trimer model can be written in the following form (see Chapter 2 for details of the matrix partitioning procedure):

$$[H_{\mathrm{CI}}^{eff}]_{aa} = [H_{\mathrm{CI}}]_{aa} + [H_{\mathrm{CI}}]_{ab}(1E' - [H_{\mathrm{CI}}]_{bb})^{-1}[H_{\mathrm{CI}}]_{ba} \tag{6.41}$$

where $[H_{CI}]_{aa}$ is the block of H_{CI} the configurations of interest (the three configurations leading to singlets S_1, S_2, S_3 and the three configurations leading to ME states: MEb1, MEb2 and MEu). $[H_{CI}]_{bb}$ is the block containing the matrix elements of all the other configurations. $[H_{CI}]_{ab}$ and $[H_{CI}]_{ba}$ contain all the coupling elements of the configurations of interest with all the other states. Finally, E' is a parameter which is chosen as the average of the eigenvalues of the states of interest from previous diagonalization of H_{CI}.Therefore $H_{\mathrm{CI}-eff}$ is an effective Hamiltonian for the trimer model, including only the configurations of interest and the effective coupling due to the interaction among themselves and with all the other configurations. For further details on the employed methodology see Chapter 2.

The final step to obtain an effective Hamiltonian for a system of N monomers is made by establishing some rules to construct it from the matrix elements of the trimer H_{CI}^{eff}. A system composed by N monomers has N singlet singles configurations. The diagonal matrix elements for the configurations from $|{}^{2}_{2}\rangle$ to $|{}^{N-1}_{N-1}\rangle$ are given by the trimer

$|{}^{2}_{2}\rangle$state while $|{}^{1}_{1}\rangle$ is given by the trimer $|{}^{1}_{1}\rangle$ and $|{}^{N}_{N}\rangle$ from trimer$|{}^{3}_{3}\rangle$. The rules for defining the coupling among the singlets configurations are the following:

(i) the effective coupling for two configurations $|{}^{i}_{i}\rangle$ and $|{}^{j}_{j}\rangle$ where $|i-j|=1$ (i.e 1 monomer distance) is given by the $\left\langle {}^{1}_{1}\right| H_{\mathrm{CI}}^{eff} \left|{}^{2}_{2}\right\rangle$ from trimer.

(ii) the effective coupling for two configurations $|{}^{i}_{i}\rangle$ and $|{}^{j}_{j}\rangle$ where $|i-j|=2$ (i.e 2 monomers distance) is given by the $\left\langle {}^{1}_{1}\right| H_{\mathrm{CI}}^{eff} \left|{}^{3}_{3}\right\rangle$ from trimer.

(iii) the coupling for two configurations $|{}^{i}_{i}\rangle$ and $|{}^{j}_{j}\rangle$ where $|i-j|>2$ is computed from the distance dependent expression for V_{ex} (see **Table 6.1**), excluding, therefore, effects due to CT states. This is reasonable at long distances.

A system of N monomers also features $[N\times(N-1)]/2$ ME configurations. Among these ME configurations, there are $N-1$ leading to MEb states and the remaining leading to MEu states. The diagonal matrix elements for these configurations are computed as follows:

(i) for MEb configurations $|{}^{ij}_{ij}\rangle$ ($|i-j|=1$) the diagonal matrix elements are taken from $|{}^{12}_{12}\rangle$ configuration;

(ii) for the MEu configurations $|{}^{ij}_{ij}\rangle$ ($|i-j|>1$) the diagonal matrix elements are taken from trimer $|{}^{13}_{13}\rangle$ configuration;

The coupling among ME configurations is determined by the following rules:

(i) the couplings among MEb configurations $|\begin{smallmatrix} ij \\ ij \end{smallmatrix}\rangle$ and $|\begin{smallmatrix} jk \\ jk \end{smallmatrix}\rangle$ are taken from the trimer $\left\langle \begin{smallmatrix} 12 \\ 12 \end{smallmatrix}\right| H_{\mathrm{CI}}^{eff} \left|\begin{smallmatrix} 23 \\ 23 \end{smallmatrix}\right\rangle$.

(ii) the coupling among the MEb states $|\begin{smallmatrix} ij \\ ij \end{smallmatrix}\rangle$ and $|\begin{smallmatrix} kl \\ kl \end{smallmatrix}\rangle$ is set to zero.

(iii) the coupling of the MEb configurations $|\begin{smallmatrix} ij \\ ij \end{smallmatrix}\rangle$ with MEu configurations $|\begin{smallmatrix} ik \\ ik \end{smallmatrix}\rangle$ is taken from trimer $\left\langle \begin{smallmatrix} 12 \\ 12 \end{smallmatrix}\right| H_{\mathrm{CI}}^{eff} \left|\begin{smallmatrix} 13 \\ 13 \end{smallmatrix}\right\rangle$ for $|j-k|=2$, hence MEb configurations only couple with MEu configurations of the same type of $|\begin{smallmatrix} 13 \\ 13 \end{smallmatrix}\rangle$.

(iv) the coupling of MEu configurations among themselves is set to $\left\langle \begin{smallmatrix} 12 \\ 12 \end{smallmatrix}\right| H_{\mathrm{CI}}^{eff} \left|\begin{smallmatrix} 13 \\ 13 \end{smallmatrix}\right\rangle$ for particular cases, explained as follow: $|\begin{smallmatrix} ij \\ ij \end{smallmatrix}\rangle$ couples with $|\begin{smallmatrix} ik \\ ik \end{smallmatrix}\rangle$ only if $|j-k|=1$. I.e $|\begin{smallmatrix} 13 \\ 13 \end{smallmatrix}\rangle$ vs $|\begin{smallmatrix} 14 \\ 14 \end{smallmatrix}\rangle$, $|\begin{smallmatrix} 14 \\ 14 \end{smallmatrix}\rangle$ vs $|\begin{smallmatrix} 15 \\ 15 \end{smallmatrix}\rangle$ and so on. These configurations couple among themselves in the same way as $|\begin{smallmatrix} 12 \\ 12 \end{smallmatrix}\rangle$ couples with $|\begin{smallmatrix} 13 \\ 13 \end{smallmatrix}\rangle$, as proven by a rapid inspection of Eq. 6.31-6.39.

Couplings among $|\begin{smallmatrix} i \\ i \end{smallmatrix}\rangle$ states and $|\begin{smallmatrix} jk \\ jk \end{smallmatrix}\rangle$ configurations are defined as follows:

(i) the coupling between $|\begin{smallmatrix} 1 \\ 1 \end{smallmatrix}\rangle$ and $|\begin{smallmatrix} 12 \\ 12 \end{smallmatrix}\rangle$ is taken from trimer $\left\langle \begin{smallmatrix} 1 \\ 1 \end{smallmatrix}\right| H_{\mathrm{CI}}^{eff} \left|\begin{smallmatrix} 12 \\ 12 \end{smallmatrix}\right\rangle$. The coupling between $|\begin{smallmatrix} N \\ N \end{smallmatrix}\rangle$ and $|\begin{smallmatrix} N-1\,N \\ N-1\,N \end{smallmatrix}\rangle$ is taken from trimer $\left\langle \begin{smallmatrix} 3 \\ 3 \end{smallmatrix}\right| H_{\mathrm{CI}}^{eff} \left|\begin{smallmatrix} 23 \\ 23 \end{smallmatrix}\right\rangle$. Finally the coupling between $|\begin{smallmatrix} i \\ i \end{smallmatrix}\rangle$ and $|\begin{smallmatrix} ij \\ ij \end{smallmatrix}\rangle$ it is taken from an average of $\left\langle \begin{smallmatrix} 2 \\ 2 \end{smallmatrix}\right| H_{\mathrm{CI}}^{eff} \left|\begin{smallmatrix} 12 \\ 12 \end{smallmatrix}\right\rangle$ and $\left\langle \begin{smallmatrix} 2 \\ 2 \end{smallmatrix}\right| H_{\mathrm{CI}}^{eff} \left|\begin{smallmatrix} 23 \\ 23 \end{smallmatrix}\right\rangle$ of the trimer. In all the other cases the coupling is set to zero.

(ii) the coupling between $|\begin{matrix} i \\ i \end{matrix}\rangle$ S configuration with $|\begin{matrix} ij \\ ij \end{matrix}\rangle$ MEu configurations is set to $\langle\begin{matrix} 1 \\ 1 \end{matrix}| H_{\mathrm{CI}}^{eff} |\begin{matrix} 13 \\ 13 \end{matrix}\rangle$, if $|i - j| = 2$.

6.6 Application of the matrix partitioning scheme: the decamer case

We apply the method previously explained to a decamer linear chain. In our effective Hamiltonian treatment the number of states of interest (the basis) is given by 10 S configurations and 45 ME configurations. This will lead to 10 S states and 45 ME states, where the ME states can be divided in two sub-groups: there are 9 MEb states and 36 MEu states. In **Figure 6.6** we show the results obtained for T (panel a) and P (panel b) scenarios at different values of F' and V_{ex}.

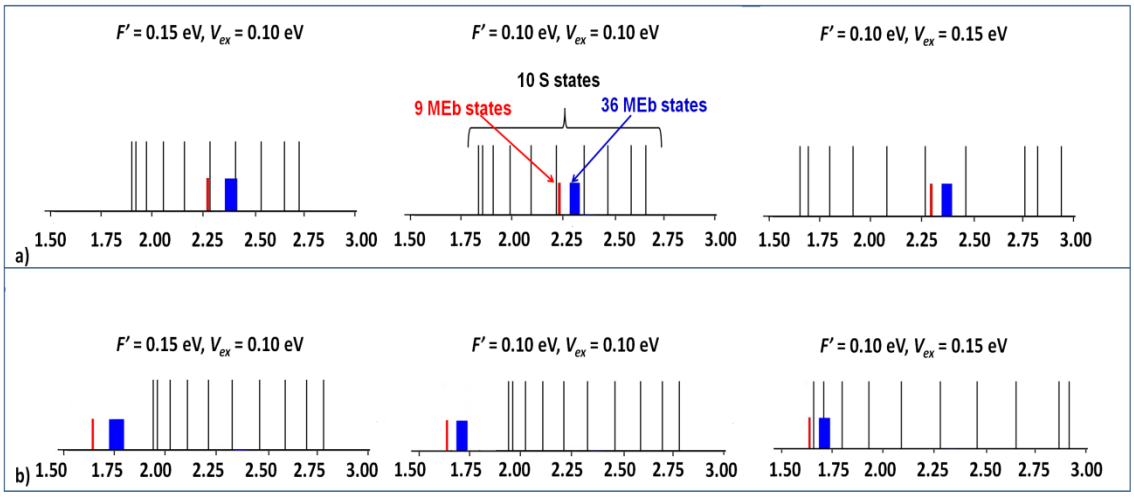

Figure 6.6: Schematic representation of energy levels of S, MEb and MEu states for a decamer for a) a T choice of parameters b) a P choice of parameters, respectively.

First of all, we notice that, with ten monomers, we visualize two different bands. A Frenkel exciton band, whose width is ruled by the excitonic coupling, and a ME "band",

whose width is smaller and dominated by the overlap dependent matrix elements. This is not a proper band because band structure theory describes only single electron states, while in this case we are considering double excited states. This "band" can be divided in two parts: the bottom of it consists of MEb while the rest features the MEu states.

Computing the width of Frenkel exciton band and of the ME "band" represents an important result since it helps understanding the physics of the SF process. In particular, the narrowness of MEb and MEu "bands" is interesting because it implies that these states are localized by electron-phonon coupling[136, 232, 233]. In fact, values of electron-phonon coupling for tetracene and pentacene are on the order of 10^{-1} eV[136, 232, 233], while MEb (in particular) and MEu "bands" are extremely narrow, their width being approximately comprised within values around 10^{-2} eV. On the other hand, singlets are likely to be delocalized as the size of V_{ex} is of the same order of magnitude of exciton-phonon coupling.

The picture, moreover, shows clearly how there is not a unique SF but there are two possible pathways for SF, since there are two separated sets of ME states, that, for reasonable values of F', are also well separated in energy. Both type of states are localized, therefore we can imagine the SF as a process where there is a transition from a delocalized singlet state to a localized ME state. It would have been impossible to observe this feature without a model capable of going beyond the description of a simple dimer, where there is only one ME state and has no other option than being localized.

Moreover, the two types of ME states are composed by different type of configurations. While MEb state are basically dominated by double excited configurations $|{}^{ij}_{ij}\rangle$ with

$|i-j|=1$, where the two pseudo-triplets are at overlap distance and are stabilized respect of two separated triplets, MEu states are composed by double excited configurations $|{}^{ij}_{ij}\rangle$ with $|i-j|>1$: the two pseudo-triplets are localized far apart from each other and are more likely to provide fast generation of two separated triplets.

The analysis of the competition between these two sets of states, as possible final states in the non-radiative process from a S state, is fundamental, since it can affect the efficiency of SF-based solar cells. In fact we know from literature that SF in an OSC must already compete with exciton separation at the interface[27]. Stabilized MEb are likely to have a longer lifetime in an organic crystalline material, due to their binding energy. They could migrate at the interface, where only a single charge could be collected, as the transfer of a second charge would be impeded by electrostatic repulsion, thus further weakening the SF efficiency. The rates of SF and the branching of SF in two possible pathways will be treated in detail in Chapter 7.

6.7 Conclusions

In this Chapter we developed a model Hamiltonian that enabled us to study the electronic structure of a linear chain of molecules undergoing to SF, overcoming the limitations of previous *ab initio* studies and phenomenological models. A preliminary study of a dimer SDCI Hamiltonian, including all singles and doubles excitations, showed that, at short inter-monomer distance, the ME state is stabilized (for a reasonable choice of parameters), its energy being lower than the energy of two separated triplets, and that the size of this stabilization is due to coupling with singles and doubles charge transfer configuration, via overlap dependent matrix elements. This model, while being only a starting point, is already more accurate than previous models that only feature few configurations. An analogue study of a trimer SDCI Hamiltonian illustrated the presence, for clusters larger than a dimer, of two types of ME states: stabilized bound ME states (MEb) composed by double excited configurations, where the two pseudo-triplets are located on neighboring sites, and unbound ME state (MEu) given by the configuration where the two pseudo-triplets are separated and outside the overlap region, its energy almost equal to the energy of two separated triplets. This proves further more that calculations on dimers or dimer models are not sufficient to capture the whole physics of a system subject to SF, since they cannot describe the electronic structure of larger cluster, as they miss fundamental states, which just do not exist in dimers. Matrix partitioning scheme is hence employed to describe a linear chain of N monomers, from the Hamiltonian of the trimer. Finally, the study of a decamer linear chain shows that, in a large cluster, we can start describing the electronic structure of the system in terms of bands: a S band with N states, whose width is related to the size of V_{ex}, and a ME "band", which is very narrow and can be divided in two parts: a

MEb “band” and a MEu “band”. While the S states are delocalized, the ME “bands” are so narrow that the states will be localized by electron-phonon coupling and, therefore, we can say that in SF there is a transition from a delocalized S state to localized ME states, a result achievable only adopting our approach. Finally, the presence of two type of ME states is something that must be taken into account, since it means that there is not a unique SF but the singlet can undergo to non-radiative decay to either of these states. The application of Fermi golden rule for the study of the ME←S_1 transition and the branching of SF between MEb and MEu states will be discussed in Chapter 7.

Chapter 7:

Dynamics of the ME←S_1 transition as a non-radiative decay

Abstract

In this chapter we adopt Fermi golden rule in order to study the dynamics of the transition from a delocalized singlet state, to a localized ME state in a 1D cluster. We first compute the electronic coupling of S state with both bound and unbound ME states. We show that bound ME states couple stronger with S state than unbound ME states and that the coupling decreases, for increasing value of N. A model of the Huang Rhys factors for the ME← S_1 transition is proposed, assuming that the geometry of S_1 is identical to the one of the ground state and that the ME state geometry is identical to the equilibrium geometry of two triplet states. We verify the validity of the Fermi golden rule approach by exploring the values of broadening for which it is valid, and comparing our results with available experimental data for broadening of vibrationally excited states in acenes crystals. The effect of different parameters of the system on the rate is considered. Finally the branching of the rate between bound and unbound ME states is discussed.

7.1 Introduction

SF rates have been evaluated experimentally in the recent years: lifetimes for the process of the order of hundreds of fs and of picoseconds have been estimated for pentacene and tetracene, respectively.[75, 96, 97] Few theoretical models have been used to compute SF rates: Reichman and coworkers employed Redfield theory[234] to compute SF rates for pentacene dimers, in order to elucidate the controversial role of CT states in SF. They support the thesis that SF is mediated by CT states through a so called "super-exchange", even if the CT state possess high energy.[22-24] Ratner and coworkers employed semi-classical treatments of SF, using Marcus theory, to study SF in perylenediimide dimers.[235] Voorhis and coworkers also adopted a semiclassical treatment computing SF, within the scheme proposed by Bixon and Jortner,[133-135] for dimers of different pentacene and tetracene derivatives.[31] All these methods are applied to dimer systems and make use of spectral densities to describe the phonon degrees of freedom. In chapter 6, however, we have found that a cluster of molecules undergoing singlet fission is characterized by delocalized Frenkel-type excitons and localized ME states. In this Chapter, we aim to describe the dynamics of the transition from a delocalized S state to localized ME states in a linear chain of N monomers, as a non radiative decay, using Fermi golden rule (FGR). We use a phenomenological model, employing realistic parameters. Therefore our calculations provide the correct order of magnitude of the parameters entering the model, without the need of a very accurate evaluation of them, which is beyond the scope of this study. Moreover, we want to describe explicitly the vibrational degrees of freedom involved, instead of using a generic spectral density. In order to fulfill these goals, we need: (i) an evaluation of the electronic coupling between delocalized S states and localized ME states; (ii) a

model for the Huang Rhys factors associated to the S1←ME transition; (iii) an assessment of the validity of the FGR with different choices of the system parameters. Such study additionally provides insight on the competition between MEb and MEu states as decay channels from S_1.

7.2 Calculation of the S_1-ME coupling

In order to study the dynamics of the transition from an initially prepared Frenkel exciton to a localized ME state, using time dependent perturbation theory, it is necessary to define an initial state that is not an eigenstate of the full Hamiltonian H_{CI}^{eff}. We are assuming that optical excitation only generates linear combinations of Frenkel states as the ME states are completely dark. We express the electronic Hamiltonian as the Hamiltonian of two separated families of states (S and ME) and their interaction. H_{CI}^{eff} can be written in the following expression:

$$H_{\mathrm{CI}}^{eff} = [H_{\mathrm{CI}}^{eff}]_{\mathrm{S}} + [H_{\mathrm{CI}}^{eff}]_{\mathrm{ME}} + V_{\mathrm{S-ME}} \tag{7.1}$$

Where $[H_{\mathrm{CI}}^{eff}]_{\mathrm{ME}}$, $[H_{\mathrm{CI}}^{eff}]_{\mathrm{S}}$ and $V_{\mathrm{S-ME}}$ are three matrices of the same size as H_{CI}^{eff}. Matrix elements of these matrices differ from zero in the following cases: (i) $[H_{\mathrm{CI}}^{eff}]_{\mathrm{S}}$ contains the matrix elements of the singlet configurations and the effective coupling among them, (ii) $[H_{\mathrm{CI}}^{eff}]_{\mathrm{ME}}$ contains the matrix elements of the ME configurations and the effective coupling among them; (iii) $V_{\mathrm{S-ME}}$ is the coupling among S and ME. Hence, if we want to describe $V_{\mathrm{S-ME}}$ as a perturbation, we write the unperturbed Hamiltonian $[H_{\mathrm{CI}}^{eff}]_0$ as:

$$[H_{\mathrm{CI}}^{eff}]_0 = \ [H_{\mathrm{CI}}^{eff}]_{\mathrm{S}} \tag{7.2}$$

From diagonalization of $[H_{\mathrm{CI}}^{eff}]_0$, we obtain the matrix of eigenvectors coefficients C, which is a block diagonal matrix with the eigenvectors in one of the diagonal blocks and zeros elsewhere. The electronic couplings between delocalized S states and localized ME states is given by:

$$\bar{V}_{\mathrm{S-ME}} = D^{\dagger} V_{\mathrm{S-ME}} D \tag{7.3}$$

In Chapter 6, we divided the ME states in two categories, bound and unbound ME states, distinguishable for energy difference. However, if the coupling with S states is considered, it is more convenient to group ME states, in terms of distance between the two pseudo-triplets composing the ME. If we define the indexes p and q to denote the sites where the two pseudotriplets of ME_{pq} are located, the distance between the two pseudo-triplets of a ME_{pq} state is given, in unit of monomers, by $\alpha = p - q$. Hence, MEb states are at $\alpha = 1$, while MEu states are at $\alpha > 1$. However the effective coupling of MEu states with S states is not equal for all values of α. In fact, MEu states at $\alpha = 2$ (i.e. ME_{13}) do not couple through CT states with S states but they couple both directly and indirectly with MEb states ($\alpha = 1$), which, in turn couple with S states (see Chapter 6). In the same way, MEu at $\alpha = 3$ couple with MEu at $\alpha = 2$, and so on. Therefore, values of effective coupling between S states and ME are likely to be drastically lowered as the distance between the two pseudo-triplets is increased. This is evident in **Figure 7.1** where values of $\bar{V}_{\mathrm{S}_1-\mathrm{ME}}$ in a cluster with $N = 10$ are reported for ME states with different values of α.

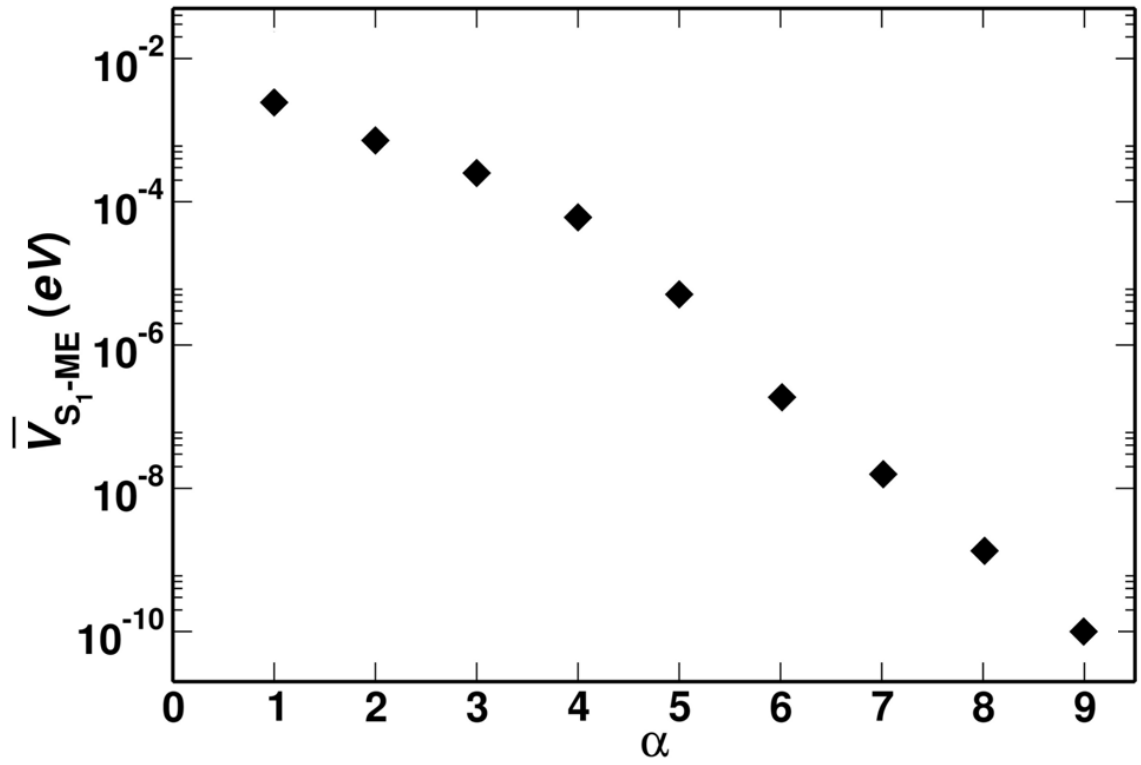

Figure 7.1: $\bar{V}_{S_1-ME}$ as function of α, for a cluster with $N = 10$, at $F' = 0.15$ eV, $V_{ex} = 0.10$ eV.

Figure 7.1 shows clearly how the electronic coupling is drastically lowered when the two pseudo-triplets are far apart. Therefore, it can be argued that the delocalized Frenkel exciton will very rarely decay into a ME state with high value of α. We can predict that there will be a competition between MEb states and MEu states possessing a low value of α. In a cluster of N molecules, there are $\frac{N(N-1)}{2}$ ME states divided in $N - \alpha$ ME states for each possible value of α. MEu energies are closer to S_1 energy while MEb states coupling is stronger. This is fundamental in the study of the branching for the ME←S_1 transition: while MEb states are favored over MEu states by electronic coupling, MEu states are favored by energy difference and, in principle, could be also favored by degeneracy. However, only a fraction of MEu states (up to $\alpha = 4$) possesses a relevant $\bar{V}_{S_1-MEu}$ and, therefore, are viable final states of the transition from an initially prepared Frenkel exciton.

Values of $\bar{V}_{S_1-ME}$ depend on the size of the cluster also for ME states with the same value of α. This is reasonable since, as the Frenkel-type exciton is delocalized over a larger number molecules, its coupling with localized ME states changes. In **Figure 7.2** we report average value of $\bar{V}_{S_1-ME}$ for ME states at $\alpha = 1,2$, as a function of N.

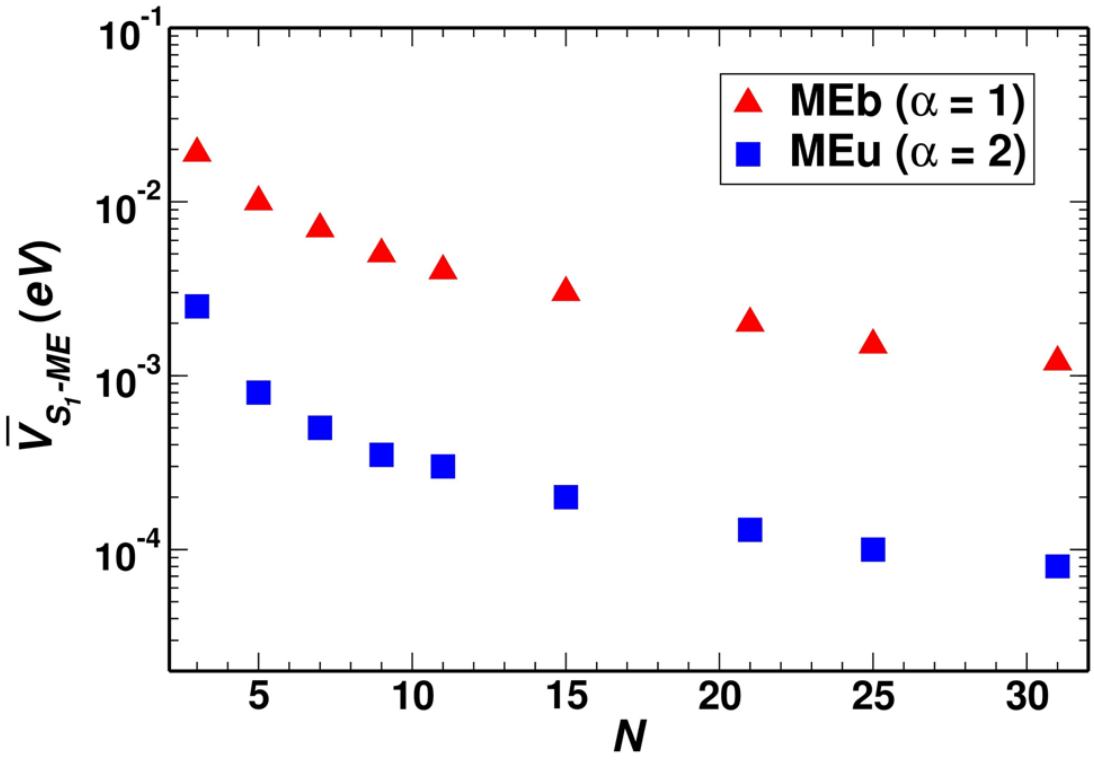

Figure 7.2: Average values of $\bar{V}_{S_1-ME}$ at $\alpha = 1,2$ as function of N ($F' = 0.15$ eV, $V_{ex} = 0.10$ eV)

In **Figure 7.2** values of $\bar{V}_{S-MEb}$ and $\bar{V}_{S-MEu}$ are shown, at a fixed value of model parameters. Both $\bar{V}_{S_1-MEb}$ and $\bar{V}_{S_1-MEu}$ decrease at increasing value of N: as the cluster grows, the coupling between delocalized S states and localized ME states of both type decreases. The N dependence of $\bar{V}_{S-ME}$ is important for the study of the dynamics of the ME←S_1 radiationless transition, because large clusters provide a higher number of ME states, but their coupling with the lowest lying S states is weaker and it is interesting to

study the competition between these two effects with opposite consequence on the rate of the process.

7.3 A generic Hamiltonian to study non-radiative transition in the presence of many acceptor electronic states

We consider a molecular system with M electronic states and n vibrational degrees of freedom. The frequencies of these degrees of freedom are collected in the vector $\boldsymbol{\omega} = \{\omega_i\}$. The vibrational quantum numbers for each electronic state are collected in the vector $\mathbf{v} = \{v_i\}$. Each state is denoted by $|j, \mathbf{v}\rangle$, where j is the electronic state index. We consider a simplified system where an initial state with no vibrational energy (denoted as $|0, \mathbf{0}\rangle$ and of energy E_0) is coupled to a manifold of vibronic states $|j, \mathbf{v}\rangle$ of energy $E_j + \hbar \mathbf{v}^{\mathrm{T}} \boldsymbol{\omega}$. The assumption implies that the zero point energy is included in the electronic energy and that the vibrational degrees of freedom are harmonic.

$$H_{el-vib} = H^0_{el-vib} + V_{el} \tag{7.4}$$

$$H^0_{el-vib} = E_0 |0, \mathbf{0}\rangle\langle 0, \mathbf{0}| + \sum_{j,\mathbf{v}} \left(E_j + \hbar \mathbf{v}^T \boldsymbol{\omega}\right) |j, \mathbf{v}\rangle\langle j, \mathbf{v}| \tag{7.5}$$

$$V_{el} = \sum_{j,\mathbf{v}} V_{j,\mathbf{v}} |j, \mathbf{v}\rangle\langle 0, \mathbf{0}| + h.c. \tag{7.6}$$

Assuming the validity of the Condon approximation, the coupling is the product of the electronic coupling and the Franck-Condon (FC) factor for the harmonic vibrations, that is known analytically. Since we are going to use $V_{j,\mathbf{v}}$ only for computing FGR rates, we report $|V_{j,\mathbf{v}}|^2$:

$$|V_{j,\mathbf{v}}|^2 = |H_{0j}|^2 \cdot \exp\left(-\sum_i \gamma_{i,j}\right) \cdot \prod_i \frac{\gamma_{i,j}}{\nu_i!} \tag{7.7}$$

In the equation above $\gamma_{i,j}$ represents the Huang-Rhys factor for the i-th mode of the electronic transition $0 \rightarrow j$, while H_{0j} is the electronic coupling between initial state and a final state j.

We consider the case of the non radiative transition from a initially prepared S_1 state to $[N \times (N-1)]/2$ manifolds of vibronic ME states, in a cluster of N sites (studied in Chapter 6). Eq. 7.5-7.7 can be rewritten as:

$$H_{el-vib} = E_{S_1}|S_1, \mathbf{0}\rangle\langle S_1, \mathbf{0}| + \sum_{j,\mathbf{v}} \left(E_{ME_j} + \hbar \mathbf{v}^T \boldsymbol{\omega}\right) |ME_j, \mathbf{v}\rangle\langle ME_j, \mathbf{v}| \tag{7.8}$$

$$V_{el} = \sum_{j,\mathbf{v}} V_{j,\mathbf{v}} |ME_j, \mathbf{v}\rangle\langle S_1, \mathbf{0}| + h.c. \tag{7.9}$$

$$|V_{j,\mathbf{v}}|^2 = |\overline{V}_{S_1-ME_j}|^2 \cdot \exp\left(-\sum_i \gamma_{i,j}\right) \cdot \prod_i \frac{\gamma_{i,j}}{\nu_i!} \tag{7.10}$$

If we assume that a generic cluster of *N* monomers behaves as in an Einstein's model for solids[144], where each monomer vibrates independently from each other, the excess energy of an electronic transition ME←S_1, can be distributed among the individual normal modes of each monomer; therefore the size of **ω** and **v** vectors is $N \times n$. Regarding the Huang Rhys factors, it is not straightforward computing them for the ME←S_1 transition. Therefore its modelling will be dealt in detail in the next section.

7.4 Modeling the Huang-Rhys factors for the ME←S1 transition

In the previous section, we expressed the Huang Rhys factors with the notation $\gamma_{i,j}$, indicating the Huang Rhys factor associated to the i-th mode for the electronic transition $0 \rightarrow j$. However, if we consider our model constituted by a 1D cluster of N monomers undergoing to SF and behaving like an Einstein's model, we need to show explicitly also to which monomer belongs the normal mode. Therefore the Huang Rhys factor is expressed with three indexes: $\gamma_{i,j,k}$: in this way we describe the Huang Rhys factor associated to the i-th normal mode of vibration of the k-th monomer of the cluster, for the electronic transition $S_1 \rightarrow ME_j$.

It is important here to recall that the Huang Rhys factor (also called the electron phonon coupling constant) is an a-dimensional quantity related to the displacement between the minimum energy positions of harmonic vibrational potentials associated with initial and final electronic states[236]:

$$\gamma_{i,j,k} = \frac{\lambda_{i,j,k}}{\hbar\omega_i} \tag{7.11}$$

$$\lambda_{i,j,k} = \frac{f_i}{2}\left(\Delta_{i,j,k}\right)^2 \tag{7.12}$$

$$\lambda_{i,j,k} = \frac{f_i\left(\Delta_{i,j,k}\right)^2}{2\hbar\omega_i} \tag{7.13}$$

Where $\lambda_{i,j,k}$ is the contribution to the reorganization energy of the i-th normal mode on the k-th monomer, f_i is the force constant of the i-th mode of frequency ω_i, and $\Delta_{i,j,k}$ is the displacement from lowest S equilibrium geometry of the harmonic vibrational potentials associated to initial and final states.

Modelling $\Delta_{i,j,k}$ and, hence, $\gamma_{i,j,k}$ for the ME←S_1 transition in a 1D cluster is hence performed. In the assumption that the ME state is a localized state formed by two pseudo-triplets on two different sites, the Huang Rhys factors associated to the allowed normal modes for ME←S_1 is approximated to T_1←S_1 Huang Rhys factor of a single molecule, Δ_{i,T_1}, for the sites where the two pseudo-triplets are localized. Hence, we are assuming that the displacement relative to the ME←S_1 electronic transition on all the sites, except the ones where the two pseudo-triplets are allocated, is negligible. This is reasonable since we showed in the previous chapter that the ME band is very narrow and that ME states are likely to be localized by electron-phonon coupling. Therefore, for a transition from S_1 to a ME state described as a $|{}^{pq}_{pq}\rangle$ configuration:

$$\Delta_{i,T_1,k} = \Delta_{i,T_1} \ \forall \ \ k = p, q \tag{7.14}$$

$$\Delta_{i,T_1,k} = 0 \ \forall \ \ k \neq p, q \tag{7.15}$$

However, this is not the only displacement we have to consider; in fact, S_1 is populated, upon photoexcitation, from the ground state S_0. Therefore we have to consider the displacement between S_0 and S_1, $\Delta_{i,S_1,k}$, that can be added or subtracted to the displacement between S_1 and T_1, $\Delta_{i,T_1,k}$. Considering the S_1 state as a linear combination of the N $|{}^{k}_{k}\rangle$ configurations, the displacement Δ_{i,S_1} for a S_0←S_1 transition for a single monomer, is equally distributed among the sites of a chain of N monomers:

$$\Delta_{i,S_1,k} = \frac{\Delta_{i,S_1}}{N} \tag{7.16}$$

The total Huang Rhys factor derives from the displacement due to S_1←S_0 and a subsequent transition to a j-th ME state:

$$\gamma_{i,j,k} = \frac{f_i\left(\frac{\Delta_{i,S_1}}{N} + \Delta_{i,T_1,k}\right)^2}{2\hbar\omega_i} \tag{7.17}$$

For a ME described as a $|{}^{pq}_{pq}\rangle$ configuration, recalling Eq. 7.15, if $k \neq p, q$, Eq. 7.17 becomes:

$$\gamma_{i,j,k\neq p,q} = \frac{f_i\left(\Delta_{i,S_1}\right)^2}{2N^2\hbar\omega_i} \tag{7.18}$$

This means that for $N = 3$, $\gamma_{i,j,k\neq p,q} = \frac{1}{9}\gamma_{i,S_1}$, while for $N = 10$, $\gamma_{i,j,k\neq p,q} = \frac{1}{100}\gamma_{i,S_1}$ (for $N = 2$, k is always equal to p or q). Neglecting the term reported in Eq. 7.18, which decreases for larger clusters as N^2, simplifies substancially the modelling of Huang Rhys factors, enabling the exclusion of normal modes of all the monomers, except the ones where the two pseudo-triplets of ME are located.

For $k = p$ and $k = q$, Eq. 7.17 can be rewritten as:

$$\gamma_{i,j,p} = \gamma_{i,j,q} = \frac{f_i\left(\Delta_{i,T_1}\right)^2}{2\hbar\omega_i} + \frac{f_i\left(\Delta_{i,S_1}\right)^2}{2N^2\hbar\omega_i} + \frac{f_i\left(\Delta_{i,T_1}\cdot\Delta_{i,S_1}\right)}{N\hbar\omega_i} \tag{7.19}$$

Again, for large clusters we can neglect the second and the third terms on the right side of Eq. 7.19.

Therefore, we only need to compute the T_1←S_1 Huang Rhys factors of a single molecule, i.e., pentacene, as represented in **Figure 7.3**, and we obtain the Huang Rhys factors for a ME←S_1 transition from Eq. 7.19. Therefore the size of **ω** and **v** vectors is reduced to $2n$ for each ME state, as we consider that the excess energy of the transition is distributed only among the normal modes of the monomers where the two pseudo-triplets of the ME state are localized. Reorganization energy for the T_1←S_1 transition ($\lambda_{T1\leftarrow S1} = 0.157$ eV) has been also computed at the CIS/6-31G* level of theory for a pentacene molecule, as the difference between the energy of the optimized electronic

structure of T_1 ($E(T_1)_{T_1}$) and the energy of T_1 in the optimized geometry of S_1 ($E(T_1)_{S_1}$) following the procedure adopted in ref.[232, 237]

$$\lambda_{T1\leftarrow S1} = E(T_1)_{T_1} - E(T_1)_{S_1} \tag{7.20}$$

Therefore, $\lambda_{ME\leftarrow S1}$ for a transition taking place in a linear chain of molecules will be twice the value of $\lambda_{T1\leftarrow S1}$ for a process in a single molecule. We obtained this result considering that the geometry of S_1 is identical to the one of S_0, because of delocalization of the S_1 state over several molecules, and that the ME state geometry is assumed to be the equilibrium geometry of two triplet states, because of localization of this type of state.

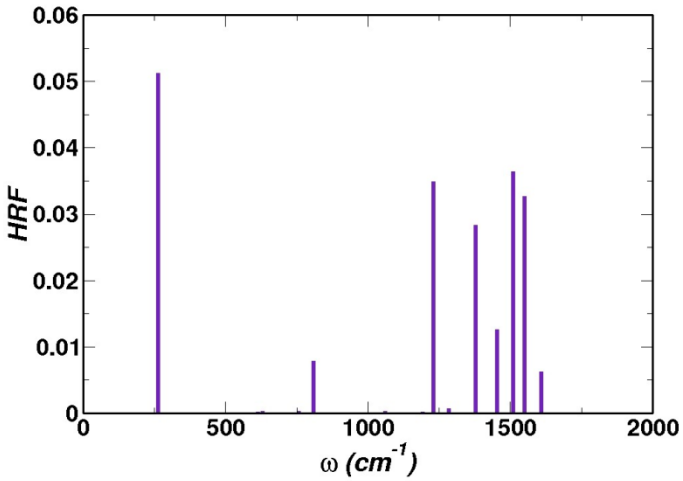

Figure 7.3: Huang Rhys factors for a single pentacene molecule for the normal mode of the corresponding frequency ω, for a $T_1\leftarrow S_1$ electronic transition. S_1 and T_1 optimized electronic structures are computed at the CIS/6-31G* level of theory.

Finally , if we indicate the ME states with the indexes p and q, denoting the site where the two pseudo-triplets are located, instead of using the index j for the number of states, Eq. 7.5-7.7 can be rewritten as follows:

$$H_{el-vib} = E_{S_1}|S_1, \mathbf{0}\rangle\langle S_1, \mathbf{0}| + \sum_{p\neq q,\mathbf{v}} \left(E_{ME_{pq}} + \hbar\mathbf{v}^T\boldsymbol{\omega}\right)|ME_{pq}, \mathbf{v}\rangle\langle ME_{pq}, \mathbf{v}| \tag{7.21}$$

$$V_{el} = \sum_{p \neq q, \mathbf{v}} V_{p,q,\mathbf{v}} \left| \mathrm{ME}_{p,q}, \mathbf{v} \right\rangle \langle \mathrm{S}_1, \mathbf{0} \Big| + h.c. \tag{7.22}$$

$$|V_{pq,\mathbf{v}}|^2 = \bar{V}_{\mathrm{S}_1 - \mathrm{ME}_{pq}}{}^2 \cdot \prod_{i,k} \exp\left(- \sum_{i,k=p,q} \gamma_{i,\mathrm{T}_1} \right) \frac{\gamma_{i,\mathrm{T}_1}}{\nu_i!} \tag{7.23}$$

7.5 Fermi Golden rule for the study of ME←S_1 transition

We study the dynamics of the transition from a delocalized S_1 state to $[N \times (N-1)]/2$ manifolds of localized ME states, using the FGR:

$$k_{\mathrm{tot}} = k_{\mathrm{S}_1, \mathbf{0} \to \{pq, \mathbf{v}\}} = \frac{2\pi}{\hbar} \sum_{p \neq q, \mathbf{v}} |V_{pq,\mathbf{v}}|^2 \delta \left[E_0 - \left(E_{\mathrm{ME}_{pq}} + \hbar \mathbf{v}^T \boldsymbol{\omega} \right) \right] \tag{7.24}$$

$$\tau_{\mathrm{tot}} = \frac{1}{k_{\mathrm{tot}}} \tag{7.25}$$

Where k_{tot} is the total rate and τ_{tot} is the decay time. k_{tot} can be also expressed as the sum of the contributions belonging to MEb and MEu states, respectively.

$$k_{\mathrm{tot}} = k_{\mathrm{MEb}} + k_{\mathrm{MEu}} \tag{7.26}$$

$\delta(x)$ is a delta Dirac function, which is approximated in its limit as a Gaussian function:

$$\frac{1}{\sqrt{2\pi}\sigma} e^{\frac{-(x)^2}{2\sigma^2}} \tag{7.27}$$

σ is a parameter ruling the width of the Gaussian, thus introducing a broadening to the energy of the final states. The physical explanation of a broadening of the vibrationally excited states in crystalline organic materials is given by depopulation and dephasing

processes, which rule the relaxation dynamics of an excited state produced by excitation of the ground state. In our case the ME states are produced by non radiative decay of S_1 but the physical picture can be considered analogous.[238-240]

According to the theory of radiationless transitions[134], electronic non radiative decay processes (i.e. inter-system crossing, internal conversion) in large molecules (such as tetracene and pentacene) correspond to the statistical limit, due to the high density of vibronic final states, ρ_f, acting as an effective continuum.[135, 241] Large molecules obey to the so called weak coupling regime where the initial state is weakly coupled with a dense manifold. ρ_f is related to the large number of degrees of freedom, n, possessed by a large molecule, and to ΔE, the energy difference between the zero-th vibronic levels of initial and final states.[135, 241] In fact the general condition for irreversibility of a radiationless transition is given by the following expressions:

$$t \ll \hbar\rho_f \tag{7.28}$$

$$t_r = \hbar\rho_f \tag{7.29}$$

Where t_r is the recurrence time for the decay of the initial state into the manifold of final states. When $t > t_r$, the population of an initial state i, $P_i(t)$, expressed by the projection of the initial state onto the total wavefunction $\Psi(x,t)$, (Eq. 7.30-7.31) will increase again (oscillating behavior).

$$\Psi(x,t) = \sum_{i=1}^{n} a_i \psi_i(x)\, e^{\frac{-iE_i t}{\hbar}} \tag{7.30}$$

$$P_i(t) = |\langle \psi_i | \Psi(x,t) \rangle|^2 \tag{7.31}$$

In Eq. 7.30 we report the general solution of the time-dependent Shrödinger, where $\psi_i(x)$ is the eigenvector associated to E_i and $\{a_i\}$ are the coefficient of the wave-

function that can be computed imposing the boundary conditions.[242] Nevertheless, for large molecules, $t_r \gg t$ and it is typically beyond the time scale of the experiments. Under these conditions, the non radiative decay can be considered an irreversible process, where the FGR is used to compute the rate constant. A similar picture stays true in condensed media.[135, 241]

In our case, we want to study the radiationless decay from an initially prepared S_1 state to $\frac{[N\times(N-1)]}{2}$ manifolds of ME states ($N-1$ MEb states and $\frac{N^2-3N+2}{2}$ MEu states) in a linear cluster of N monomers. The density of vibronic ME states, ρ_{ME}, is related to the value of the broadening σ: the smaller the σ under which the FGR is valid, the higher the density of states. Moreover, in order for the result to be acceptable, values of σ must be close to a reasonable vibronic broadening of excited states, for a system such as an organic crystalline material.[238-240] As stated before, ρ_{ME} is also related to the energy difference between the zero-th vibronic levels of initial and final states. This is something to take into account, since in Chapter 6 we showed that for a pentacene-like model the zero-th energy difference between S_1 and ME, ΔE, is small, thus reducing the value of ρ_{ME}, possibly placing the system under study in the dense intermediate case (small electronic gap in a large molecule).[241]

In order to explore the limits of validity of the FGR for the system under study, we compute FGR rates, taking into account the following parameters:

(i) the energy difference between the initial and final electronic ground states $\Delta E = E_{\mathrm{S}_1} - E_{\mathrm{ME}_{pq}}$. In the case of a dimer system there is only one electronic ME state, while for larger cluster we showed that two different kind of ME states (MEb and MEu) arise. We showed in previous chapter that MEu and MEb "bands" are very narrow and,

therefore, we assume, in the following calculations, that states belonging to the same set have the same energy. We define ΔE as the energy difference between zero-th vibronic S_1 and MEb: $\Delta E = E_{S_1} - E_{\mathrm{MEb}}$. The energy of MEu states is higher than MEb states and, for each chosen ΔE, we impose that $E_{\mathrm{MEu}} = E_{\mathrm{MEb}} + 0.1$ eV. We perform calculations for different values of ΔE to show the decrease of the rate at increasing values of ΔE, as predicted by the energy gap law.[241]

(ii) the number of normal modes per monomer n: in our study we want to include explicitly the normal modes of vibration. It is clear that the number of vibronic states for each ME depends on n, since we have to consider $2n$ normal modes for each electronic state, as shown in Section 7.4. A way to simplify this scenario can be obtained by grouping normal modes with similar frequencies. In this way, we obtain a reduced number of normal modes $\tilde{n}$, thus decreasing the size of **ω** and **v** vectors.

$$\widetilde{\omega}_h = \left(\sum_i^{\tilde{n}_h} \omega_i \right) {\tilde{n}_h}^{-1} \tag{7.32}$$

$$\tilde{\gamma}_{h,\mathrm{T}_1} = \sum_i^{\tilde{n}_h} \gamma_{i,\mathrm{T}_1} \tag{7.33}$$

The frequency $\widetilde{\omega}_h$ of each grouped mode $\tilde{v}_h$ is given by the average of the frequencies ω_i (as shown in **Figure 7.3**) of the $\tilde{n}_h$ modes composing it. From the values collected in **Figure 7.3**, we only consider Huang Rhys factors whose value is higher than 3% of the highest Huang Rhys factor. The sum of individual Huang Rhys factors, γ_{i,T_1}, produces the corresponding grouped Huang Rhys factors $\tilde{\gamma}_{h,\mathrm{T}_1}$. In **Table 7.1**, we report three different models of the system, given by different grouping of the normal modes shown

in **Figure 7.3**. In particular, we choose $\tilde{n} = 2,5,9$, hence covering cases with small, intermediate and large number of modes.

(iii) the number of monomers N of the cluster: we showed in Section 7.2 that $\bar{V}_{S_1-ME}$ decreases for larger clusters, while in Section 7.4 we demonstrated that, for each ME state, we have to consider only the normal modes where the two pseudo-triplets are located and, hence, the total number of normal modes does not depend on N. Therefore, only the number of MEb and MEu states and the value of $\bar{V}_{S_1-ME}$ depend on N. In the following calculations we compute FGR for different values of N, using the pertinent values of $\bar{V}_{S_1-MEb}$ and $\bar{V}_{S_1-MEu}$.

Table 7.1: Elements of **ω** (cm^{-1}) and their respective Huang Rhys factors for $\tilde{n} = 2,5,9$ respectively.

$\tilde{n} = 2$		$\tilde{n} = 5$		$\tilde{n} = 9$	
$\tilde{\omega}$	$\tilde{\gamma}_{h,T_1}$	$\tilde{\omega}$	$\tilde{\gamma}_{h,T_1}$	$\tilde{\omega}$	$\tilde{\gamma}_{h,T_1}$
261.4	0.0512	261.4	0.0512	261.4	0.0512
1264.7	0.1173	809.4	0.0081	809.4	0.0081
		1255.8	0.0356	1228.3	0.0349
		1398.2	0.0410	1283.4	0.0007
		1556.4	0.0755	1377.7	0.0283
				1451.9	0.0127
				1510.1	0.0365
				1549.8	0.0327
				1609.2	0.0063

An estimation of the minimum value of σ ($\sigma_{\min}$), for which the FGR is valid, is given by the minimum value of σ, for which the following expression is true:

$$\frac{d^2\log(k_{\mathrm{tot}}/s^{-1})}{d(\log\sigma\,/\mathrm{eV})^2} < 10^{-4} \tag{7.34}$$

When FGR is valid, the rate does not depend on the detail of the broadening; if we plot the rate as a function of the broadening, it will reach a plateau at low values of σ. Below this plateau $\log(k_{\mathrm{tot}})$ will diverge to $-\infty$. Eq. 7.34 allows to evaluate the minimum value of sigma before the divergence. In **Figure 7.4** we show this behaviour, reporting k_{tot} against σ, at a fixed value of N (3) and ΔE (0.2 eV), for the three different models of the system: $\tilde{n} = 2,5,9$, while in **Table 7.2** we report values of $\sigma_{\min}$ for different choices of parameters, along with the correspondent value of k_{tot}. Rates are computed using Eq. 7.24. We notice that, while for $\tilde{n} = 2$, the FGR is valid only for high values of σ (~10^{-2} eV), increasing $\tilde{n}$ to 5 or 9 produces the appearance of a second region of validity of the FGR for lower values of σ, which are close to broadening of vibrationally excited states in acenes, reported in literature (~$10^{-3.4}$ - $10^{-3.6}$ eV).[238-240] This is more pronounced for $\tilde{n} = 9$, along with higher k_{tot}, and it is reasonable since, for larger number of modes, the number of vibronic states is drastically increased and so ρ_{ME}. $\tilde{n} = 9$ is clearly the best model for the system, providing a good value of $\sigma_{\min}$. It is also computationally feasible ($\tilde{n} = 9$ means that for each ME state we are considering 18 normal modes), allowing us to use FGR to study the dynamics of ME←S_1. We will always adopt this model for the following calculations.

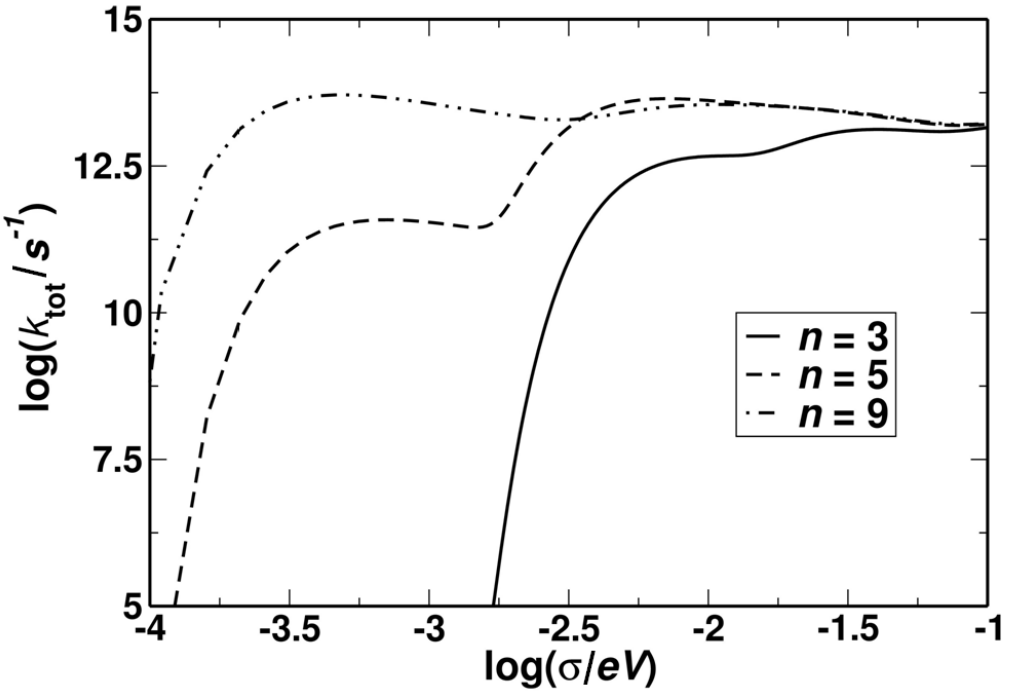

Figure 7.4: $\log(k_{\mathrm{tot}})$ vs. $\log(\sigma)$ for different values of $\tilde{n}$, at $\Delta E = 0.2$ eV and $N = 3$.

Table 7.2: σ_{min} and k_{tot} for different values of $\tilde{n}$ ($\Delta E = 0.2$ eV, $N = 3$).

$\tilde{n}$	$-\log(\sigma_{\mathrm{min}}/\mathrm{eV})$	$\log(k_{\mathrm{tot}}/\mathrm{s}^{-1})$
2	2.2	12.5
5	3.2	11.5
9	3.4	13.7

In **Table 7.3** we collect values of σ_{min} and the relative k_{tot} for $N = 3$ and $\tilde{n} = 9$, for different values of ΔE. We notice that, as predicted by energy gap law, the rate decreases for larger values of ΔE in both the low and the high σ regions, while value of σ_{min} is only marginally affected by ΔE. The energy difference between S_1 and ME states is affected by excitonic coupling as shown in Chapter 6. Therefore, we can imagine that high ΔE correspond to low values of V_{ex}.

Table 7.3: $\sigma_{\min}$ and k_{tot} for different values of ΔE ($N = 3$, $\tilde{n} = 9$)

ΔE (eV)	$-\log(\sigma_{\min}/\mathrm{eV})$	$\log(k_{\mathrm{tot}}/\mathrm{s}^{-1})$
0.2	3.4	13.7
0.4	3.5	12.0
0.6	3.2	10.6

In **Figure 7.5** we report k_{MEb} and k_{MEu}, computed at $\sigma_{\min}$, as a function of N. Rates are computed applying Eq. 7.23, using the pertinent coupling for each ME_{pq}. Both k_{MEb} and k_{MEu} are somewhat constant for low values of N and then decrease for higher values of N, as the weakening of the electronic coupling is not compensated anymore by degeneracy. Nevertheless, it has been reported that a number of molecules below ten (or even four) is sufficient to describe the delocalization of a Frenkel exciton in an acene crystal.[29] Computed transition rates produce decay times from tens to hundreds of fs, which are somewhat in agreement with experimental results for pentacene crystals.[75]

It is interesting to study the branching of the rate between MEb and MEu states. We know that electronic coupling of MEb states with S_1 is stronger than the one relative to MEu states. On the other hand, MEu states are favoured for Franck Condon factors (energy is closer to S_1 and hence vibronic states with lower v are included). MEu states are also more abundant than MEb states. However, we showed in Section 7.2 that only a fraction of MEu states, whose pseudo-triplets are not too far apart, are significantly coupled with the delocalized singlet exciton. The competition among these effects

brings to a difference of more than 1 order of magnitude between k_{MEb}, and k_{MEu}. Therefore, more than 90% of S_1 states decay onto MEb states.

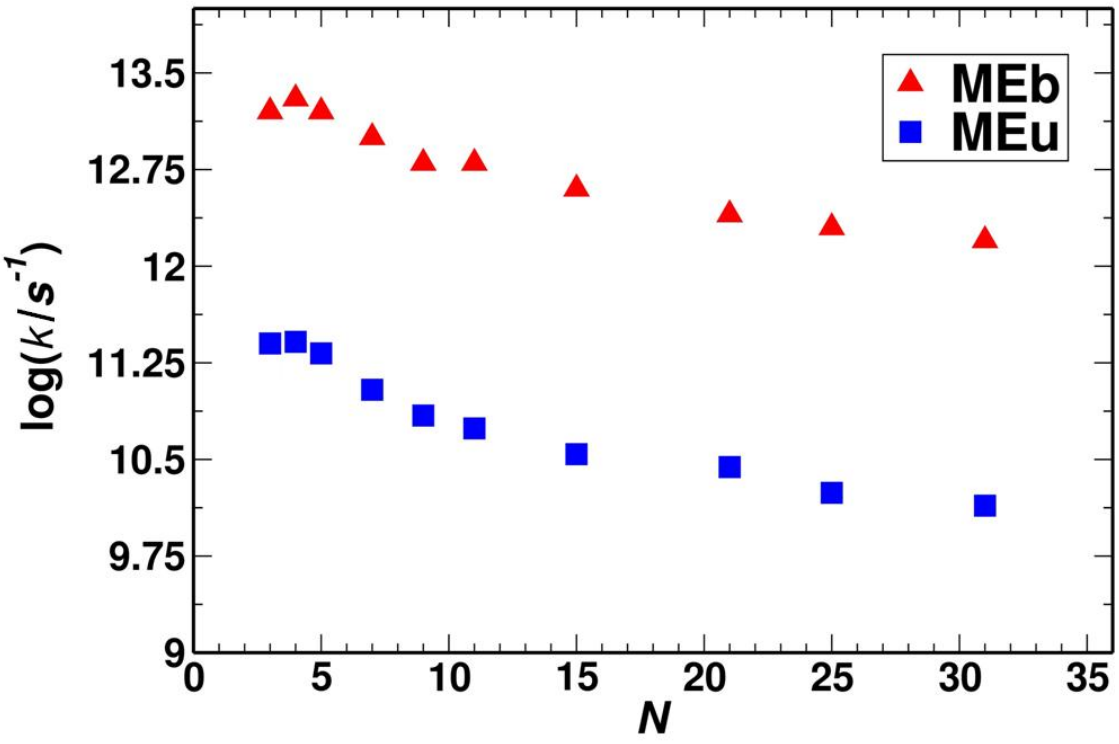

Figure 7.5: $\log(k_{\mathrm{MEb}})$ and $\log(k_{\mathrm{MEu}})$ as function of N ($\Delta E = 0.2$ eV).

This results is interesting because MEb states possess a binding energy, whose entity depends on F', as discussed in Chapter 6. They are stabilized respect to the energy of two triplets ($E_{\mathrm{MEb}} < 2E_{\mathrm{T}_1}$), thus possibly slowing down the final separation into two separate triplets, due to higher lifetime. On the other side, $E_{\mathrm{MEu}} \cong 2E_{\mathrm{T}_1}$, so singlets decaying over the MEu channel would fastly produce two separate triplets. Nevertheless, it is important to underline that for very low values of F', the stabilization of MEb states is very low and, hence, become less distinguishable with MEu states. Also $\bar{V}_{\mathrm{S}_1-\mathrm{MEu}}$ and $\bar{V}_{\mathrm{S}_1-\mathrm{MEb}}$ are related to F', since the coupling between S and MEb states is mediated by CT states, through F' matrix elements, as demonstrated in Chapter

6. Therefore low values of F' will also produce low values of $\bar{V}_{S_1-MEu}$ and $\bar{V}_{S_1-MEb}$, thus affecting the transition rate. The rate of $S_1 \leftarrow$ME transition is also related to V_{ex}, which tunes the energy of S_1 and therefore the energy difference with ME states: for low values of excitonic coupling, S_1 energy is higher and ΔE increases, slowing the transition.

It is important to remind that we are only considering transition from the ground vibronic S_1 to vibronic ME states and we are not considering the subsequent separation of the ME in two separated triplets. A possible continuation of this study could include the time dependent evolution of the ME states. Competition between SF and exciton separation could also be studied, including interface with an acceptor in the model, leading to a complete understanding of the SF efficiency in organic solar cells.

7.6 Conclusions

In this Chapter we studied the dynamics of the transition from an initially prepared delocalized S_1 state to $\frac{[N\times(N-1)]}{2}$ manifolds of localized ME states, in a linear chain of N molecules, whose electronic structure has been described in Chapter 6, as a non radiative decay. We decided to employ FGR for the study of the dynamics of this phenomenon. First of all, we computed the electronic coupling between delocalized S states and localized MEb and MEu states, underlining how these couplings change as a function of N and as a function of the distance between the two pseudo-triplets. We included explicitly the allowed normal modes and hence the vibronic states for each ME state, instead of using a general spectral density, as done in previous models. For this

reason, we modelled the Huang Rhys factors for the ME←S_1 transition, assuming that the S_1 geometry is equivalent to the geometry of the ground state, because of delocalization of the Frenkel state. On the other hand, ME states are considered as two pseudo-triplets localized on two separated sites. The geometry of each of these two sites is assumed to be the equilibrium geometry of a T_1 state. The validity of FGR approach has been verified, computing the rate as function of the broadening of the gaussian approximating the Dirac function, and comparing the results obtained with different sets of parameters with available experimental estimations of broadening for vibrationally excited states in acene crystals. Finally, the branching of the rate between MEb and MEu states has been discussed: we demonstrated that MEb state are favoured over MEu states as preferred decay channel. MEb states have a binding energy, instead of MEu states, whose energy is almost equal to two separated triplets. Therefore their bound nature is likely to affect their time dependent evolution, whose study represents a possible continuation of the project. We underline that it was possible to obtain these results, only going beyond the simplified dimer picture, common to most of recent models and *ab initio* calculations. This study paves the way for further investigation, aimed to analyze the effective efficiency of SF in donor-acceptor systems.

Chapter 8:

Concluding remarks and perspective

In this thesis, we studied two different processes, which play a key role in the mechanism of functioning of third generation solar cells: (i) electron injection in dye sensitized solar cells; (ii) non radiative decay from a Frenkel exciton to a multi-excitonic state, a fundamental step in the mechanism of singlet fission in organic crystalline materials, commonly adopted in organic solar cells.

In Chapter 1, we explained the motivations behind our study, describing the state of the art of these two research fields. We underlined the limitations of current experimental measurements and theoretical methods, which cannot provide full insights on the mechanisms of these processes. In particular, for DSSCs, the complex nature of the device, constituted by different components that cannot be optimized independently from each other, produced a spread of the research efforts in different directions, in order to achieve higher efficiencies. However, due to the lack of systematic design rules, these efforts, while enlarging the knowledge of the field, provided only small improvements of the actual device, if compared to the early Grätzel cell. We, hence, decided to focus our study on a single step of the mechanism of functioning of a DSSC: the electron injection from the photoexcited dye to the semiconductor. While not being the process determining the efficiency of the device, a fast electron injection is surely a requisite for an optimal device and we aimed to provide a computational tool,

independent from experiments, to screen a large number of candidate dyes and to observe in detail the factors affecting the injection rates. Previous works on electron injection in DSSCs were not suitable for a fast and completely *ab initio* analysis of large sets of candidates dyes, neither they were capable of isolating different effects contributing to the injection rate.

On the other hand, studies on SF were limited experimentally by the fact that an important role in SF mechanism is played by a double excited state, the so called multi-excitonic state, which cannot be identified by most of the classical experimental techniques. Moreover, previous theoretical works reached somewhat diverging findings and they were limited by the choice of a small system (typically a dimer extracted from the crystallographic structure of the organic crystalline material) and pertinent only to a particular system. Therefore we decided to contribute to this field, aiming for the theoretical description of larger systems, through a model Hamiltonian of a linear chain of molecules undergoing to SF.

In Chapter 2 we presented in detail the methodologies applied in this thesis, showing how these two different processes can be studied within the same theoretical framework, provided by time-dependent perturbation theory. We also highlighted the consistent differences with recent theoretical approaches. In particular, we described our matrix partitioning approach combined with a diabatization of molecular and semiconductor states, which allowed us to separate the problem of the electronic structure of the dye-semiconductor interface, in smaller and simpler systems, thus providing a powerful tool for an *ab initio* high through-put analysis of possible DSSC dyes.

We also motivated our choice of quantum chemistry methods with a particular focus on CI theory, which have been used to build our model Hamiltonian for the study of SF. We underlined the unsuitableness of previous *ab initio* calculations for the study of large systems, which are necessary for the study of organic crystalline materials, due to their unaffordable computational cost.

In Chapters 3-5 we presented three different applications of our theoretical approach to DSSCs. In Chapter 3 we presented a study of the electron injection characteristics for a large set of organic phosphonated dyes on TiO_2 anatase and rutile surfaces. Our results were in good agreement with available experiments and we demonstrated that our method is capable of capturing effects of chemically different spacer groups, usually employed in DSSC dyes. These two achievements represented the foundation for successive studies, as they proved that our method could be reliably used in a predictive way. In Chapter 4 we, hence, presented a predictive application of our method as we sought for the optimal anchoring group for a DSSC dye. We combined the study of the possible adsorption geometries and adsorption energies of 15 anchoring groups on both anatase and rutile, with calculations of electron injection rates for perylene molecules functionalized with these groups. In this way, we identified moieties, possessing both a strong stability on the semiconductor surface and good injection properties, that can actually substitute the currently used carboxylated anchoring group. Moreover, we showed that the choice of novel anchoring group is not straightforward and cannot be driven by simple chemical wisdom, as it requires the calculation of the anchoring group-surface couplings. Nevertheless, this calculation can provide all the information needed to discern whether an anchoring group is efficient or not, thus avoiding weeks of experimental efforts. Finally, in Chapter 5 we proved that our methodology could be

used also to study organo-metallic dyes with a complex attachment chemistry on the semiconductor's surface, as we studied the attachment chemistry and the electron injection for the N3 dye. However, some caution should be used in the study of this kind of systems as we showed that the correct modeling of the anchoring group is fundamental, as this type of dyes require a larger model of the interface, due to multiple anchoring groups binding to the surface.

The studies reported in this thesis are only a fraction of the possible directions that can be followed with our approach, as, in principle, any dye-semiconductor system could be studied, provided that a correct *ab initio* description of the semiconductor is given, and it could also be extended to different device architectures (nanotubes and nanowires). Further improvements could also be provided by including the solvent, in order to investigate the effect of the surrounding media on electron transfer processes. Effects of co-sensitization on electron injection could also be studied and even a possible adaptation of the model to study solid state DSSCs, which recently showed very promising results, could be performed. In general, the low computational cost of the method, combined with its qualitative and quantitative accuracy, provides a flexible tool that can be used for a variety of different analysis for different systems.

In Chapters 6-7 we presented our study on SF, which has been divided in two parts: analysis of electronic structure and dynamics of SF, respectively. In Chapter 6, we proposed a model CI Hamiltonian for the study of a linear chain of molecules, whose physical parameters mimic two common molecules capable of SF: tetracene and pentacene. Our study of the excited states of this system showed that, as we intuitively guessed, it is not possible, for a cluster larger then a dimer, to define a single ME state, as we can distinguish between two different type of ME states: a bound ME state,

possessing a stabilization energy, and an unbound state whose energy is almost equal to the energy of two separated triplet excitons. The analysis of a large cluster also allowed to define the system in terms of bands: in particular while singlet excitons were found to be delocalized, due to excitonic coupling, we showed that the ME "band" is an almost flat band and, hence, ME states are localized due to electron-phonon coupling. Once defined the electronic structure of our system, in Chapter 7 we studied the radiationless decay from a singlet exciton to a set of ME states, each described with a manifold of vibronic states. An investigation of the electronic coupling between these singlet and ME states showed that it depends upon the size of the linear chain and upon the distance between the two pseudo-triplets composing the multi-exciton. Highest couplings are provided by bound ME states, while the coupling fastly decreases as the two psedo-triplets are located far from each other. A model for describing explicitly the vibrational degrees of freedom of the ME state was proposed, assuming that each pseudo-triplet has the same geometry of a triplet exciton and that, due to delocalization on several molecules, the S_1 state has the same geometry of the ground state. Therefore, we computed the rates of ME←S_1 transition, having verified that Fermi golden rule is a viable approach for this kind of study. In particular, we analyzed the branching of the rate, among different types of ME, and we realized that transition occurs towards bound-type ME states for more than 90% of the singlet excitons, on a timescale of tens to hundreds fs, depending on the size of the cluster. Therefore, we can state that, according to our studies, in SF mechanism, the delocalized Frenkel exciton decays onto a localized state of multi-excitonic nature, whose two pseudo-triplets are located on neighboring molecules. We care to remark that these results could be obtained only within our phenomenological model approach and, as far as the author is aware, this is

the first study of SF on a large model system. A possible evolution of this study could be represented by the extension of the model to a two-dimensional system where the parameters are tuned in both directions, in order to verify our results with a more realistic system. Moreover, an interface with a model acceptor could be implemented, in order to study both the competition of SF with exciton dissociation and the time dependent evolution of the ME state in a heterogeneous system.

In conclusion, we strongly believe that the theoretical investigations presented in this thesis can contribute significantly to the research field of third generation solar cells and leave open a wide variety of opportunities for further studies.

Francesco Ambrosio

June 2014

Bibliography

1. Hubbert, M.K., *Energy from Fossil Fuels.* Science (New York, N.Y.), 1949. **109**(2823): p. 103-9.
2. Hubbert, M.K., *ENERGY RESOURCES*. Committee on Resources and Man, National Academy of Sciences, National Research Council. Resources and Man. Xi + 259p. Illus. Maps. W.H. Freeman and Co.: San Francisco, Calif., U.S.A. 1969. 157-242.
3. Lynch, M.C., *Oil scarcity, Oil crises, and alternative energies - don't be fooled again.* Appl. Energ., 1999. **64**(1-4): p. 31-53.
4. http://www.unfccc.int.
5. *Key World Energy Statistics*, 2011, International Energy Agency.
6. Price, S. and R. Margolis, Solar Technologies Market Report, 2008, U.S. Department of Energy.
7. Green, M.A., *Silicon solar cells: state of the art.* Philos. Trans. R. Soc. A, 2013. **371**(1996).
8. Dale, M. and S.M. Benson, *Energy Balance of the Global Photovoltaic (PV) Industry - Is the PV Industry a Net Electricity Producer?* Environ. Sci. Technol., 2013. **47**(7): p. 3482-3489.
9. Shah, A., P. Torres, R. Tscharner, N. Wyrsch, and H. Keppner, *Photovoltaic Technology: The Case for Thin-Film Solar Cells.* Science, 1999. **285**(5428): p. 692-698.
10. *Mineral Commodity Summaries*. 2012 Geological Survey: Government Printing Office.
11. Conibeer, G., *Third-generation photovoltaics.* Mater. Today, 2007. **10**(11): p. 42-50.
12. Oregan, B. and M. Grätzel, *A low-cost, high-efficiency solar cell based on dye-sensitized colloidal TiO_2 films.* Nature, 1991. **353**(6346): p. 737-740.

13. Yella, A., H.W. Lee, H.N. Tsao, C.Y. Yi, and A.K. Chandiran, *Porphyrin-sensitized solar cells with cobalt (II/III)-based redox electrolyte exceed 12 percent efficiency* Science, 2011. **334**(6060): p. 1203-1203.
14. Burschka, J., N. Pellet, S.J. Moon, R. Humphry-Baker, P. Gao, M.K. Nazeeruddin, and M. Grätzel, *Sequential deposition as a route to high-performance perovskite-sensitized solar cells.* Nature, 2013. **499**(7458): p. 316.
15. Martsinovich, N. and A. Troisi, *Theoretical Studies of Dye-Sensitised Solar Cells: From Electronic Structure to Elementary Processes.* Energy Environ. Sci., 2011. **4**: p. 4473-4495.
16. Shockley, W. and H.J. Queisser, *Detailed Balance Limit of Efficiency of p-n Junction Solar Cells.* J. Appl. Phys., 1961. **32**(3): p. 510-519.
17. Smith, M.B. and J. Michl, *Singlet Fission.* Chem. Rev., 2010. **110**(11): p. 6891-6936.
18. Congreve, D.N., J. Lee, N.J. Thompson, E. Hontz, S.R. Yost, P.D. Reusswig, M.E. Bahlke, S. Reineke, T. Van Voorhis, and M.A. Baldo, *External Quantum Efficiency Above 100% in a Singlet-Exciton-Fission–Based Organic Photovoltaic Cell.* Science, 2013. **340**(6130): p. 334-337.
19. Smith, M.B. and J. Michl, *Recent Advances in Singlet Fission.* Annu. Rev. Phys. Chem., 2013. **64**(1): p. 361-386.
20. Lee, J., P. Jadhav, and M.A. Baldo, *High efficiency organic multilayer photodetectors based on singlet exciton fission.* Appl. Phys. Lett., 2009. **95**(3).
21. Aryanpour, K., J.A. Muñoz, and S. Mazumdar, *Does Singlet Fission Enhance the Performance of Organic Solar Cells?* J. Phys. Chem. C, 2013. **117**(10): p. 4971-4979.
22. Chan, W.-L., T.C. Berkelbach, M.R. Provorse, N.R. Monahan, J.R. Tritsch, M.S. Hybertsen, D.R. Reichman, J. Gao, and X.Y. Zhu, *The Quantum Coherent Mechanism for Singlet Fission: Experiment and Theory.* Acc. Chem. Res., 2013. **46**(6): p. 1321-1329.
23. Berkelbach, T.C., M.S. Hybertsen, and D.R. Reichman, *Microscopic theory of singlet exciton fission. I. General formulation.* J. Chem. Phys., 2013. **138**(114102).

24. Berkelbach, T.C., M.S. Hybertsen, and D.R. Reichman, *Microscopic theory of singlet exciton fission. II. Application to pentacene dimers and the role of superexchange.* J. Chem. Phys., 2013. **138**(114103).
25. Feng, X., A.V. Luzanov, and A.I. Krylov, *Fission of Entangled Spins: An Electronic Structure Perspective.* Phys. Chem. Lett., 2013. **4**(22): p. 3845-3852.
26. Beljonne, D., H. Yamagata, J.L. Brédas, F.C. Spano, and Y. Olivier, *Charge-transfer excitations steer the Davydov splitting and mediate singlet exciton fission in pentacene.* Phys. Rev. Lett., 2013. **110**(22): p. 226402.
27. Akimov, A.V. and O.V. Prezhdo, *Nonadiabatic Dynamics of Charge Transfer and Singlet Fission at the Pentacene/C60 Interface.* J. Am. Chem. Soc., 2014. **136**(4): p. 1599-1608.
28. Zimmerman, P.M., Z.Y. Zhang, and C.B. Musgrave, *Singlet fission in pentacene through multi-exciton quantum states.* Nat. Chem., 2010. **2**(8): p. 648-652.
29. Zimmerman, P.M., F. Bell, D. Casanova, and M. Head-Gordon, *Mechanism for Singlet Fission in Pentacene and Tetracene: From Single Exciton to Two Triplets.* J. Am. Chem. Soc., 2011. **133**(49): p. 19944-19952.
30. Casanova, D., *Electronic Structure Study of Singlet Fission in Tetracene Derivatives.* J. Chem. Theory Comput., 2013. **10**(1): p. 324-334.
31. Yost, S.R., J. Lee, W.B. WilsonMark, T. Wu, D.P. McMahon, R.R. Parkhurst, N.J. Thompson, D.N. Congreve, A. Rao, K. Johnson, M.Y. Sfeir, M. Bawendi, T.M. Swager, R.H. Friend, M.A. Baldo, and V.T. Voorhis, *A transferable model for singlet-fission kinetics.* Nat. Chem., 2014. **advance online publication**: http://dx.doi.org/10.1038/nchem.1945.
32. Dos Santos, T., A. Morandeira, S. Koops, A.J. Mozer, G. Tsekouras, Y. Dong, P. Wagner, G. Wallace, J.C. Earles, K.C. Gordon, D. Officer, and J.R. Durrant, *Injection Limitations in a Series of Porphyrin Dye-Sensitized Solar Cells.* J. Phys. Chem. C, 2010. **114**(7): p. 3276-3279.
33. O'Regan, B.C. and J.R. Durrant, *Kinetic and Energetic Paradigms for Dye-Sensitized Solar Cells: Moving from the Ideal to the Real.* Acc. Chem. Res., 2009. **42**(11): p. 1799-1808.

34. Maggio, E., N. Martsinovich, and A. Troisi, *Evaluating Charge Recombination Rate in Dye-Sensitized Solar Cells from Electronic Structure Calculations.* J. Phys. Chem. C, 2012. **116**(14): p. 7638-7649.
35. Durrant, J.R., S.A. Haque, and E. Palomares, *Towards optimisation of electron transfer processes in dye sensitised solar cells.* Coord. Chem. Rev., 2004. **248**(13-14): p. 1247-1257.
36. Prezhdo, O.V., W.R. Duncant, and V.V. Prezhdo, *Dynamics of the photoexcited electron at the chromophore-semiconductor interface.* Acc. Chem. Res., 2008. **41**(2): p. 339-348.
37. Maggio, E., N. Martsinovich, and A. Troisi, *Theoretical study of charge recombination at the TiO_2-electrolyte interface in dye sensitised solar cells.* Journal of Chemical Physics, 2012. **137**(22).
38. Maggio, E.,Ph. D. Thesis, University of Warwick, 2013. http://wrap.warwick.ac.uk/57508/1/WRAP_THESIS_Maggio_2013.pdf.
39. Hagfeldt, A., G. Boschloo, L.C. Sun, L. Kloo, and H. Pettersson, *Dye-Sensitized Solar Cells.* Chem. Rev., 2010. **110**(11): p. 6595-6663.
40. Labat, F., P. Baranek, C. Domain, C. Minot, and C. Adamo, *Density functional theory analysis of the structural and electronic properties of TiO_2 rutile and anatase polytypes: Performances of different exchange-correlation functionals.* J. Chem. Phys., 2007. **126**(15).
41. Labat, F., P. Baranek, and C. Adamo, *Structural and electronic properties of selected rutile and anatase TiO_2 surfaces: An ab initio investigation.* J. Chem. Theory Comput., 2008. **4**(2): p. 341-352.
42. Zhang, H. and J. F. Banfield, *Thermodynamic analysis of phase stability of nanocrystalline titania.* J. Mater. Chem., 1998. **8**(9): p. 2073-2076.
43. Barnard, A.S., P. Zapol, and L.A. Curtiss, *Modeling the Morphology and Phase Stability of TiO2 Nanocrystals in Water.* J. Chem. Theory Comput., 2004. **1**(1): p. 107-116.
44. Tebby, Z., T. Uddin, Y. Nicolas, C.l. Olivier, T. Toupance, C. Labrugère, and L. Hirsch, *Low-Temperature UV Processing of Nanoporous SnO_2 Layers for Dye-Sensitized Solar Cells.* ACS Appl. Mater. Interfaces, 2011. **3**(5): p. 1485-1491.

45. Zheng, H., Y. Tachibana, and K. Kalantar-zadeh, *Dye-Sensitized Solar Cells Based on WO_3.* Langmuir, 2010. **26**(24): p. 19148-19152.

46. Diamant, Y., S. Chappel, S.G. Chen, O. Melamed, and A. Zaban, *Core-shell nanoporous electrode for dye sensitized solar cells: the effect of shell characteristics on the electronic properties of the electrode.* Coord. Chem. Rev., 2004. **248**(13-14): p. 1271-1276.

47. Lenzmann, F., J. Krueger, S. Burnside, K. Brooks, M. Grätzel, D. Gal, S. Ruhle, and D. Cahen, *Surface photovoltage spectroscopy of dye-sensitized solar cells with TiO_2, $Nb2O_5$, and $SrTiO_3$ nanocrystalline photoanodes: Indication for electron injection from higher excited dye states.* J. Phys. Chem. B, 2001. **105**(27): p. 6347-6352.

48. Law, M., L.E. Greene, J.C. Johnson, R. Saykally, and P.D. Yang, *Nanowire dye-sensitized solar cells.* Nat. Mater., 2005. **4**(6): p. 455-459.

49. Enache-Pommer, E., B. Liu, and E.S. Aydil, *Electron transport and recombination in dye-sensitized solar cells made from single-crystal rutile TiO_2 nanowires.* Phys. Chem. Chem. Phys., 2009. **11**(42): p. 9648-9652.

50. Chen, D., F. Huang, Y.-B. Cheng, and R.A. Caruso, *Mesoporous Anatase TiO2 Beads with High Surface Areas and Controllable Pore Sizes: A Superior Candidate for High-Performance Dye-Sensitized Solar Cells.* Adv. Mater., 2009. **21**(21): p. 2206-2210.

51. Daeneke, T., T.H. Kwon, A.B. Holmes, N.W. Duffy, U. Bach, and L. Spiccia, *High-efficiency dye-sensitized solar cells with ferrocene-based electrolytes.* Nat. Chem., 2011. **3**(3): p. 211-215.

52. Zhang, Z., P. Chen, T.N. Murakami, S.M. Zakeeruddin, and M. Grätzel, *The 2,2,6,6-Tetramethyl-1-piperidinyloxy Radical: An Efficient, Iodine- Free Redox Mediator for Dye-Sensitized Solar Cells.* Adv. Funct. Mater., 2008. **18**(2): p. 341-346.

53. Humphry-Baker, N., K. Driscoll, A. Rao, T. Torres, H.J. Snaith, and R.H. Friend, *Time-Evolution of Poly(3-Hexylthiophene) as an Energy Relay Dye in Dye-Sensitized Solar Cells.* Nano Letters, 2011. **12**(2): p. 634-639.

54. Nazeeruddin, M.K., A. Kay, I. Rodicio, R. Humphry-Baker, E. Mueller, P. Liska, N. Vlachopoulos, and M. Grätzel, *Conversion of light to electricity by cis*

- *X2bis(2,2'-bipyridyl - 4,4'- dicarboxylate)ruthenium(II) charge-transfer sensitizers (X = Cl-, Br-, I-, CN-, and SCN-) on nanocrystalline titanium dioxide electrodes.* J. Am. Chem. Soc., 1993. **115**(14): p. 6382-6390.

55. Chiba, Y., A. Islam, Y. Watanabe, R. Komiya, N. Koide, and L. Han, *Dye-Sensitized Solar Cells with Conversion Efficiency of 11.1%.* Jpn. J. Appl. Phys., 2006. **45**(25): p. L638.
56. Cao, Y., Y. Bai, Q. Yu, Y. Cheng, S. Liu, D. Shi, F. Gao, and P. Wang, *Dye-Sensitized Solar Cells with a High Absorptivity Ruthenium Sensitizer Featuring a 2-(Hexylthio)thiophene Conjugated Bipyridine.* J Phys. Chem. C, 2009. **113**(15): p. 6290-6297.
57. Ito, S., S.M. Zakeeruddin, R. Humphry-Baker, P. Liska, R. Charvet, P. Comte, M.K. Nazeeruddin, P. Péchy, M. Takata, H. Miura, S. Uchida, and M. Grätzel, *High-Efficiency Organic-Dye- Sensitized Solar Cells Controlled by Nanocrystalline-TiO_2 Electrode Thickness.* Adv. Mater., 2006. **18**(9): p. 1202-1205.
58. Zhang, G., H. Bala, Y. Cheng, D. Shi, X. Lv, Q. Yu, and P. Wang, *High efficiency and stable dye-sensitized solar cells with an organic chromophore featuring a binary [small pi]-conjugated spacer.* Chem. Commun., 2009(16): p. 2198-2200.
59. Zeng, W., Y. Cao, Y. Bai, Y. Wang, Y. Shi, M. Zhang, F. Wang, C. Pan, and P. Wang, *Efficient Dye-Sensitized Solar Cells with an Organic Photosensitizer Featuring Orderly Conjugated Ethylenedioxythiophene and Dithienosilole Blocks.* Chem. Mater., 2010. **22**(5): p. 1915-1925.
60. Srinivas, K., K. Yesudas, K. Bhanuprakash, V.J. Rao, and L. Giribabu, *A Combined Experimental and Computational Investigation of Anthracene Based Sensitizers for DSSC: Comparison of Cyanoacrylic and Malonic Acid Electron Withdrawing Groups Binding onto the TiO_2 Anatase (101) Surface.* J. Phys. Chem. C, 2009. **113**(46): p. 20117-20126.
61. Mishra, A., M.K.R. Fischer, and P. Bauerle, *Metal-Free Organic Dyes for Dye-Sensitized Solar Cells: From Structure: Property Relationships to Design Rules.* Angewandte Chemie-International Edition, 2009. **48**(14): p. 2474-2499.

62. Cid, J.J., J.H. Yum, S.R. Jang, M.K. Nazeeruddin, E.M. Ferrero, E. Palomares, J. Ko, M. Grätzel, and T. Torres, *Molecular cosensitization for efficient panchromatic dye-sensitized solar cells.* Angew. Chem. Int. Ed., 2007. **46**(44): p. 8358-8362.

63. Wilson, M.W.B., A. Rao, K. Johnson, S. Gélinas, R. di Pietro, J. Clark, and R.H. Friend, *Temperature-Independent Singlet Exciton Fission in Tetracene.* J. Am. Chem. Soc., 2013. **135**(44): p. 16680-16688.

64. Jadhav, P.J., A. Mohanty, J. Sussman, J. Lee, and M.A. Baldo, *Singlet Exciton Fission in Nanostructured Organic Solar Cells.* Nano Lett., 2011. **11**(4): p. 1495-1498.

65. Burdett, J.J. and C.J. Bardeen, *Quantum Beats in Crystalline Tetracene Delayed Fluorescence Due to Triplet Pair Coherences Produced by Direct Singlet Fission.* J. Am. Chem. Soc., 2012. **134**(20): p. 8597-8607.

66. Burdett, J.J. and C.J. Bardeen, *The Dynamics of Singlet Fission in Crystalline Tetracene and Covalent Analogs.* Acc. Chem. Res., 2013. **46**(6): p. 1312-1320.

67. Ma, L., K.J. Tan, H. Jiang, C. Kloc, M.-E. Michel-Beyerle, and G.G. Gurzadyan, *Excited-State Dynamics in an α-Perylene Single Crystal: Two-Photon- and Consecutive Two-Quantum-Induced Singlet Fission.* J. Phys. Chem. A, 2014.

68. Johnson, J.C., A.J. Nozik, and J. Michl, *High Triplet Yield from Singlet Fission in a Thin Film of 1,3-Diphenylisobenzofuran.* J. Am. Chem. Soc., 2010. **132**(46): p. 16302-16303.

69. Rao, A., M.W.B. Wilson, S. Albert-Seifried, R. Di Pietro, and R.H. Friend, *Photophysics of pentacene thin films: The role of exciton fission and heating effects.* Phys. Rev. B, 2011. **84**(19).

70. Dillon, R.J., G.B. Piland, and C.J. Bardeen, *Different Rates of Singlet Fission in Monoclinic versus Orthorhombic Crystal Forms of Diphenylhexatriene.* J. Am. Chem. Soc., 2013. **135**(46): p. 17278-17281.

71. Musser, A.J., M. Al-Hashimi, M. Maiuri, D. Brida, M. Heeney, G. Cerullo, R.H. Friend, and J. Clark, *Activated Singlet Exciton Fission in a Semiconducting Polymer.* J. Am. Chem. Soc., 2013. **135**(34): p. 12747-12754.

72. Ehrler, B., M.W.B. Wilson, A. Rao, R.H. Friend, and N.C. Greenham, *Singlet Exciton Fission-Sensitized Infrared Quantum Dot Solar Cells.* Nano Lett., 2012. **12**(2): p. 1053-1057.

73. Walker, B.J., A.J. Musser, D. Beljonne, and R.H. Friend, *Singlet exciton fission in solution.* Nat. Chem., 2013. **5**(12): p. 1019-1024.

74. Lee, J., P. Jadhav, P.D. Reusswig, S.R. Yost, N.J. Thompson, D.N. Congreve, E. Hontz, T. Van Voorhis, and M.A. Baldo, *Singlet Exciton Fission Photovoltaics.* Acc. Chem. Res., 2013. **46**(6): p. 1300-1311.

75. Chan, W.-L., M. Ligges, A. Jailaubekov, L. Kaake, L. Miaja-Avila, and X.-Y. Zhu, *Observing the Multiexciton State in Singlet Fission and Ensuing Ultrafast Multielectron Transfer.* Science, 2011. **334**(6062): p. 1541-1545.

76. Rao, A., M.W.B. Wilson, J.M. Hodgkiss, S. Albert-Seifried, H. Bassler, and R.H. Friend, *Exciton Fission and Charge Generation via Triplet Excitons in Pentacene/C-60 Bilayers.* J. Am. Chem. Soc., 2010. **132**(36): p. 12698-12703.

77. Tabachnyk, M., B. Ehrler, S. Bayliss, R.H. Friend, and N.C. Greenham, *Triplet diffusion in singlet exciton fission sensitized pentacene solar cells.* Appl. Phys. Lett., 2013. **103**(15): p. -.

78. Ehrler, B., B.J. Walker, M.L. Bohm, M.W.B. Wilson, Y. Vaynzof, R.H. Friend, and N.C. Greenham, *In situ measurement of exciton energy in hybrid singlet-fission solar cells.* Nat. Commun., 2012. **3**.

79. Paci, I., J.C. Johnson, X. Chen, G. Rana, D. Popović, D.E. David, A.J. Nozik, M.A. Ratner, and J. Michl, *Singlet Fission for Dye-Sensitized Solar Cells: Can a Suitable Sensitizer Be Found?* J. Am. Chem. Soc., 2006. **128**(51): p. 16546-16553.

80. Jaeger, H.M., K. Hyeon-Deuk, and O.V. Prezhdo, *Exciton Multiplication from First Principles.* Acc. Chem. Res., 2013. **46**(6): p. 1280-1289.

81. Beard, M.C., J.M. Luther, O.E. Semonin, and A.J. Nozik, *Third Generation Photovoltaics based on Multiple Exciton Generation in Quantum Confined Semiconductors.* Acc. Chem. Res., 2012. **46**(6): p. 1252-1260.

82. Wilson, M.W.B., A. Rao, J. Clark, R.S.S. Kumar, D. Brida, G. Cerullo, and R.H. Friend, *Ultrafast Dynamics of Exciton Fission in Polycrystalline Pentacene.* J. Am. Chem. Soc., 2011. **133**(31): p. 11830-11833.

83. Marciniak, H., I. Pugliesi, B. Nickel, and S. Lochbrunner, *Ultrafast singlet and triplet dynamics in microcrystalline pentacene films.* Phys. Rev. B, 2009. **79**(23): p. 235318.

84. Lee, J., M.J. Bruzek, N.J. Thompson, M.Y. Sfeir, J.E. Anthony, and M.A. Baldo, *Singlet Exciton Fission in a Hexacene Derivative.* Adv. Mater., 2013. **25**(10): p. 1445-1448.

85. Mondal, R., R.M. Adhikari, B.K. Shah, and D.C. Neckers, *Revisiting the stability of hexacenes.* Org. Lett., 2007. **9**(13): p. 2505-2508.

86. Payne, M.M., S.R. Parkin, and J.E. Anthony, *Functionalized higher acenes: Hexacene and heptacene.* J. Am. Chem. Soc., 2005. **127**(22): p. 8028-8029.

87. Purushothaman, B., S.R. Parkin, and J.E. Anthony, *Synthesis and Stability of Soluble Hexacenes.* Org. Lett., 2010. **12**(9): p. 2060-2063.

88. Gundlach, L., R. Ernstorfer, and F. Willig, *Pathway-Dependent Electron Transfer for Rod-Shaped Perylene-Derived Molecules Adsorbed in Nanometer-Size TiO_2 Cavities.* The J. Phys. Chem. C, 2007. **111**(36): p. 13586-13594.

89. Hao, E., N.A. Anderson, J.B. Asbury, and T. Lian, *Effect of Trap States on Interfacial Electron Transfer between Molecular Absorbates and Semiconductor Nanoparticles.* J. Phys. Chem. B, 2002. **106**(39): p. 10191-10198.

90. Bartelt, A.F., R. Schutz, A. Neubauer, T. Hannappel, and R. Eichberger, *Influence of TiO2/Perylene Interface Modifications on Electron Injection and Recombination Dynamics.* J. Phys. Chem. C, 2009. **113**(50): p. 21233-21241.

91. Gundlach, L., Ph.D. Thesis - Freie Universitat Berlin, 2005 http://www.diss.fu-berlin.de/2005/269/.

92. Ernstorfer, R., Ph.D. Thesis - Freie Universitat Berlin, 2004 http://www.diss.fu-berlin.de/2004/268/.

93. Rehm, J.M., G.L. McLendon, Y. Nagasawa, K. Yoshihara, J. Moser, and M. Grätzel, *Femtosecond Electron-Transfer Dynamics at a Sensitizing Dye−Semiconductor (TiO2) Interface.* J. of Phys. Chem., 1996. **100**(23): p. 9577-9578.

94. Frontiera, R.R., J. Dasgupta, and R.A. Mathies, *Probing Interfacial Electron Transfer in Coumarin 343 Sensitized TiO2 Nanoparticles with Femtosecond Stimulated Raman.* J. Am. Chem. Soc., 2009. **131**(43): p. 15630.

95. Ghosh, H.N., J.B. Asbury, Y. Weng, and T. Lian, *Interfacial Electron Transfer between Fe(II)(CN)$_6^{4-}$ and TiO$_2$ Nanoparticles: Direct Electron Injection and Nonexponential Recombination.* J. Phys. Chem. B, 1998. **102**(50): p. 10208-10215.

96. Chan, W.L., M. Ligges, and X.Y. Zhu, *The energy barrier in singlet fission can be overcome through coherent coupling and entropic gain.* Nat. Chem., 2012. **4**(10): p. 840-845.

97. Chan, W.-L., J.R. Tritsch, and X.Y. Zhu, *Harvesting Singlet Fission for Solar Energy Conversion: One- versus Two-Electron Transfer from the Quantum Mechanical Superposition.* J. Am. Chem. Soc., 2012. **134**(44): p. 18295-18302.

98. Gundlach, L., T. Letzig, and F. Willig, *Test of theoretical models for ultrafast heterogeneous electron transfer with femtosecond two-photon photoemission data.* J. Chem. Sci., 2009. **121**(5): p. 561-574.

99. Wang, L., W. Chen, and A.T.S. Wee, *Charge transfer across the molecule/metal interface using the core hole clock technique.* Surf. Sci. Rep., 2008. **63**(11): p. 465-486.

100. Mayor, L.C., J. Ben Taylor, G. Magnano, A. Rienzo, C.J. Satterley, J.N. O'Shea, and J. Schnadt, *Photoemission, resonant photoemission, and x-ray absorption of a Ru(II) complex adsorbed on rutile TiO$_2$ (110) prepared by in situ electrospray deposition.* J. Chem. Phys., 2008. **129**(11).

101. Weston, M., A.J. Britton, and J.N. O'Shea, *Charge transfer dynamics of model charge transfer centers of a multicenter water splitting dye complex on rutile TiO$_2$ (110).* J Chem. Phys., 2011. **134**(5).

102. Schnadt, J., P.A. Bruhwiler, L. Patthey, J.N. O'Shea, S. Sodergren, M. Odelius, R. Ahuja, O. Karis, M. Bassler, P. Persson, H. Siegbahn, S. Lunell, and N. Martensson, *Experimental evidence for sub-3-fs charge transfer from an aromatic adsorbate to a semiconductor.* Nature, 2002. **418**(6898): p. 620-623.

103. Schnadt, J., J.N. O'Shea, L. Patthey, L. Kjeldgaard, J. Ahlund, K. Nilson, J. Schiessling, J. Krempasky, M. Shi, O. Karis, C. Glover, H. Siegbahn, N. Martensson, and P.A. Bruhwiler, *Excited-state charge transfer dynamics in systems of aromatic adsorbates on TiO$_2$ studied with resonant core techniques.* J. Chem. Phys., 2003. **119**(23): p. 12462-12472.

104. Schnadt, J., A. Henningsson, M.P. Andersson, P.G. Karlsson, P. Uvdal, H. Siegbahn, P.A. Bruhwiler, and A. Sandell, *Adsorption and charge-transfer study of bi-isonicotinic acid on in situ-grown anatase TiO_2 nanoparticles.* J. Phys. Chem. B, 2004. **108**(10): p. 3114-3122.

105. Diebold, U., *The surface science of titanium dioxide.* Surf. Sci. Rep., 2003. **48**(5-8): p. 53-229.

106. Bredow, T., L. Giordano, F. Cinquini, and G. Pacchioni, *Electronic properties of rutile TiO_2 ultrathin films: Odd-even oscillations with the number of layers.* Phys. Rev. B, 2004. **70**(3).

107. Clifford, J.N., E. Martinez-Ferrero, A. Viterisi, and E. Palomares, *Sensitizer molecular structure-device efficiency relationship in dye sensitized solar cells.* Chem. Soc. Rev., 2011. **40**(3): p. 1635-1646.

108. De Angelis, F., S. Fantacci, A. Selloni, M. Grätzel, and M.K. Nazeeruddin, *Influence of the sensitizer adsorption mode on the open-circuit potential of dye-sensitized solar cells.* Nano Lett., 2007. **7**: p. 3189-3195.

109. Nazeeruddin, M.K., F. De Angelis, S. Fantacci, A. Selloni, G. Viscardi, P. Liska, S. Ito, T. Bessho, and M. Grätzel, *Combined experimental and DFT-TDDFT computational study of photoelectrochemical cell ruthenium sensitizers.* J. Am. Chem. Soc., 2005. **127**(48): p. 16835-16847.

110. De Angelis, F., S. Fantacci, and A. Selloni, *Alignment of the dye's molecular levels with the TiO_2 band edges in dye-sensitized solar cells: a DFT-TDDFT study.* Nanotechnology, 2008. **19**(42).

111. Pastore, M., A. Selloni, S. Fantacci, and F. Angelis, *Electronic and Optical Properties of Dye-Sensitized TiO_2 Interfaces*. Top. Curr. Chem., 2014, Springer Berlin Heidelberg. p. 1-45.

112. Ronca, E., M. Pastore, L. Belpassi, F. Tarantelli, and F. De Angelis, *Influence of the dye molecular structure on the TiO_2 conduction band in dye-sensitized solar cells: disentangling charge transfer and electrostatic effects.* Energy Environ. Sci., 2013. **6**(1): p. 183-193.

113. Kondov, I., M. Čížek, C. Benesch, H. Wang, and M. Thoss, *Quantum Dynamics of Photoinduced Electron-Transfer Reactions in Dye−Semiconductor Systems:*

First-Principles Description and Application to Coumarin 343−TiO_2. J. Phys. Chem. C, 2007. **111**(32): p. 11970-11981.

114. Duncan, W.R., W.M. Stier, and O.V. Prezhdo, *Ab Initio Nonadiabatic Molecular Dynamics of the Ultrafast Electron Injection across the Alizarin−TiO_2 Interface.* J. Am. Chem. Soc., 2005. **127**(21): p. 7941-7951.
115. Duncan, W.R., C.F. Craig, and O.V. Prezhdo, *Time-Domain ab Initio Study of Charge Relaxation and Recombination in Dye-Sensitized TiO_2.* J. Am. Chem. Soc., 2007. **129**(27): p. 8528-8543.
116. Calbo, J., M. Pastore, E. Mosconi, E. Orti, and F. De Angelis, *Computational modeling of single- versus double-anchoring modes in di-branched organic sensitizers on TiO2 surfaces: structural and electronic properties.* Phys. Chem. Chem. Phys., 2014. **16**(10): p. 4709-4719.
117. Wang, H. and M. Thoss, *Multilayer formulation of the multiconfiguration time-dependent Hartree theory*. The Journal of Chemical Physics, 2003. **119**(3): p. 1289-1299.
118. Kondov, I., M. Thoss, and H. Wang, *Theoretical Study of Ultrafast Heterogeneous Electron Transfer Reactions at Dye−Semiconductor Interfaces: Coumarin 343 at Titanium Oxide*. J. Phys. Chem. A, 2005. **110**(4): p. 1364-1374.
119. Li, J., I. Kondov, H. Wang, and M. Thoss, *Theoretical Study of Photoinduced Electron-Transfer Processes in the Dye−Semiconductor System Alizarin−TiO_2.* J. Phys. Chem. C, 2010. **114**(43): p. 18481-18493.
120. Stier, W. and O.V. Prezhdo, *Non-adiabatic molecular dynamics simulation of ultrafast solar cell electron transfer*. Comp. Theor. Chem., 2003. **630**(1–3): p. 33-43.
121. Stier, W. and O.V. Prezhdo, *Nonadiabatic molecular dynamics simulation of light-induced electron transfer from an anchored molecular electron donor to a semiconductor acceptor*. J. Phys. Chem. B, 2002. **106**(33): p. 8047-8054.
122. Stier, W., W.R. Duncan, and O.V. Prezhdo, *Thermally Assisted Sub-10 fs Electron Transfer in Dye-Sensitized Nanocrystalline TiO_2 Solar Cells.* Adv. Mater., 2004. **16**(3): p. 240-244.

123. Rego, L.G.C. and V.S. Batista, *Quantum dynamics simulations of interfacial electron transfer in sensitized TiO_2 semiconductors.* J. Am. Chem. Soc., 2003. **125**(26): p. 7989-7997.

124. Abuabara, S.G., L.G.C. Rego, and V.S. Batista, *Influence of thermal fluctuations on interfacial electron transfer in functionalized TiO_2 semiconductors.* J. Am. Chem. Soc., 2005. **127**(51): p. 18234-18242.

125. Ramakrishna, S., F. Willig, and V. May, *Theory of ultrafast photoinduced heterogeneous electron transfer: Decay of vibrational coherence into a finite electronic–vibrational quasicontinuum.* J. Chem. Phys., 2001. **115**(6): p. 2743-2756.

126. Wang, L., F. Willig, and V. May, *Theory of ultrafast photoinduced heterogeneous electron transfer.* Mol. Simul., 2006. **32**(9): p. 765-781.

127. May, V. and L. Wang, *Plasmon Enhanced Heterogeneous Electron Transfer: A Model Study.* J. Phys. Chem. C, 2014.

128. Jones, D.R. and A. Troisi, *A method to rapidly predict the charge injection rate in dye sensitized solar cells.* Phys. Chem. Chem. Phys., 2010. **12**(18): p. 4625-4634.

129. Martsinovich, N. and A. Troisi, *High-Throughput Computational Screening of Chromophores for Dye-Sensitized Solar Cells.* J. Phys. Chem. C, 2011. **115**(23): p. 11781-11792.

130. Zimmerman, P.M., C.B. Musgrave, and M. Head-Gordon, *A Correlated Electron View of Singlet Fission.* Acc. Chem. Res., 2013. **46**(6): p. 1339-1347.

131. Casanova, D., L.V. Slipchenko, A.I. Krylov, and M. Head-Gordon, *Double spin-flip approach within equation-of-motion coupled cluster and configuration interaction formalisms: Theory, implementation, and examples.* J. Chem. Phys., 2009. **130**(4).

132. Wu, Q., B. Kaduk, and T. Van Voorhis, *Constrained density functional theory based configuration interaction improves the prediction of reaction barrier heights.* J. Chem. Phys., 2009. **130**(3).

133. Jortner, J. and M. Bixon, *Intramolecular vibrational excitations accompanying solvent-controlled electron transfer reactions.* J. Chem. Phys., 1988. **88**(1): p. 167-170.

134. Bixon, M. and J. Jortner, *Intramolecular Radiationless Transitions.* J. Chem. Phys., 1968. **48**(2): p. 715-726.

135. Bixon, M. and J. Jortner, *Electronic Relaxation in Large Molecules.* J. Chem. Phys., 1969. **50**(9): p. 4061-4070.

136. Yamagata, H., J. Norton, E. Hontz, Y. Olivier, D. Beljonne, J.L. Brédas, R.J. Silbey, and F.C. Spano, *The nature of singlet excitons in oligoacene molecular crystals.* J. Chem. Phys., 2011. **134**(20).

137. Levine, I.N., *Quantum chemistry*. Vol. 5. 2000, Prentice Hall Upper Saddle River, NJ.

138. Szabo, A. and N.S. Ostlund, *Modern quantum chemistry: introduction to advanced electronic structure theory*. 2012, Courier Dover Publications.

139. Löwdin, P.-O., *Quantum theory of many-particle systems. III. Extension of the Hartree-Fock scheme to include degenerate systems and correlation effects.* Phys. rev., 1955. **97**(6): p. 1509.

140. Parr, R.G. and W. Yang, *Density-functional theory of atoms and molecules*. Vol. 16. 1989: Oxford university press.

141. Hohenberg, P. and W. Kohn, *Inhomogeneous electron gas.* Phys. rev., 1964. **136**(3B): p. B864.

142. Kohn, W. and L.J. Sham, *Self-consistent equations including exchange and correlation effects.* Phys. Rev., 1965. **140**(4A): p. A1133.

143. Sousa, S.F., P.A. Fernandes, and M.J. Ramos, *General performance of density functionals.* J. Phys. Chem. A, 2007. **111**(42): p. 10439-10452.

144. Kittel, C. and P. McEuen, *Introduction to solid state physics*. Vol. 8. 1986, Wiley New York.

145. Vydrov, O.A. and G.E. Scuseria, *Assessment of a long-range corrected hybrid functional.* J. Chem. Phys., 2006. **125**(23): p. 234109.

146. Sholl, D. and J.A. Steckel, *Density functional theory: a practical introduction*. 2011, John Wiley & Sons.

147. Becke, A.D., *Density-functional thermochemistry. III. The role of exact exchange.* J. Chem. Phys., 1993. **98**(7): p. 5648-5652.

148. Martsinovich, N., D.R. Jones, and A. Troisi, *Electronic Structure of TiO_2 Surfaces and Effect of Molecular Adsorbates Using Different DFT Implementations.* J. Phys. Chem. C, 2010. **114**(51): p. 22659-22670.

149. Monkhorst, H.J. and J.D. Pack, *Special points for Brillouin-zone integrations.* Phys. Rev. B, 1976. **13**(12): p. 5188-5192.

150. Marques, M. and E. Gross, *Time-dependent density functional theory.* Annu. Rev. Phys. Chem., 2004. **55**: p. 427-455.

151. Bartolotti, L.J., *Time-dependent Kohn-Sham density-functional theory.* Phys. Rev. A, 1982. **26**(4): p. 2243.

152. Cremer, D., *Møller–Plesset perturbation theory.* Encyclopedia of computational chemistry, 1998.

153. Jensen, F., *Atomic orbital basis sets.* Wiley Interdisciplinary Reviews: Computational Molecular Science, 2013. **3**(3): p. 273-295.

154. Hehre, W.J., R. Ditchfield, and J.A. Pople, *Self—consistent molecular orbital methods. XII. Further extensions of Gaussian—type basis sets for use in molecular orbital studies of organic molecules.* J. Chem. Phys., 2003. **56**(5): p. 2257-2261.

155. Rassolov, V.A., J.A. Pople, M.A. Ratner, and T.L. Windus, *6-31G* basis set for atoms K through Zn.* J. Chem. Phys., 1998. **109**(4): p. 1223-1229.

156. Francl, M.M., W.J. Pietro, W.J. Hehre, J.S. Binkley, M.S. Gordon, D.J. DeFrees, and J.A. Pople, *Self-consistent molecular orbital methods. XXIII. A polarization-type basis set for second-row elements.* J. Chem. Phys., 1982. **77**(7): p. 3654-3665.

157. McHale, J.L., *Molecular spectroscopy*. 1999, Prentice Hall Upper Saddle River, NJ.

158. Datta, S., *Quantum Transport Atom to Transistor*.2005, Cambridge University.

159. Priyadarshy, S., S.S. Skourtis, S.M. Risser, and D.N. Beratan, *Bridge-mediated electronic interactions: Differences between Hamiltonian and Green function partitioning in a non-orthogonal basis.* J. Chem. Phys., 1996. **104**(23): p. 9473-9481.

160. Preat, J., D. Jacquemin, V. Wathelet, J.M. Andre, and E.A. Perpete, *TD-DFT investigation of the UV spectra of pyranone derivatives.* J. Phys. Chem. A, 2006. **110**(26): p. 8144-8150.

161. Preat, J., *Photoinduced Energy-Transfer and Electron-Transfer Processes in Dye-Sensitized Solar Cells: TDDFT Insights for Triphenylamine Dyes.* J. Phys. Chem. C, 2010. **114**(39): p. 16716-16725.

162. Ojamae, L., C. Aulin, H. Pedersen, and P.O. Kall, *IR and quantum-chemical studies of carboxylic acid and glycine adsorption on rutile TiO_2 nanoparticles.* J. Colloid Interface Sci., 2006. **296**(1): p. 71-78.

163. Vittadini, A., A. Selloni, F.P. Rotzinger, and M. Grätzel, *Formic acid adsorption on dry and hydrated TiO_2 anatase (101) surfaces by DFT calculations.* J. Phys. Chem. B, 2000. **104**(6): p. 1300-1306.

164. Nilsing, M., S. Lunell, P. Persson, and L. Ojamae, *Phosphonic acid adsorption at the TiO_2 anatase (101) surface investigated by periodic hybrid HF-DFT computations.* Surf. Sci., 2005. **582**(1-3): p. 49-60.

165. Nilsing, M., P. Persson, S. Lunell, and L. Ojamae, *Dye-sensitization of the TiO_2 rutile (110) surface by perylene dyes: Quantum-chemical periodic B3LYP computations.* J. Phys. Chem. C, 2007. **111**(32): p. 12116-12123.

166. Ernstorfer, R., L. Gundlach, S. Felber, W. Storck, R. Eichberger, and F. Willig, *Role of Molecular Anchor Groups in Molecule-to-Semiconductor Electron Transfer†.* J. Phys. Chem. B, 2006. **110**(50): p. 25383-25391.

167. Gundlach, L., R. Ernstorfer, and F. Willig, *Ultrafast interfacial electron transfer from the excited state of anchored molecules into a semiconductor.* Progr. Surf. Sci., 2007. **82**(4-6): p. 355-377.

168. Li, J.R., M. Nilsing, I. Kondov, H.B. Wang, P. Persson, S. Lunell, and M. Thoss, *Dynamical simulation of photoinduced electron transfer reactions in dye-semiconductor systems with different anchor groups.* J. Phys. Chem. C, 2008. **112**(32): p. 12326-12333.

169. Jakubikova, E., R.C. Snoeberger, V.S. Batista, R.L. Martin, and E.R. Batista, *Interfacial Electron Transfer in TiO_2 Surfaces Sensitized with Ru(II)-Polypyridine Complexes.* J. Phys. Chem. A, 2009. **113**(45): p. 12532-12540.

170. Pang, C.L., M. Watkins, G. Cabailh, S. Ferrero, L.T. Ngo, Q. Chen, D.S. Humphrey, A.L. Shluger, and G. Thornton, *Bonding of Methyl Phosphonate to TiO_2 (110).* J. Phys. Chem. C, 2010. **114**(40): p. 16983-16988.

171. Luschtinetz, R., J. Frenzel, T. Milek, and G. Seifert, *Adsorption of Phosphonic Acid at the TiO_2 Anatase (101) and Rutile (110) Surfaces.* J. Phys. Chem. C, 2009. **113**(14): p. 5730-5740.

172. Bates, S.P., G. Kresse, and M.J. Gillan, *The adsorption and dissociation of ROH molecules on TiO_2 (110).* Surf. Sci., 1998. **409**(2): p. 336-349.

173. Dovesi, R., R. Orlando, B. Civalleri, C. Roetti, V.R. Saunders, and C.M. Zicovich-Wilson, *CRYSTAL: a computational tool for the ab initio study of the electronic properties of crystals.* Zeitschrift Fur Kristallographie, 2005. **220**(5-6): p. 571-573.

174. Cora, F., *The performance of hybrid density functionals in solid state chemistry: the case of $BaTiO_3$.* Mol. Phys., 2005. **103**(18): p. 2483-2496.

175. Zicovich-Wilson, C.M., A. Bert, C. Roetti, R. Dovesi, and V.R. Saunders, *Characterization of the electronic structure of crystalline compounds through their localized Wannier functions.* J. Chem. Phys., 2002. **116**(3): p. 1120-1127.

176. Soler, J.M., E. Artacho, J.D. Gale, A. Garcia, J. Junquera, P. Ordejon, and D. Sanchez-Portal, *The SIESTA method for ab initio order-N materials simulation.* J. Phys. Condens. Matter, 2002. **14**(11): p. 2745-2779.

177. Di Valentin, C., G. Pacchioni, and A. Selloni, *Electronic structure of defect states in hydroxylated and reduced rutile TiO_2 (110) surfaces.* Phys. Rev. Lett., 2006. **97**(16).

178. Hara, K., T. Sato, R. Katoh, A. Furube, Y. Ohga, A. Shinpo, S. Suga, K. Sayama, H. Sugihara, and H. Arakawa, *Molecular design of coumarin dyes for efficient dye-sensitized solar cells.* J. Phys. Chem. B, 2003. **107**(2): p. 597-606.

179. Perdew, J.P., K. Burke, and M. Ernzerhof, *Generalized Gradient Approximation Made Simple.* Phys. Rev. Lett., 1996. **77**(18): p. 3865-3868.

180. Boschloo, G., L. Haggman, and A. Hagfeldt, *Quantification of the effect of 4-tert-butylpyridine addition to I^-/I_3^- redox electrolytes in dye-sensitized nanostructured TiO_2 solar cells.* Journal of Physical Chemistry B, 2006. **110**(26): p. 13144-13150.

181. Wang, Z.S., F.Y. Li, and C.H. Huang, *Highly efficient sensitization of nanocrystalline TiO_2 films with styryl benzothiazolium propylsulfonate.* Chem. Commun., 2000(20): p. 2063-2064.

182. Altobello, S., C.A. Bignozzi, S. Caramori, G. Larramona, S. Quici, G. Marzanni, and R. Lakhmiri, *Sensitization of TiO_2 with ruthenium complexes containing boronic acid functions.* J. Photochem. Photobiol., 2004. **166**(1-3): p. 91-98.

183. McNamara, W.R., R.C. Snoeberger, G. Li, J.M. Schleicher, C.W. Cady, M. Poyatos, C.A. Schmuttenmaer, R.H. Crabtree, G.W. Brudvig, and V.S. Batista, *Acetylacetonate Anchors for Robust Functionalization of TiO_2 Nanoparticles with Mn(II)-Terpyridine Complexes.* J. Am. Chem. Soc., 2008. **130**(43): p. 14329-14338.

184. McNamara, W.R., R.C. Snoeberger, G.H. Li, C. Richter, L.J. Allen, R.L. Milot, C.A. Schmuttenmaer, R.H. Crabtree, G.W. Brudvig, and V.S. Batista, *Hydroxamate anchors for water-stable attachment to TiO_2 nanoparticles.* Energy Environ. Sci., 2009. **2**(11): p. 1173-1175.

185. Forrest, S.R., *Organic-inorganic semiconductor devices and 3, 4, 9, 10 perylenetetracarboxylic dianhydride: an early history of organic electronics.* J. Phys. Condens. Matter, 2003. **15**(38): p. S2599-S2610.

186. Tautz, F.S., *Structure and bonding of large aromatic molecules on noble metal surfaces: The example of PTCDA.* Progr. Surf. Sci., 2007. **82**(9-12): p. 479-520.

187. Hardin, B.E., E.T. Hoke, P.B. Armstrong, J.H. Yum, P. Comte, T. Torres, J.M.J. Frechet, M.K. Nazeeruddin, M. Grätzel, and M.D. McGehee, *Increased light harvesting in dye-sensitized solar cells with energy relay dyes.* Nature Photon., 2009. **3**(7): p. 406-411.

188. Rice, C.R., M.D. Ward, M.K. Nazeeruddin, and M. Grätzel, *Catechol as an efficient anchoring group for attachment of ruthenium-polypyridine photosensitisers to solar cells based on nanocrystalline TiO_2 films.* New J. Chem., 2000. **24**(9): p. 651-652.

189. Boys, S.F. and F. Bernardi, *Calculation of small molecular interactions by differences of separated total energies - some procedures with reduced errors.* Mol. Phys., 1970. **19**(4): p. 553.

190. Frisch, M.J., G.W. Trucks, H.B. Schlegel, G.E. Scuseria, M.A. Robb, J.R. Cheeseman, J.A. Montgomery, T. Vreven, K.N. Kudin, J.C. Burant, J.M. Millam, S.S. Iyengar, J. Tomasi, V. Barone, B. Mennucci, M. Cossi, G. Scalmani, N. Rega, G.A. Petersson, H. Nakatsuji, M. Hada, M. Ehara, K. Toyota, R. Fukuda, J. Hasegawa, M. Ishida, T. Nakajima, Y. Honda, O. Kitao, H. Nakai, M. Klene, X. Li, J.E. Knox, H.P. Hratchian, J.B. Cross, V. Bakken, C. Adamo, J. Jaramillo, R. Gomperts, R.E. Stratmann, O. Yazyev, A.J. Austin, R. Cammi, C. Pomelli, J.W. Ochterski, P.Y. Ayala, K. Morokuma, G.A. Voth, P. Salvador, J.J. Dannenberg, V.G. Zakrzewski, S. Dapprich, A.D. Daniels, M.C. Strain, O. Farkas, D.K. Malick, A.D. Rabuck, K. Raghavachari, J.B. Foresman, J.V. Ortiz, Q. Cui, A.G. Baboul, S. Clifford, J. Cioslowski, B.B. Stefanov, G. Liu, A. Liashenko, P. Piskorz, I. Komaromi, R.L. Martin, D.J. Fox, T. Keith, A. Laham, C.Y. Peng, A. Nanayakkara, M. Challacombe, P.M.W. Gill, B. Johnson, W. Chen, M.W. Wong, C. Gonzalez, and J.A. Pople, *Gaussian 03, Revision C.02*, **2003** *Gaussian 03, Revision C.02*.

191. Benkö, G., J. Kallioinen, J.E.I. Korppi-Tommola, A.P. Yartsev, and V. Sundström, *Photoinduced Ultrafast Dye-to-Semiconductor Electron Injection from Nonthermalized and Thermalized Donor States.* J. Am. Chem. Soc., 2001. **124**(3): p. 489-493.

192. Wenger, B., M. Grätzel, and J.-E. Moser, *Rationale for Kinetic Heterogeneity of Ultrafast Light-Induced Electron Transfer from Ru(II) Complex Sensitizers to Nanocrystalline TiO_2.* J. Am. Chem. Soc., 2005. **127**(35): p. 12150-12151.

193. Kuang, D., S. Ito, B. Wenger, C. Klein, J.-E. Moser, R. Humphry-Baker, S.M. Zakeeruddin, and M. Grätzel, *High Molar Extinction Coefficient Heteroleptic Ruthenium Complexes for Thin Film Dye-Sensitized Solar Cells.* J. Am. Chem. Soc., 2006. **128**(12): p. 4146-4154.

194. Finnie, K.S., J.R. Bartlett, and J.L. Woolfrey, *Vibrational spectroscopic study of the coordination of (2,2 '-bipyridyl-4,4 '-dicarboxylic acid)ruthenium(II) complexes to the surface of nanocrystalline titania.* Langmuir, 1998. **14**(10): p. 2744-2749.

195. Duffy, N.W., K.D. Dobson, K.C. Gordon, B.H. Robinson, and A.J. McQuillan, *In situ infrared spectroscopic analysis of the adsorption of ruthenium(II)*

bipyridyl dicarboxylic acid photosensitisers to TiO_2 in aqueous solutions. Chem. Phys. Lett., 1997. **266**(5-6): p. 451-455.

196. Nazeeruddin, M.K., R. Humphry-Baker, P. Liska, and M. Grätzel, *Investigation of sensitizer adsorption and the influence of protons on current and voltage of a dye-sensitized nanocrystalline TiO_2 solar cell.* J. Phys. Chem. B, 2003. **107**(34): p. 8981-8987.
197. Pérez León, C., L. Kador, B. Peng, and M. Thelakkat, *Characterization of the Adsorption of Ru-bpy Dyes on Mesoporous TiO_2 Films with UV−Vis, Raman, and FTIR Spectroscopies.* J. Phys. Chem. B, 2006. **110**(17): p. 8723-8730.
198. Murakoshi, K., G. Kano, Y. Wada, S. Yanagida, H. Miyazaki, M. Matsumoto, and S. Murasawa, *Importance of binding states between photosensitizing molecules and the TiO_2 surface for efficiency in a Dye-sensitized solar cell.* J. Electroanal. Chem., 1995. **396**(1-2): p. 27-34.
199. Rensmo, H., K. Westermark, S. Sodergren, O. Kohle, P. Persson, S. Lunell, and H. Siegbahn, *XPS studies of Ru-polypyridine complexes for solar cell applications.* J. Chem. Phys., 1999. **111**(6): p. 2744-2750.
200. Johansson, E.M.J., M. Hedlund, H. Siegbahn, and H. Rensmo, *Electronic and molecular surface structure of $Ru(tcterpy)(NCS)_3$ and $Ru(dcbpy)_2(NCS)_2$ adsorbed from solution onto nanostructured TiO_2: A photoelectron spectroscopy study.* J. Phys. Chem. B, 2005. **109**(47): p. 22256-22263.
201. Syres, K.L., A.G. Thomas, D.J.H. Cant, S.J.O. Hardman, and A. Preobrajenski, *Pyrocatechol as a surface capping molecule on raffle TiO_2 (110).* Surf. Sci., 2012. **606**(3-4): p. 273-277.
202. Sasahara, A., K. Fujio, N. Koide, L. Han, and H. Onishi, *STM imaging of a model surface of $Ru(4,4'\text{-dicarboxy-}2,2'\text{-bipyridine})_2(NCS)_2$ dye-sensitized TiO2 photoelectrodes.* Surf. Sci., 2010. **604**(2): p. 106-110.
203. Shklover, V., Y.E. Ovchinnikov, L.S. Braginsky, S.M. Zakeeruddin, and M. Grätzel, *Structure of organic/inorganic interface in assembled materials comprising molecular components. Crystal structure of the sensitizer bis (4,4 '-carboxy-2,2 '-bipyridine)(thiocyanato) ruthenium(II).* Chem. Mater., 1998. **10**(9): p. 2533-2541.

204. Fillinger, A., D. Soltz, and B.A. Parkinson, *Dye sensitization of natural anatase crystals with a ruthenium-based dye.* J. Electrochem. Soc., 2002. **149**(9): p. A1146-A1156.

205. Sasahara, A., C.L. Pang, and H. Onishi, *STM observation of a ruthenium dye adsorbed on a TiO_2 (110) surface.* J. Phys. Chem. B, 2006. **110**(10): p. 4751-4755.

206. Ikeda, M., N. Koide, L. Han, C.L. Pang, A. Sasahara, and H. Onishi, *Lateral distribution of N3 dye molecules on TiO2 (110) surface.* J. Photochem. Photobiol. A, 2009. **202**(2-3): p. 185-190.

207. Persson, P. and M.J. Lundqvist, *Calculated Structural and Electronic Interactions of the Ruthenium Dye N3 with a Titanium Dioxide Nanocrystal.* J. Phys. Chem. B, 2005. **109**(24): p. 11918-11924.

208. De Angelis, F., S. Fantacci, A. Selloni, M.K. Nazeeruddin, and M. Grätzel, *Time-dependent density functional theory investigations on the excited states of Ru(II)-dye-sensitized TiO_2 nanoparticles: The role of sensitizer protonation.* J. Am. Chem. Soc., 2007. **129**: p. 14156-14157.

209. De Angelis, F., S. Fantacci, A. Selloni, M.K. Nazeeruddin, and M. Grätzel, *First-Principles Modeling of the Adsorption Geometry and Electronic Structure of Ru(II) Dyes on Extended TiO_2 Substrates for Dye-Sensitized Solar Cell Applications.* J. Phys. Chem. C, 2010. **114**(13): p. 6054-6061.

210. Schiffmann, F., J. VandeVondele, J. Hutter, R. Wirz, A. Urakawa, and A. Baiker, *Protonation-Dependent Binding of Ruthenium Bipyridyl Complexes to the Anatase(101) Surface.* J. Phys. Chem. C, 2010. **114**(18): p. 8398-8404.

211. Patrick, C.E. and F. Giustino, *O 1s core-level shifts at the anatase TiO_2 (101)/N3 photovoltaic interface: Signature of H-bonded supramolecular assembly.* Phys. Rev. B, 2011. **84**(8): p. 085330.

212. Labat, F., I. Ciofini, H.P. Hratchian, M.J. Frisch, K. Raghavachari, and C. Adamo, *Insights into Working Principles of Ruthenium Polypyridyl Dye-Sensitized Solar Cells from First Principles Modeling.* J. Phys. Chem. C, 2011. **115**(10): p. 4297-4306.

213. Gong, X.-Q. and A. Selloni, *Role of steps in the reactivity of the anatase TiO_2 (101) surface.* J. Catal., 2007. **249**(2): p. 134-139.

214. Henderson, M.A., *A surface science perspective on photocatalysis.* Surf. Sci. Rep., 2011. **66**(6–7): p. 185-297.

215. Bates, S.P., G. Kresse, and M.J. Gillan, *A systematic study of the surface energetics and structure of TiO_2 (110) by first-principles calculations.* Surf. Sci., 1997. **385**(2–3): p. 386-394.

216. http://www.tcm.phy.cam.ac.uk/~mdt26/crystal.html.

217. Niskanen, M., P. Hirva, and M. Haukka, *Computational DFT Study of Ruthenium Tetracarbonyl Polymer.* J. Chem. Theory Comput., 2009. **5**(4): p. 1084-1090.

218. Srikanth, K., V.R. Marathe, and M.K. Mishra, *Role of electronic structure of ruthenium polypyridyl dyes in the photoconversion efficiency of dye-sensitized solar cells: Semiempirical investigation.* Int. J. Quant. Chem., 2002. **89**(6): p. 535-549.

219. Fantacci, S., F. De Angelis, and A. Selloni, *Absorption Spectrum and Solvatochromism of the [Ru(4,4'-COOH-2,2'-bpy)$_2$(NCS)$_2$] Molecular Dye by Time Dependent Density Functional Theory.* J. Am. Chem. Soc., 2003. **125**(14): p. 4381-4387.

220. Patthey, L., H. Rensmo, P. Persson, K. Westermark, L. Vayssieres, A. Stashans, A. Petersson, P.A. Brühwiler, H. Siegbahn, S. Lunell, and N. Mårtensson, *Adsorption of bi-isonicotinic acid on rutile TiO_2 (110).* J. Chem. Phys., 1999. **110**(12): p. 5913-5918.

221. Odelius, M., P. Persson, and S. Lunell, *Bi-isonicotinic acid on rutile (110): calculated molecular and electronic structure.* Surf. Sci., 2003. **529**(1-2): p. 47-58.

222. Nazeeruddin, M.K., S.M. Zakeeruddin, R. Humphry-Baker, M. Jirousek, P. Liska, N. Vlachopoulos, V. Shklover, C.-H. Fischer, and M. Grätzel, *Acid−Base Equilibria of (2,2'-Bipyridyl-4,4'-dicarboxylic acid)ruthenium(II) Complexes and the Effect of Protonation on Charge-Transfer Sensitization of Nanocrystalline Titania.* Inorg. Chem., 1999. **38**(26): p. 6298-6305.

223. Sun, C., L.-M. Liu, A. Selloni, G.Q. Lu, and S.C. Smith, *Titania-water interactions: a review of theoretical studies.* J. Mater. Chem., 2010. **20**(46): p. 10319-10334.

224. Grabulosa, A., M. Beley, P.C. Gros, S. Cazzanti, S. Caramori, and C.A. Bignozzi, *Homoleptic Ruthenium Complex Bearing Dissymmetrical 4-Carboxy-4'-pyrrolo-2,2'-bipyridine for Efficient Sensitization of TiO_2 in Solar Cells.* Inorg. Chem., 2009. **48**(16): p. 8030-8036.

225. Vougioukalakis, G.C., A.I. Philippopoulos, T. Stergiopoulos, and P. Falaras, *Contributions to the development of ruthenium-based sensitizers for dye-sensitized solar cells.* Coord. Chem. Rev., 2011. **255**(21–22): p. 2602-2621.

226. Benkö, G., J. Kallioinen, P. Myllyperkiö, F. Trif, J.E.I. Korppi-Tommola, A.P. Yartsev, and V. Sundström, *Interligand electron transfer determines triplet excited state electron injection in RuN3-sensitized TiO_2 films.* J. Phys. Chem. B, 2004. **108**(9): p. 2862-2867.

227. Gamba, A., Simonett.M, and Tantardi.Gf, *Study of ground and excited states of biphenyl by molecules in molecules method.* Spectrochim. Acta Mol. Spectros., 1972. **A 28**(10): p. 1877-&.

228. Crocker, L., T. Wang, and P. Kebarle, *Electron affinities of some polycyclic aromatic hydrocarbons, obtained from electron-transfer equilibria.* J. Am. Chem. Soc., 1993. **115**(17): p. 7818-7822.

229. Stahl, D. and F. Maquin, *Charge-stripping mass spectrometry of molecular ions from polyacenes and molecular orbital theory.* Chem. Phys. Lett., 1984. **108**(6): p. 613-617.

230. Kasha, M., H. Rawls, and M.A. El-Bayoumi, *The exciton model in molecular spectroscopy.* Pure Appl. Chem., 1965. **11**(3-4): p. 371-392.

231. Troisi, A. and G. Orlandi, *Dynamics of the Intermolecular Transfer Integral in Crystalline Organic Semiconductors.* J. Phys. Chem. A, 2006. **110**(11): p. 4065-4070.

232. Gruhn, N.E., D.A. da Silva Filho, T.G. Bill, M. Malagoli, V. Coropceanu, A. Kahn, and J.-L. Brédas, *The Vibrational Reorganization Energy in Pentacene: Molecular Influences on Charge Transport.* J. Am. Chem. Soc., 2002. **124**(27): p. 7918-7919.

233. Deng, W.-Q. and W.A. Goddard, *Predictions of Hole Mobilities in Oligoacene Organic Semiconductors from Quantum Mechanical Calculations.* J. Phys. Chem. B, 2004. **108**(25): p. 8614-8621.

234. Redfield, A.G., *On the theory of relaxation processes.* IBM Journal of Research and Development, 1957. **1**: p. 19-31.

235. Renaud, N., P.A. Sherratt, and M.A. Ratner, *Mapping the Relation between Stacking Geometries and Singlet Fission Yield in a Class of Organic Crystals.* Phys. Chem. Lett., 2013. **4**(7): p. 1065-1069.

236. Nitzan, A., *Chemical Dynamics in Condensed Phases: Relaxation, Transfer and Reactions in Condensed Molecular Systems: Relaxation, Transfer and Reactions in Condensed Molecular Systems*. 2006, Oxford University Press.

237. Scholes, G.D. and K.P. Ghiggino, *Rate expressions for excitation transfer. 1 radiationless transition theory perspective.* J. Chem. Phys., 1994. **101**(2): p. 1251-1261.

238. Owrutsky, J.C., D. Raftery, and R.M. Hochstrasser, *Vibrational-relaxation dynamics in solutions.* Annu. Rev. Phys. Chem., 1994. **45**: p. 519-555.

239. Panero, C., R. Bini, and V. Schettino, *Vibron dynamics in naphtalene crystal.* J. Chem. Phys., 1994. **100**(11): p. 7938-7944.

240. Olson, R.W. and M.D. Fayer, *Site-dependent vibronic line widths and relaxation in the mixed molecular crystal pentacene in p-terphenyl.* J. Phys. Chem., 1980. **84**(16): p. 2001-2004.

241. Englman, R. and J. Jortner, *Energy gap law for radiationless transitions in large molecules.* Mol. Phys., 1970. **18**(2): p. 145-&.

242. Merzbacher, E., *Quantum Mechanics, 3rd Ed.* 1998, Wiley.

243. www.crystal.unito.it/basis-sets/